UNIVERSTIY OF CALIFORNIA SAN DIEGO

Soft materials for soft robots

A dissertation submitted in partial satisfaction of the requirements
for the degree Doctor of Philosophy

in

Materials Science & Engineering

by

Yang Wang

Committee in charge:

Professor Shengqiang Cai ,Chair
Professor Renkun Chen
Professor Darren Lipomi
Professor Kenneth Loh
Professor Tse Nga Ng

2022

The Dissertation of **Yang Wang** is approved, and it is acceptable in quality and form for publication on microfilm and electronically.

University of California San Diego

2022

Table of Contents

Dissertation Approval Page iii

Table of Contents iv

List of Figures viii

Acknowledgements xii

Vita xv

Abstract of the Dissertation xvii

Chapter 1 Introduction 1

1.1 Background 1

1.2 Liquid crystal elastomers (LCEs)-based actuation 2

1.3 Hydrogel-based sensing and computation 3

1.4 Dissertation structure 3

Chapter 2 Electrically controlled soft actuators with multiple and reprogrammable modes 4

2.1 Introduction 4

2.2 Results and discussion 6

2.2.1 Synthesis of disulfide LCE (ss-LCE) thin films 6

2.2.2 Disulfide exchange reaction and room temperature programming: 7

2.2.3 Fabrication process of heating wires 9

2.2.4 Fabrication of the ss-LCE based actuator: 13

2.2.5 Program/reprogram the ss-LCE based actuator into different modes: 15

2.2.6 Actuation performance of its contraction mode 16

2.2.7 Reprogrammability of the ss-LCE based actuator 19

2.2.8 Reprogrammability of the ss-LCE based actuator between multiple modes 19

2.3 Conclusion 22

Acknowledgements 22
Chapter 3 Liquid Crystal Elastomer based dexterous artificial motor unit 23
3.1 Introduction 23
3.2 Fabrication of the LCE-based motor unit 27
3.2.1 Preparation of the LCE precursor for the fabrication of the LCE thin film 27
3.2.2 Compression-assisted molding technique and characterization of the thickness 28
3.2.3 Fabrication of monodomain LCE thin film 30
3.2.4 Characterization of the monodomain LCE thin film 31
3.3 Construction of LCE-based artificial motor unit 35
3.3.1 Fabrication of the LCE-based artificial motor unit 35
3.3.2 Morphology characterization of the wrinkled gold coating layer 38
3.4 Quasi-static behavior of the LCE-based motor unit 40
3.4.1 Self-defined algorithms to obtain actuation strain from experimental videos.. 40
3.4.2 Isotonic tests and isometric tests with quasi-static stimulation conditions 41
3.5 Dynamic behaviors of the LCE-based motor unit 46
3.5.1 Representative dynamic behaviors 46
3.5.2 Fourier analysis of the time-varying actuation strain (power density spectrum) 48
3.5.3 Large strain rate observed in the dynamic behaviors 49
3.5.4 Isometric test of LCE-based motor unit with 30 V pulses 51
3.5.5 Systematic study of the dynamic behaviors 53
3.5.6 Output power density of LCE-based motor unit in isotonic tests 56
3.5.7 Comprehensive performance of the LCE-based motor unit outperforming real muscle 59
3.6 Actuation stress control of the motor unit 62

3.7 Electro-thermo-mechanical model of the LCE-based motor unit 65
3.7.1 Solving the temperature profile with given voltage pulses 65
3.7.2 Temperature-dependent equilibrium strain of an LCE-based motor unit..... 67
3.7.3 Electro-thermo-dynamic model 68
3.7.4 Amplification of actuation strain and output power density through system resonance 72
3.8 Work loop of the artificial motor unit 73
3.8.1 Experimental setup and data processing of the work loop analysis 73
3.8.2 Analysis of the results 74
3.8.3 Phase-controlled multifunctionalities of the LCE-based motor unit 76
3.9 Dexterous artificial neuromuscular system 78
3.9.1 Demonstrations with open-loop control 78
3.9.2 Demonstrations with close-loop control 82
3.10 Conclusion 83
Acknowledgements 86
Chapter 4 Stretchable and Transparent Ionic Diode and Logic Gates 87
4.1 Introduction 87
4.2 Results and discussion 89
4.2.1 Synthesis of polyelectrolyte doped hydrogels 89
4.2.2 Fabrication of hydrogel-based ionic diode 89
4.2.3 Experimental setup 90
4.2.4 Stretchable and transparent diode with rectification effect 92
4.2.5 Electrical performance of ionic diode under cyclic loading 94
4.2.6 Ionic logic gates 95
4.3 Conclusion 99
Acknowledgements 100

Chapter 5 Conclusion 101
5.1 Summary of the dissertation 101
5.2 Outlook for future work 103
Bibliography 104

List of Figures

Figure 2.1: Schematic illustration of (**a**) the chemical structure of ss-LCE and (**b**) mechanism of disulfide exchange reaction..... 5

Figure 2.2: Schematic illustration of the programming and reprogramming process of ss-LCE.. 7

Figure 2.3: Dependence of the actuation performance of the ss-LCE film on the programming process..... 8

Figure 2.4: Comparison of the actuation behavior of the ss-LCE film before and after the reprogramming procedures. 9

Figure 2.5: Fabrication of heating wires with half-and-half Peano structure. 11

Figure 2.6: Measurement of the thicknesses of the heating wire and the coated PI layer. 12

Figure 2.7: Working mechanism, design and fabrication of reprogrammable ss-LCE based actuator..... 14

Figure 2.8: Characterizations of ss-LCE based soft actuator..... 18

Figure 2.9: Multiple actuation modes can be programmed in the actuator. 20

Figure 3.1: Biomimetic design of an LCE-based artificial motor unit. 26

Figure 3.2: Molecular structure of the chemical components for synthesizing LCE thin film. .. 28

Figure 3.3: Compression-assisted LCE thin film molding process and its thickness measurements. 29

Figure 3.4: Preparations of LCE films before the sputtering of the gold film..... 30

Figure 3.5: The alignment of the mesogens in monodomain LCE can be confirmed by microscopy images in dark field..... 31

Figure 3.6: DSC analysis of monodomain LCE thin film. 32

Figure 3.7: Mechanical performance of an LCE thin film at room temperature. 33

Figure 3.8: Mechanical performance of LCE thin film at different temperatures. 33

Figure 3.9: Measurement of actuation strain and actuation stress of an LCE film from the tensile test under different temperatures. 34

Figure 3.10: Fabrication of LCE-based motor unit with wrinkled gold film coating..... 36

Figure 3.11: Pre-stretched monodomain LCE thin film with sputtered gold. 38

Figure 3.12: Thickness measurement of the sputtered gold film using surface profiler. 39

Figure 3.13: Characterization of the wrinkled surface morphology of a sputtered gold film. 39

Figure 3.14: Method for measuring the actuation strain of the LCE film during the test. 40

Figure 3.15: Quasi-static behavior of the LCE-based motor unit..... 42

Figure 3.16: Actuation strain versus time of LCE-based motor unit during quasistatic tests. 43

Figure 3.17: Actuation stress versus time of LCE-based motor unit obtained from isometric tests. The stimulations are 0.25 Hz 5 V voltage pulses with pulse width from 0.1 s to 0.5 s under different L/L_0 ratios..... 44

Figure 3.18: Maximum actuation stress during isometric tests with different stretches (L/L_0)... 45

Figure 3.19: Typical velocity and acceleration versus time of the LCE-based motor unit during its dynamic tests..... 47

Figure 3.20: Fourier analysis of actuation strain versus time during the dynamic isotonic tests. 48

Figure 3.21: Actuation strain and strain rate versus time of LCE-based motor unit when it is stimulated by a cyclically applied voltage pulse of 30 V at 1 Hz frequency..... 50

Figure 3.22: Actuation stress profile of the LCE actuator during isometric tests with different stimulation condition and stretches (L/L_0) 52

Figure 3.23: Actuation strain vs time of the LCE-based motor unit for different isotonic test conditions with the stimulation voltage at 30 V. 54

Figure 3.24: Bode plot of the actuation strain versus frequency (log-log) of the LCE motor unit during isotonic test under 30 V voltage stimulation with the frequency varying from 1 Hz to 16 Hz. The blue dashed line indicates the cutoff frequency at around 6 Hz, which is regarded as bandwidth of the LCE motor unit. 55

Figure 3.25: Difference between the largest and the smallest actuation strain of the LCE motor unit for different testing conditions. We calculated the results from Figure 3.23 and denoted it with

"maximum strain amplitude" in the vertical axis. We use this result to calculate the power density which will be discussed later. 55

Figure 3.26: Actuation strain versus time from different isotonic test conditions of the LCE-based motor unit with different LCE thickness and a constant applied stress of 1.7 MPa. 57

Figure 3.27: The peak of the power density always occurs at 6 Hz with different LCE thicknesses and a constant applied stress (1.7 MPa) during isotonic tests..... 58

Figure 3.28: LCE-based motor unit shows a large actuation strain (40% ~ 60%) during isotonic test with applied stress of 1.5 MPa. 59

Figure 3.29: For the LCE film with the thickness of 10 μm, its work density can reach 455 J/kg under applied stress of 1.7 MPa. 60

Figure 3.30: Dynamic behaviors of the LCE-based motor unit..... 61

Figure 3.31: Control of the actuation stress of the motor unit in isometric tests..... 63

Figure 3.32: The sharp peaks of the actuation stress merge to form a stable plateau once the stimulation frequency is larger than 10 Hz in isometric tests. 64

Figure 3.33: Experimental measurements of the equilibrium strain ($\varepsilon^*(T)$) of LCE motor unit versus temperature under different applied stresses (0.5 MPa ~ 1.5 MPa). 67

Figure 3.34: Electro-thermo-mechanical model of an LCE-based motor unit. 69

Figure 3.35: Comparisons between the experimental results and simulation results of the actuation strain in quasi-static cases (Vp = 5 V, f = 0.25 Hz, tw = 0.3~0.4 s, applied stress = 1.5 MPa).. 71

Figure 3.36 Comparison between the experimental results and simulation results of the actuation strain versus time for dynamic cases (Vp = 30 V, f = 1~ 2Hz, tw= 3~5 ms, applied stress = 1.5 MPa)..... 71

Figure 3.37: Data processing of the work loop experiment..... 74

Figure 3.38: Work loop of the LCE-based motor unit..... 75

Figure 3.39: Work loops of the LCE-based motor unit for different phases (0% ~ 90%) when the stimulating voltage pulse (30 V, 0.25 Hz, 4 ms pulse width) was applied. Different shapes and directions of the loop indicate different energy conversion processes in the motor unit. 76

Figure 3.40: Dexterous artificial neuromuscular system. 79

Figure 3.41: Active close-loop PID control of the joint angle..... 83

Figure 3.42: Durability of the LCE-based motor under cyclic actuation. 85

Figure 4.1: Structure and fabrication of a hydrogel-based ionic diode. 90

Figure 4.2: High transparency and stretchability of hydrogel-based ionic diode. 92

Figure 4.3: Current-Voltage characteristic curves of the ionic diode with several different stretches. 93

Figure 4.4: Performance of the hydrogel-based ionic diode after cyclic stretch. 95

Figure 4.5: Hydrogel-based ionic OR gate. 96

Figure 4.6: Hydrogel-based ionic AND gate. 98

Acknowledgements

I could not finish my journey and finally get the PhD degree without the help and support from many people, and I would like to express my gratitude to all of them here.

First, I would like to express my deepest gratitude to my advisor, Prof. Shengqiang Cai, who is the best advisor one can hardly met in this world. He is not only an academically advisor but also a life mentor who provides me so many insightful guidance when I got lost. His deep understanding of mechanics and physics provided me so many insightful inspirations through my entire PhD life. I learned a lot from the discussions with him. His patience and great passion in doing research makes me feel so enjoyable when working with him to explore different research topics. I feel really lucky to have him as my PhD advisor.

Secondly, I would like to thank all my committee members: Professor Renkun Chen, Professor Darren Lipomi, Professor Kenneth Loh and Professor Tse Nga Ng for their valuable suggestions, comments to my research projects.

Thirdly, I would like to thank all my collaborators: Professor Yong-Lae Park, Jiyeon Cho, Prof. Tse Nga Ng, Dr. Zhijian Wang, Wei Fan, Qiguang He, Jinrong Li, Prajval Iyer and Zhengliang Su.

Last, I would like to thank group members from Cai Group, thank you for all the help you have provided. They are Zhijian Wang, Qiguang He, Chihyung Ahn, Xudong Liang, Wei Fan, Somaye Jafari, Yue Zheng, Zhaoqiang Song, Zijun Wang, Chenghai Li, Raja Annapooranan, Nada F. Qari, Gaoweiang Dong, Robert Chambers, Ram Hemanth Yeerella, Shengjia Zhang, and all the

current and previous group members.

Finally, I would like to thank my family and my friends who gives me unconditional support all the time. Their love and support give me courage to keep going on when I confronted difficulties in my lift. This endeavor would not have been possible without your help, thank you all!

Chapter 2, in full, is a reprint of the material as it appears in "Electrically controlled soft actuator with multiple and reprogrammable actuation modes", *Advanced Intelligent Systems* 2 (2020): 1900177, by Yang Wang, Zhijian Wang, Qiguang He, Prajval Iyer, Shengqiang Cai. The dissertation author was the primary investigator and first author of this paper.

Chapter 3, in full, is currently being prepared for publication by Yang Wang, Qiguang He, Zhijian Wang, Shengjia Zhang, Chenghai Li, Zijun Wang, Yong-Lae Park, Shengqiang Cai. The dissertation author was the primary investigator and first author of this paper.

Chapter 4, in full, is a reprint of the material as it appears in "Stretchable and transparent ionic diode and logic gates", *Extreme Mechanics Letters*, vol. 28, 2019, by Yang Wang, Zhijian Wang, Zhengliang Su, Shengqiang Cai. The dissertation author was the primary investigator and first author of this paper.

Vita

2014 Bachelor of Engineering in Electronic Packaging, Beijing Institute of Technology

2016 Master of Science in Structural Engineering, University of California San Diego

2022 Doctor of Philosophy in Materials Science & Engineering, University of California San Diego

Publications

1. **Y Wang**, Z. Wang, Z. Su, S. Cai, "Stretchable and transparent ionic diode and logic gates", *Extreme Mechanics Letters*, 28 (2019): 81-86.

2. **Y. Wang**, Z. Wang, Q. He, P. Lyer, S. Cai, "Electrically controlled soft actuator with multiple and reprogrammable actuation modes", *Advanced Intelligent Systems* 2 (2020): 1900177.

3. **Y. Wang**, Q. He, Z. Wang, S. Zhang, C. Li, Z. Wang, Y. Park, S. Cai, "Liquid crystal elastomer based dexterous artificial motor unit", submitted.

4. W. Fan, **Y. Wang**, S. Cai, "Fatigue fracture of a highly stretchable acrylic elastomer", *Polymer Testing* 61 (2017), 373-377.

5. J. Li, **Y. Wang**, L. Liu, S. Xu, Y. Liu, J. Leng, S. Cai, "A biomimetic soft lens controlled by electrooculographic signal", *Advanced Functional Materials* 29 (2019), 1903762.

6. Z. Wang, **Y. Wang**, Z. Wang, Q. He, C. Li, S. Cai, "3D printing of electrically responsive PVC gel actuators", *ACS Applied Materials & Interfaces* 13 (2021), 24164-24172.

7. R. Annapooranan, **Y. Wang**, S. Cai, "Highly Durable and Tough Liquid Crystal Elastomers", *ACS Applied Materials & Interfaces* 14 (2022), 2006-2014.

8. Z. Wang, **Y. Wang**, S. Cai, J. Yang, "Liquid Crystal Elastomers for Soft Actuators", *Materials Lab* 1 (2022), 220030-1-220030-4.

9. Q. He, Z. Wang, **Y. Wang**, A. F. Minori, M. T. Tolley., S. Cai, "Electrically Controlled Liquid Crystal Elastomer Based Soft Tubular Actuator with Multimodal Actuation", *Science advances,* 5 (2019): eaax5746.

10. Z. Wang, Q. He, **Y. Wang**, S. Cai, "Programmable actuation of liquid crystal elastomer via "living" exchange reaction", *Soft matter,* 15 (2019): 2811-2816.

11. Q. He[#], Z. Wang[#], **Y. Wang**, Z. Song, S. Cai, "Recyclable and self-repairable fluid-driven liquid crystal elastomer actuator", *ACS applied materials & interfaces* 12 (2020): 35464-35474.

12. Q. He, Z. Wang, **Y. Wang**, Z. Wang, C. Li, R. Annapooranan, J. Zeng, R. Chen, S. Cai, "Electrospun liquid crystal elastomer microfiber actuator", *Science Robotics* 6 (2021), eabi9704.

13. C. Li, Z. Wang, **Y. Wang**, Q. He, R. Long, S. Cai, "Effects of network structures on the fracture of hydrogel", *Extreme Mechanics Letters* 49 (2021), 101495.

14. C. Li, Q. He, **Y. Wang**, Z. Wang, Z. Wang, R. Annapooranan, M.I. Latz, S. Cai, "Highly robust and soft biohybrid mechanoluminescence for optical signaling and illumination", *Nature communications* 13 (2022), 1-13.

15. Z. Wang, W. Fan, Q. He, **Y. Wang**, X. Liang, S. Cai, "A simple and robust way towards reversible mechanochromism: Using liquid crystal elastomer as a mask", *Extreme Mechanics Letters,* 11 (2017): 42-48.

16. Z. Wang, Z. Wang, Y. Zheng, Q. He, **Y. Wang**, S. Cai, "Three-dimensional printing of functionally graded liquid crystal elastomer", *Science advances,* 6 (2020): eabc0034.

Abstract of the Dissertation

Soft materials for soft robots

by

Yang Wang

Doctor of Philosophy in Materials Science & Engineering

University of California San Diego, 2022

Professor Shengqiang Cai, Chair

Comparing with traditional robotic design based rigid materials, soft material based robotic design shows unique advantages such as large deformation and great compatibility for many applications such as human-machine-interfaces. The field of soft robotics has witnessed numerous growths of new designs of soft actuators and soft sensors. Even though they show the great uniqueness of using soft materials but many of them do not have a comprehensive performance to adapt to different complex scenarios. Therefore, we came with material-level designs using soft smart materials, such as liquid crystal elastomers and hydrogels, to address this challenge.

In this dissertation, we first designed and fabricated an electrically controlled soft actuator with multiple and reprogrammable actuation modes, and then demonstrated a reusable and general-purpose soft actuator which can meet various requirements in constructing new soft active devices. Secondly, we developed an integrated artificial motor unit based on gold-coated ultrathin liquid crystal elastomer (LCE) film. Due to the small thermal inertial of the ultrathin LCE structure, its cyclic actuation speed is fast and easily controllable. We showed that under electrical stimulation, the actuation strain of the LCE-based motor unit reaches 45%, strain rate is as high as 750 %/s, and the output power density is as high as 1360 W/kg. Lastly, we developed a transparent and stretchable hydrogel-based ionic diode based on doped polyacrylamide hydrogels. Using the ionic diode, we further successfully constructed two types of ionic logic gates, which can potentially be used as soft sensors. We hope the material-based designs of soft actuators and soft sensors we developed in this dissertation can be used as the basic functional elements for advanced and integrated soft robotic systems.

Chapter 1 Introduction

1.1 Background

Over the past decades, numerous extraordinary works have demonstrated many unique properties of soft robots, such as human-friendly interface for interactions, large number of degree of freedoms (DOFs) and so on [1, 2]. These properties push forward a profound change in paradigm of designing robots to fulfill demands from real world, especially intriguing designs based on soft materials with different functionalities [3-5]. Various smart materials has been developed for different designs of robots [6]. Although the rapid development of soft materials provides more opportunities for soft robots, it is still challengeable to generate comprehensive designs which can embed capabilities of sensation, actuation or computation into soft materials while maintain their unique mechanical properties, namely soft [7].

Many soft material-based actuator has been developed to address such challenge [7-10]: such as dielectric elastomer actuator with high power density for insect-like robot [11], hydrogel with fast responsive speed and high actuation force [12], LCE-based artificial muscle with large actuation strain and actuation stress as well [13], pneumatic walker with electronic-free computation capability [14] and so on. But only limited design can compare with the main metrics of the actuation performance of the biological muscles.

Besides than actuation, using soft materials to realize sensation or computation is also an emerging field. For example, people have developed hydrogel-based strain sensor with large

stretchability [15], hydrogel-based flexible pH sensor [16], stretchable CNT-based strain sensor through structure design [17], and so on. We also have soft material-based computation components designs such as pneumatic oscillator [18] or soft digital logic circuits [19].

Despite the great advancement in designing diverse soft robots, they are not yet as dexterous as most soft animals in many aspects. One main reason is that they still lack integrated artificial neuromuscular systems with a great performance and also are hard to be conveniently fabricated, although many recently developed artificial muscles, various sensors and control systems have shown excellent properties individually. In this dissertation, we will explore the possibilities of addressing such challenges using smart soft materials such as liquid crystal elastomers (LCEs) and polyelectrolyte doped hydrogels.

1.2 Liquid crystal elastomers (LCEs)-based actuation

Liquid crystal elastomers (LCEs) have been widely recognized as a promising soft actuating material with many unique features such as large actuation stress, strain, and work density. The phase transition between nematic phase and isotropic phase leads to large reversible deformation which makes LCE a perfect choice for soft actuators [20]. The external stimulus to trigger the actuation of LCE can be light [21], heat [22], and chemicals [23]. Designing LCE-based soft actuator involves the chemical design to realize desired functionalities and the control system to apply the external stimulus. In all the forms of external stimulation, electrical driven actuators show the best compatibility with the current electronic circuit systems. The difficulty of designing such soft actuating system comes from requiring electrical controllability, large actuation

strain/stress and fast response speed all at a same time. This challenge will be addressed in this dissertation later.

1.3 Hydrogel-based sensing and computation

Biological neural system shows efficient information processing functionality with electronic-free ionic signals. Considering that biological system is usually wet and ionic, it has been proposed to make ionic device using hydrogels as complementary to traditional electronic devices [24]. Meanwhile, various designs of hydrogel-based sensation and computation [25-28] may enrich the application scenarios of soft robots such as the soft human-machine interfaces. In this dissertation, we will explore the possibilities of using hydrogel to design new types of ionic logic circuits which can potentially be used as ionic sensation or computation component.

1.4 Dissertation structure

The objective of my dissertation is to design and fabricate robotic components which owns comprehensive properties. We describe the design and fabrication process, characterize the performance of the LCE-based actuators and hydrogel-based stretchable diodes. This dissertation is organized as follows:

Chapter 1 introduces the background of using soft materials to realize soft robotic applications. Chapter 2 describes how to construct a reprogrammable LCE-based actuator, Chapter 3 describes an LCE-based artificial motor unit and the neuromuscular system built based on it, Chapter 4 describes the strategy to demonstrate a stretchable ionic diode and the ionic logic gates with the developed diode. Chapter 5 summaries the dissertation and provide outlooks for the future works.

Chapter 2 Electrically controlled soft actuators with multiple and reprogrammable modes

2.1 Introduction

Soft actuators are of great interest in diverse applications where muscle-like actuations are desired [29]. Advances in soft actuators have enabled the design and fabrication of novel soft robotics [2, 30, 31], biomimetic devices [32, 33] and wearable devices [34]. To meet the requirements of various applications, soft actuators with different actuation modes have been developed. For example, polymer composite fibers [9, 35] and twisted fishing line artificial muscles [4] can generate large uniaxial contraction. LCE tubular actuator [13] and self-sensing paper-based actuators [36] can exhibit bending actuation. Shear-vacuum-actuated machines [37] show active shear deformation. However, most previously developed soft actuators can only have one actuation mode, which is fixed once it is fabricated. In this work, by embedding stretchable heating wires into disulfide liquid crystal elastomers (ss-LCEs), [38, 39] we have successfully designed and fabricated an electrically controlled soft actuator with multiple and reprogrammable actuation modes. We believe the ss-LCE based soft actuator can find its wide applications in constructing different soft active structures and devices.

Thermally driven LCE has been widely recognized as a promising soft actuating material with many unique features such as large actuation stress, actuation strain, and work density [40-45]. Actuation of an LCE originates from the phase transition of the liquid crystal mesogens in the

material. Once the temperature of an LCE is increased above nematic-to-isotropic phase transition temperature, aligned mesogens in nematic phase transform to isotropic phase accompanying with significant shape change. Such shape change is reversible once the temperature is decreased down to room temperature with mesogens transiting from isotropic phase back to nematic phase. Previous work has demonstrated that various actuation modes of LCE can be achieved by controlling different alignment of mesogens [46-51]. Moreover, our recent work has shown that by introducing disulfide bonds into LCE, its actuation mode can be easily programmed at room temperature though dynamic bond exchanging reaction [39]. In the current work, we choose to use ss-LCE (see its chemical structure in Figure 2.1) to construct a reprogrammable soft actuator.

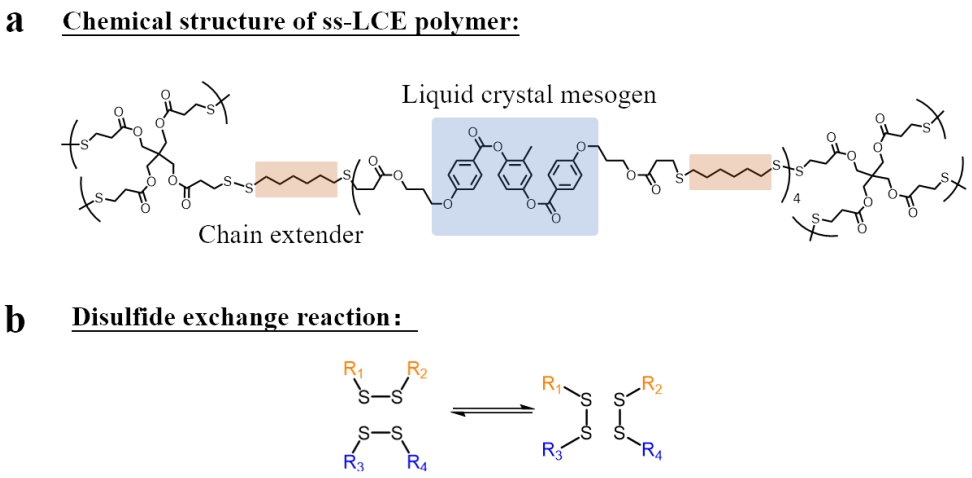

Figure 2.1: Schematic illustration of (**a**) the chemical structure of ss-LCE and (**b**) mechanism of disulfide exchange reaction.

2.2 Results and discussion

2.2.1 Synthesis of disulfide LCE (ss-LCE) thin films

We use the following chemicals to synthesize the ss-LCE: (1,4-bis-[4-(3-acryloyloxypropyloxy) benzoyloxy]-2-methylbenzene) (RM257) (Wilshire company, 95 %) as liquid crystal mesogens; 1,6-hexanedithiol (HDT, Alfa-Aesar, 97%) as chain extender; pentaerythritol tetrakis (3-mercaptopropionate) (PETMP, Sigma-Aldrich, 95%) as crosslinker; dipropylamine (DPA, Sigma-Aldrich, 98%), 30% hydrogen peroxide solution (Fisher Chemical), sodium iodide (Sigma-Aldrich, 99%) and sodium thiosulfate pentahydrate (Fisher Scientific) as catalyst. All the chemicals were used as received without further purification.

First, RM257 (9.42 g, 16 mmol) and HDT (3.00 g, 20 mmol) were dissolved in acetone (50 mL). Then the catalyst DPA (0.2 g, 2 mmol) was added into the solution and the mixture was stirred overnight until the turbid LCE oligomer solution had been formed. We then evaporated acetone away with rotary evaporator (Buchi) and dissolved the concentrated solution in THF (50 mL). After that, the crosslinker PETMP (0.98 g, 2 mmol) was added into the THF solution. Then, oxidized reagent 30% hydrogen peroxide (1 mL) and catalyst NaI (0.04 g, 0.26 mmol) were added into the mixture. The mixture was stirred for 24 hours, and the gelation formed. Then, we cut the gel into small pieces and washed with 5% sodium thiosulfate solution and then DI water for 3 times. The ss-LCE sample was obtained as small yellow pieces after fully dried in the oven at 85°C overnight. The particles were then subject to hot-compression (Carver Hot Embossing System) at

180°C for 1 hour with 1-ton compression force to get a thin-film shaped product with a thickness of around 0.25mm.

2.2.2 Disulfide exchange reaction and room temperature programming:

We illustrate the chemical structure of ss-LCE polymer and the mechanism of disulfide exchange reaction in Figure 2.1. Once temperature of ss-LCE is increased to 180 °C, the disulfide bonds can be cleaved, and free radicals are generated. After the temperature is lowered down to room temperature, mesogens are in polydomain state with residual free radicals inside the material. These residual free radicals can stay in the material for several hours at room temperature which enables the material programming. The programming and reprogramming process of ss-LCE is shown in Figure 2.2.

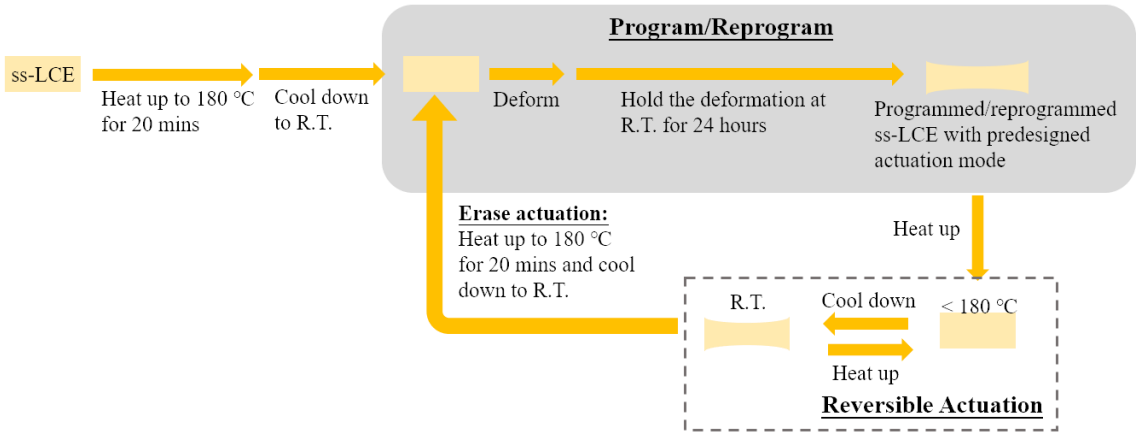

Figure 2.2: Schematic illustration of the programming and reprogramming process of ss-LCE.

As illustrated in Figure 2.2, with the help of disulfide exchange reaction (Figure 2.1b), actuation mode of a ss-LCE film can be easily reprogrammed. The sample needs to be first heated up to 180 °C for 20 mins and then cooled it down to room temperature. After the temperature is lowered to room temperature, mesogens in the LCE are in a polydomain state and thus its

preexisting actuation mode (or alignment of mesogens) is erased. Subsequently, by deforming the ss-LCE into another shape and hold the deformation for 24 hours, new alignment of mesogens can be introduced thus the ss-LCE has been reprogrammed. With the heating time of 20 mins at 180 ℃ and deformation holding time of 24 hours, the new alignment of mesogens can be fixed (see Figure 2.3). The ss-LCE films were firstly programmed by a uniaxial stretch of 1.5 with a desired pre-designed actuation strain as 33%. The actuation strain was then tested on a hotplate of 120 ℃. When the heating time at 180 ℃ is longer than 10 mins and the deformation holding time is longer than 16 hours, the actuation reaches the predesigned value.

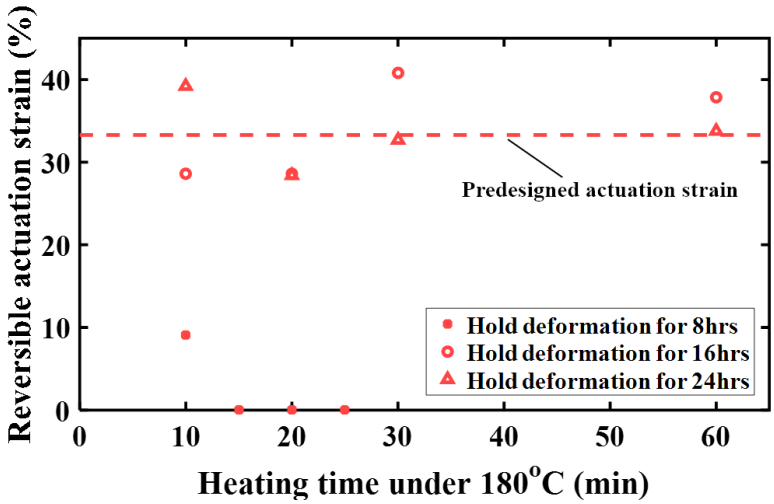

Figure 2.3: Dependence of the actuation performance of the ss-LCE film on the programming process.

More importantly, no degradation of the actuation performance of a reprogrammed ss-LCE is detected during the reprogramming process as shown in Figure 2.4. The ss-LCE film was firstly programmed with active contraction around 33%. After the measurement of the actuation strain,

the actuation in the LCE was erased and then reprogrammed. The degradation of the actuation performance of the reprogrammed LCE is insignificant.

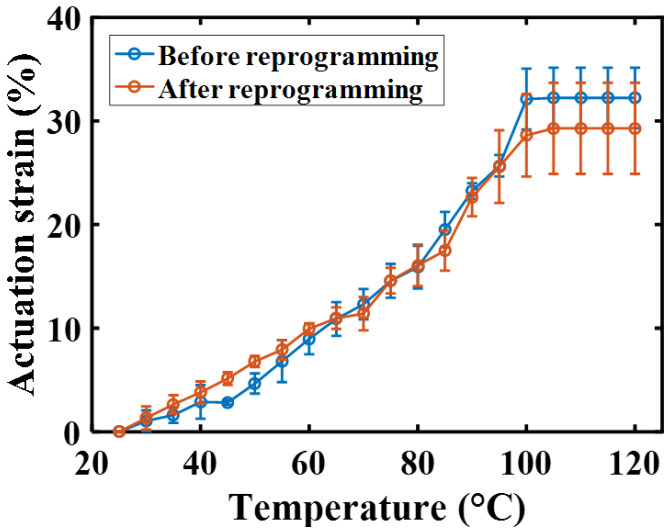

Figure 2.4: Comparison of the actuation behavior of the ss-LCE film before and after the reprogramming procedures.

2.2.3 Fabrication process of heating wires

In addition to the actuating material, how to apply external stimuli to trigger the actuation is crucial for an actuator in its applications. In the past, different strategies have been adopted to trigger the actuation of an LCE as thermally responsive material. One commonly adopted way to change the temperature of LCE is through controlling the environmental temperature [52, 53]. Photothermal effects have also been used to realize remote control of local temperature change in LCE [54, 55]. Compared to those heating strategies, Joule heating generated by resistive heating wires embedded in the material has shown several advantages including simple control, low cost

and easy integration [13]. To construct an electronically controllable actuator, in the current work, we integrate resistive heating wires of carefully selected shape with ss-LCE films.

To make a soft actuator with great stretchability along an arbitrary direction, we embedded heating wires with half-and-half Peano shape [56] into the actuator. The heating wires were fabricated through standard photolithography as described in the following paragraph.

As shown in Figure 2.5, we first spin-coated polyimide precursor (PI-2545, HD Microsystems) onto the copper foil (MicroThin copper foil, Insulectro Company). PI precursor was then fully cured at 300°C in nitrogen environment. Then, we placed the PI-coated copper foil onto the glass substrate with copper side facing up, as shown in Step 1 in Figure 2.5. Photolithography and wet etching were then used to define the patterns of the heating wires on copper layer (Step 2). Mask I in Figure 2.5 was used in this step of photolithography. Later, we spin-coated another layer of PI on the patterned copper layer (Step 3) same as in Step 1. After that, 2nd step photolithography and dry etching process defined the final pattern of the heating wires (Step 4), in which copper was fully encapsulated and insulated by the PI expect for the two contact pads shown in the dash box in Figure 2.6a. Mask II in Figure 2.5b was used in this step of photolithography.

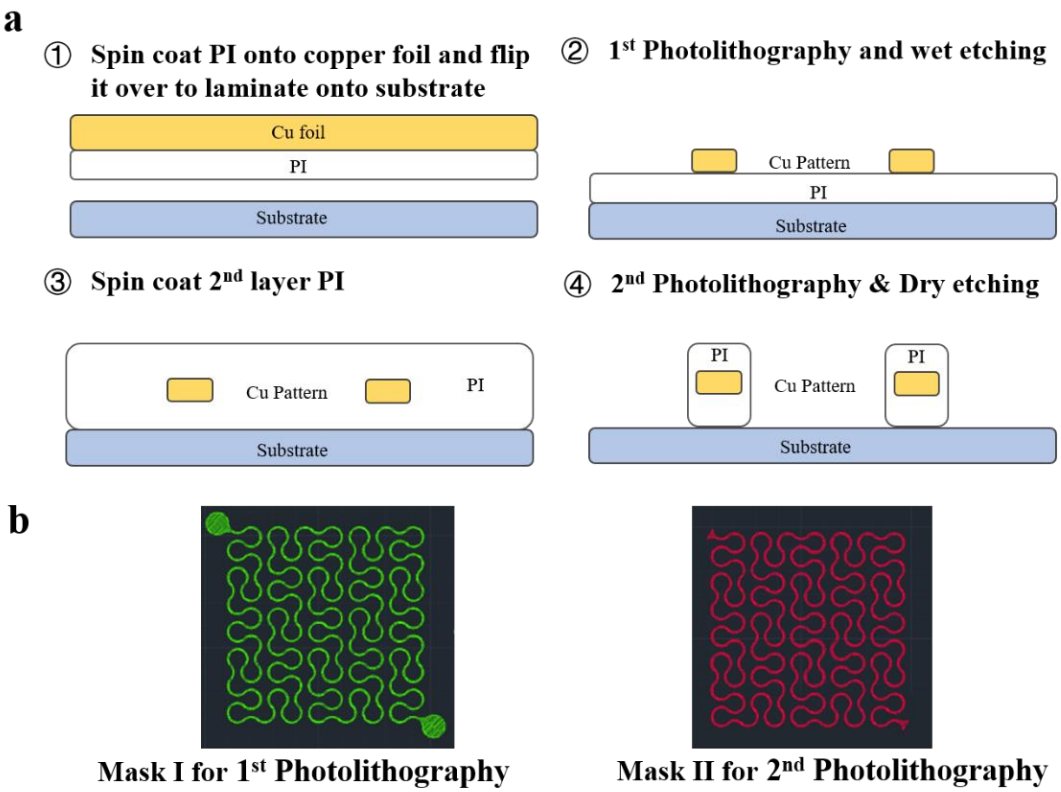

Figure 2.5: Fabrication of heating wires with half-and-half Peano structure.
a, Fabrication process of stretchable heating wires with standard photolithography technique. **b,** Designs of Mask I and Mask II used in step ② and step ④ during photolithography.

The thickness of spin-coated polyimide (PI) was around 3.5 μm which was verified using stylus profilometer (Dektak XT) as in Figure 2.6b. The total thickness of the heating wires was around 20 μm which was also verified using stylus profilometer (Dektak XT) as in Figure 2.6c. To further enhance the stretchability of the heating wires, we attached the heating wires to an initially biaxially pre-stretched LCE film and the heating wires were under biaxial compression after the pre-stretch in the LCE films was removed. Detailed fabrication steps can be discussed later.

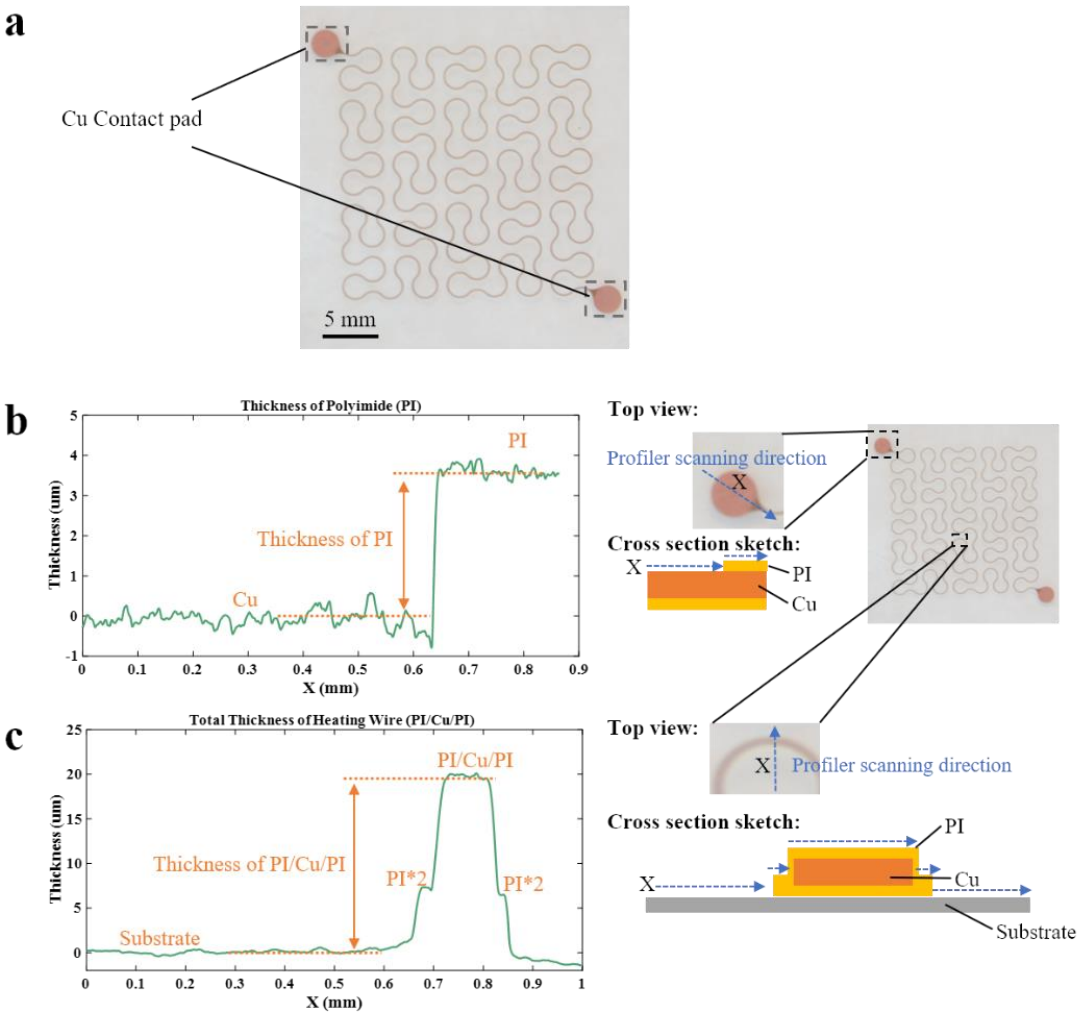

Figure 2.6: Measurement of the thicknesses of the heating wire and the coated PI layer. **a,** A photo of the heating wires with half-and-half Peano structure. The heating wires were fabricated on the surface of a glass substrate. A white paper was used beneath the substrate as background. Inside the two dashed boxes are two contact pads reserved for soldering. **b,** Measurement of the thickness of the coated PI film by profilometer (Dektak XT). The characterization shows that the thickness of the PI film is around 3.5 μm. **c.** The characterization shows that the thickness of the heating wire including both of the copper wire and the coated PI film (wrapping around the copper wire) is around 20 μm.

2.2.4 Fabrication of the ss-LCE based actuator:

As shown in Figure 2.7, with the fabricated heating wires and synthesized two ss-LCE thin-films with the thickness of around 0.25 mm (4 cm × 4 cm), we then stretched both ss-LCE films equal-biaxially with the stretch ratio around 1.3 and fixed the stretch. To attach the heating wires onto the surface of one of the ss-LCE film, we first transferred the heating wires from the glass substrate to a water-soluble tape (Arc-Zone), and then attached the tape onto the ss-LCE film using stick glue. The ss-LCE film together with the water-soluble tape and heating wires was left untouched for 1 day. We next cut out the central area of the ss-LCE film and took it away from the acrylate plate. We then dissolved the water-soluble tape on the surface of the ss-LCE film by using DI water, while the heating wires still attached on the surface of the ss-LCE film. After the entire film was fully dried, we covered it by the other stretched ss-LCE film on top to get a sandwich structure. We then heated up the sandwich structure using a hotplate with temperature of 120 °C for 5 mins, which caused the biaxial contraction of the entire film thus increased stretchability of heating wires. After that, we compressed the sandwich structure using two glass slides and multiple clips, and then put it in an oven of 180 °C for 20 mins to form bonding between two ss-LCE films. Finally, we took the entire structure out from the oven and cooled it down to room temperature. To connect the actuator with external power supply, we carefully peeled off small pieces of LCE film to expose the metal contact pads (Figure 2.6) of the heating wires, and then soldered electrical wirings onto them for connection of external power supply. The final actuator was of 3 cm x 3 cm with a thickness of around 0.5 mm.

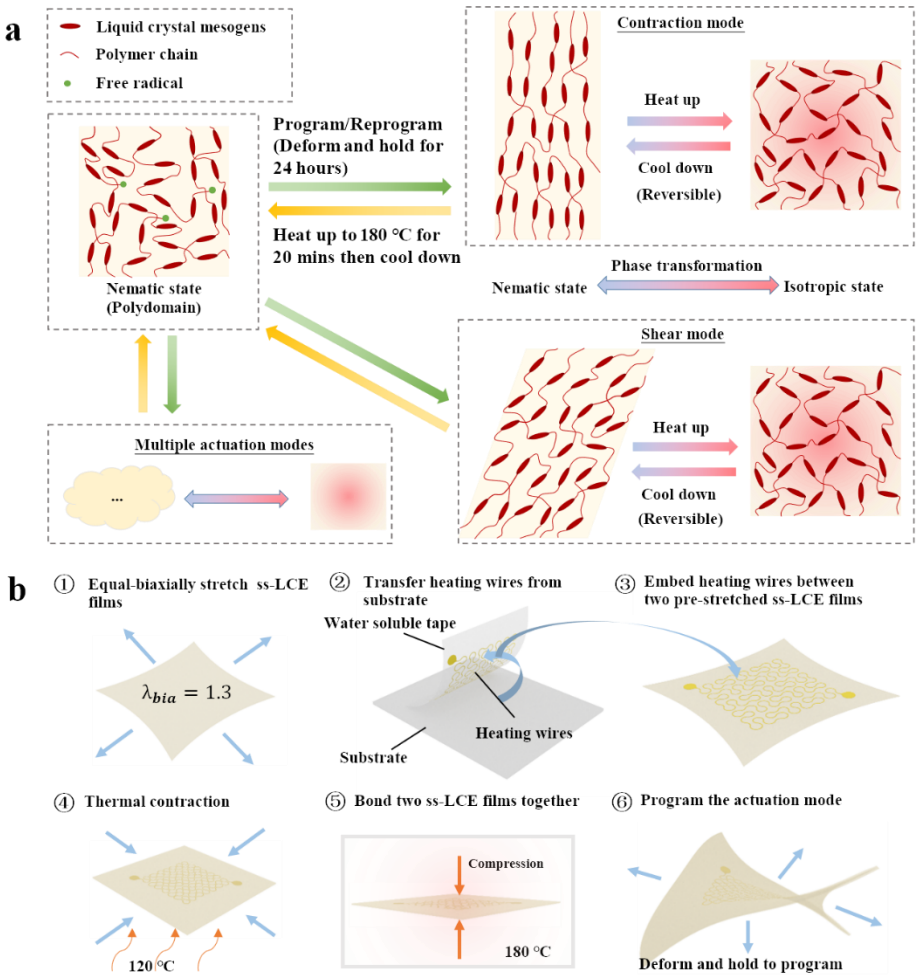

Figure 2.7: Working mechanism, design and fabrication of reprogrammable ss-LCE based actuator.

a, Schematics of reversible actuation of ss-LCE with contraction mode and shear mode and the reprogrammability of ss-LCE based on disulfide exchange reaction; **b,** Fabrication process of a reprogrammable ss-LCE based actuator: ① Stretch two ss-LCE films equal-biaxially with the stretch ratio around 1.3. The biaxial stretch in the two ss-LCE films is maintained for 1 day. ② Transfer heating wires from its glass substrate to a water-soluble tape. ③ Attach the tape with heating wires onto the biaxially pre-stretched ss-LCE film, dissolve the water-soluble tape away with only heating wires attached on ss-LCE film, and cover the thin film by another equal-biaxially stretched ss-LCE film on top to get a sandwich structure. ④ Heat the sandwich structure up to 120°C for 5 mins, which causes biaxial contraction of the ss-LCE film and thus biaxially compresses the heating wires. ⑤ Put the whole structure under compression and in an oven of 180 °C for 20 mins to form strong bonding between the two ss-LCE films. ⑥ Take the entire structure out from the oven and cool it down to room temperature, and then deform the entire structure at room temperature to program it with a desired actuation mode.

2.2.5 Program/reprogram the ss-LCE based actuator into different modes:

With the fabricated actuator, we can program or reprogram it with various actuation modes as shown in Figure 2.7a. The programming of actuators with different modes shares similar procedure as programming the ss-LCE materials: First, the actuator was heated up to 180 °C for 20 mins and cooled down to room temperature; Then, certain deformation was applied to the actuator and kept for 24 hours. The heating time of 20 mins and the time for holding the deformation (24 hours) were determined through parametric studies (Figure 2.3). Detailed information for different modes programming is described as following:

(1) Contraction mode: we first heated the actuator up to 180 °C and cooled it down. Then we fixed one end of the actuator using Kapton tape (3M company) and manually applied a uniaxial stretch with the stretch ratio of 1.5 to the actuator. We then fixed the other end using Kapton tape to hold the stretch for 24 hours.

(2) Bending mode: we first programmed the actuator with a uniaxial stretch of 1.5 as described above. Then we adhered Kapton tape with width of 8 mm and length of 3 cm to one surface of the actuator to form a bilayer structure.

(3) Shear mode: we first heated the actuator up to 180 °C and cooled it down. Then we sheared actuator with a shear angle of 30° by using a simple customized device. We then held the shear deformation in the actuator for 24 hours.

2.2.6 Actuation performance of its contraction mode

We first programed the soft actuator with the contraction mode, which is one of the most important actuation modes for an actuator. The programming process can be found in the previous section. To quantitively characterized the actuation performance determined by Joule heating of the heating wires, we performed isotonic (constant load) and isometric (constant displacement) tests to measure the actuation strain and stress as shown in Figure 2.8a. We used external power supply (Keysight E3642A) to apply voltage to the actuator. We first measured the surface temperatures of the actuator with different applied voltage (2 V, 3 V and 4 V for 120 s) using infrared camera (FLIR E75-42), Figure 2.8b shows the maximum temperature on the surface of the actuator as a function of time. Once the voltage was turned on, the surface temperature started increasing and then reached to a plateau value. The plateau value of the maximal surface temperature increased from 83 °C to 140 °C and to 191 °C when we successively increased the voltage from 2 V to 3 V and to 4 V. When we turned off the voltage, the surface temperature gradually decreased to room temperature within 180 s. Although higher voltage resulted in relatively higher surface temperature with shorter period, we needed to make sure that the actuating temperature of the actuator is below 180 °C to prevent erasing the programmed actuation.

To measure the actuation strain of the actuator, we applied three different levels of voltages (2 V, 3 V and 4 V) for 120 s. The actuator was subjected to 0.196 N axial load (20 g weight) to keep it straight as shown in Figure 2.8a. The actuation strain can be defined as $\varepsilon=(L-l)/L\times100\%$, where L is the length of the actuator in the initial state while l is the length in the actuated state.

We measured the actuation strain of the actuator by processing the photos taken by the digital camera (Canon 80D) using ImageJ. As shown in Figure 2.8c, the actuation strain increased and reached the maximal value after 60 s for all three different voltages. Specifically, when the voltage was 3 V, 23% actuation strain could be generated within 45 s. In addition, the response of the soft actuator was faster as we increased the applied voltage. An average strain rate of 0.15% s^{-1}, 0.75% s^{-1} and 1.5% s^{-1} could be realized as the applied voltage was 2 V, 3 V and 4 V, respectively. Furthermore, the actuation stress could be measured by fixing the length of the actuator (Figure 2.8a) while applying different levels of voltage (2 V, 3 V and 4 V) as shown in Figure 2.8d. We measured the actuation stress of the actuator by using the Instron Universal Testing System (5965 Dual Column Testing Systems: Instron) with 10 N loading cell. Similarly, for a given value of voltage, the actuation stress increased from zero to the maximum value after the voltage was turned on, and gradually dropped to zero when the voltage was turned off. Specifically, a maximum actuation stress of 0.2 MPa could be produced by the actuator when the voltage was 3 V. The actuator could also generate cyclic actuation when the voltage was turned on and off cyclically. The actuation stress generated by the actuator depended on the magnitude as well as the duration of the voltage when the voltage was turned on.

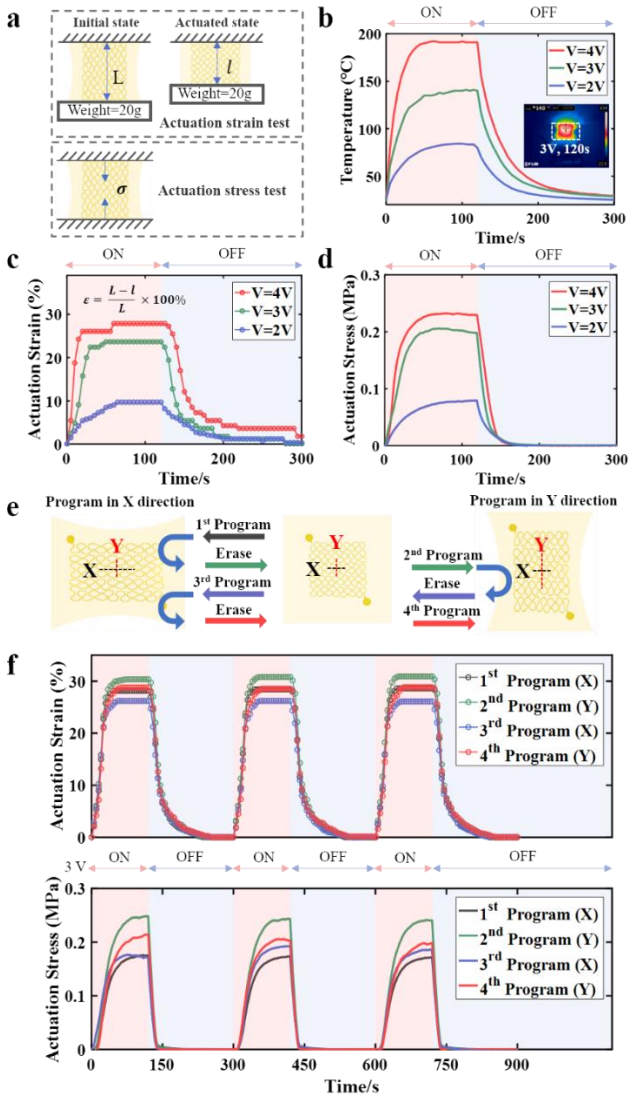

Figure 2.8: Characterizations of ss-LCE based soft actuator.

a Schematics of the experiment set up for the characterization of actuation strain and actuation stress of a ss-LCE actuator. **b** Maximum surface temperature of the actuator as a function of time during contraction (voltage on) and recovery (voltage off), the inset is the infrared (IR) image showing surface temperature distribution of the actuator when the applied voltage is 3 V at 120 s. The dash lines in the inset shows the area of the actuator. **c** Actuation strain of the actuator as a function of time under three different levels of applied voltages :2 V, 3 V, 4 V. The actuator was subjected to 0.198N load (20 g weight) to keep the actuator straight. **d** Actuation stress of the actuator as a function of time for three different levels of applied voltages: 2 V, 3 V, 4 V. **e** Schematics of reprogramming the actuator. Uniaxial contraction along X or Y direction was alternately reprogrammed and erased for four times in the same actuator. **f** Actuation strain and actuation stress along either X or Y direction as a function of time after the actuator was programmed or reprogrammed.

2.2.7 Reprogrammability of the ss-LCE based actuator

We next demonstrated the reprogrammability of the actuator. The actuator was first programmed with uniaxial contraction mode along X direction, as shown in Figure 2.8e. We then heated the actuator to 180 °C in an oven for 20 mins to erase its contractive actuation in X direction and reprogrammed it with contractive actuation along Y direction. We further erased the contractive actuation in Y direction and repeated above reprogramming and erasing process. The active contraction along two orthogonal directions can be alternatively introduced into the actuator as shown in Figure 2.8f. Before reprogramming, the actuator programmed for 1st time could generate an actuation stress of 0.17 MPa in isometric condition with an applied voltage of 3 V and its actuation strain under isotonic condition could reach 28 % after the voltage was turned on for 120 s. After each reprogramming, both actuation strain and stress of the actuator maintained almost unchanged, indicating its very robust reprogrammability.

2.2.8 Reprogrammability of the ss-LCE based actuator between multiple modes

We then demonstrated the multi-mode programmability of the actuator. In the experiment, we programmed an actuator with three different actuation modes: contraction mode, bending mode and shear mode. The detailed steps of programming ss-LCE actuator can be found in the Experimental Section. As shown in Figure 2.9a, the actuator with contraction mode could lift a weight of 60 g up by 6 mm (80 times of its own weight) with an applied voltage of 3 V.

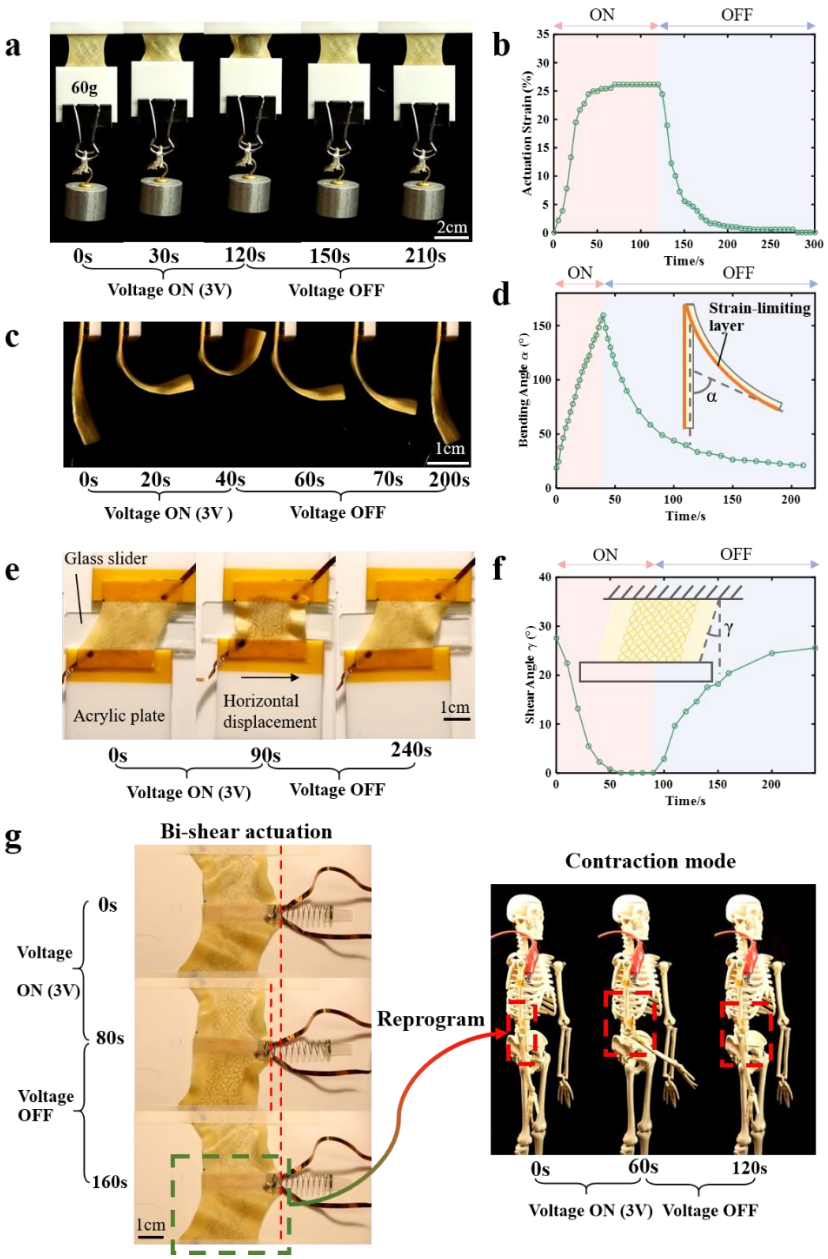

Figure 2.9: Multiple actuation modes can be programmed in the actuator.
a Contraction mode of ss-LCE actuator. The actuator could lift a weight of 60 g when a voltage of 3 V was applied to the actuator. **b** The actuation strain of the actuator as a function of time. **c** Bending mode can be realized by attaching strain-limiting layer (Kapton tape) to a contractive actuator. **d** Bending angle (defined in the inset) as a function of time with the applied voltage of 3V for 40s. **e** Shear mode of the actuator. **f** Shear angle (defined in the inset) as a function of time with the applied voltage of 3V for 90s. g, A pair of actuators with shear mode could be combined to one actuator to generate the bi-shear actuation. The actuator with shear mode actuation could be erased and then reprogrammed with contraction mode. This newly generated contractive actuator could lift up a skeleton arm.

Figure 2.9b shows its actuation strain as a function of time. It took 45 s for the actuator to reach the actuation strain of 25%, which was comparable to the case shown in Figure 2.9b with the weight of 20 g. As shown in Figure 2.9c, the actuator with bending actuation can be achieved by attaching strain-limiting layer (Kapton tape, 3M Company) to a contractive actuator. As the voltage was applied to the actuator, bending actuation can be produced as shown in Figure 2.9c. The bending angle defined in Figure 2.9d was measured as a function of time. The actuator was not straight as it was fabricated and had an initial bending angle of 20°. When we applied a voltage of 3 V, the bending angle of the actuator increased from 20° to 160° within 40 s. After we turned off the voltage, its bending angle gradually reduced to its initial value within 180 s.

We also studied the actuator with shear mode as shown in Figure 2.9e. In the experiment, two acrylic plates were attached to the two parallel edges of the actuator. One of the plates was fixed and the other one was allowed to move horizontally along the glass slider. When the voltage was turned on, large shear deformation could be generated by the actuator (Figure 2.9e). When the voltage was turned off, the actuator gradually recovered back to its initial shape. In Figure 2.9f, we plot the shear angle of the actuator as a function of time when the voltage was first turned on for 90s and then turned off for 150s.

At last, we showed the possibility of transforming the actuator with one actuation mode to another. We first programed a pair of actuators with shear mode, and then combined them into one actuator to generate bi-shear actuation as shown in Figure 2.9g. The free end of the new actuator was able to pull a spring by 4.8 mm with a voltage of 3V applied to both two actuators for 90 s.

We next took one of the actuators out and reprogrammed it with contraction mode. As shown in Figure 2.9g, after reprogramming, the actuator could lift up a skeleton arm within 60 s with applied voltage of 3V. Such significant transformation of actuation mode in an actuator can be very useful in many engineering applications.

2.3 Conclusion

In conclusion, we have successfully constructed ss-LCE based soft actuator, which exhibits various actuation modes after programing or reprogramming. We have also characterized different actuation modes such as contraction, bending and shear of the ss-LCE actuator. Most existing soft actuators have fixed actuation modes after they fabricated. In contrast, we have shown that both erasing and reprograming an actuation mode in the newly developed soft actuator are facile. Moreover, the actuation of the soft actuator can be electrically controlled with low voltage, which enables its simple integration with most existing control systems with low cost. We hope the newly developed reprogrammable soft actuator can find its wide applications in constructing diverse soft active structures.

Acknowledgements

Chapter 2, in full, is a reprint of the material as it appears in "Electrically controlled soft actuator with multiple and reprogrammable actuation modes", *Advanced Intelligent Systems* 2 (2020): 1900177, by Yang Wang, Zhijian Wang, Qiguang He, Prajval Iyer, Shengqiang Cai. The dissertation author was the primary investigator and first author of this paper.

Chapter 3 Liquid Crystal Elastomer based dexterous artificial motor unit

3.1 Introduction

Intuitively, the function of a natural muscle is converting chemical energy to mechanical work to enable various activities of animals, behaving as an actuator. Nevertheless, abundant evidence from biological studies have recently demonstrated that muscle works more like a tunable and active materials [57], which can function as an actuator, a brake, or a nonlinear spring [58]. From energy perspective, natural muscle can produce mechanical work as an actuator, actively dissipate energy as a brake and store/release energy as a spring [59]. The switch between each function is rapid and often controlled by neural signals [60, 61]. A motor neuron and the muscle fibers innervated by it form a motor unit [62] which enables the multifunctionalities of a natural muscle and is essential for the dexterous motion of animals.

The recent decade has witnessed the rapid progress in creating diverse soft robots [1, 2, 7]. Nevertheless, the dexterity of most soft robots still does not match that of the simplest animals in nature. Building an autonomous and dexterous soft robot requires an artificial motor unit with great performances, including a fast actuation response, a large actuation strain/stress, high flexibility, and effective/efficient conversion of sensing signals to control signals dictating the activities of the unit, analogous to the motor unit of most animals. Despite the great advancement

in developing various artificial muscles and control methods [9, 10, 63, 64], investigations on the integrated dexterous artificial motor unit are still limited.

It has been well recognized that excellent performance of individual elements does not guarantee their compatibilities in an integrated system and hence its superior performance. For instance, actuation of many artificial muscles previously developed is driven by environmental heating [4, 64], which makes their control in a robotic system highly challenging. Other widely explored artificial muscles are responsive to light [55, 65], magnetic field [66, 67], humidity [68] or driven by high voltages [11, 69]. A compact design of an artificial motor unit using those responsive materials also remains difficult.

To construct an artificial motor unit for dexterous soft robots, we need a soft actuating material with a fast response and to be electronically controllable. Therefore, in this study, we developed a gold-coated ultrathin liquid crystal elastomer (LCE) film, together with the electronic control systems, to build an artificial motor unit. Recently, LCE has been extensively investigated as a means of soft actuators. Due to the phase transition of liquid crystal mesogens in the elastomer, LCE generates large and reversible actuation, resembling the contractile behavior of biological muscles [13, 41, 44]. However, most of the LCE-based actuators show slow responses [13, 39, 63, 64] (the response time is often around or even above 1 min), like most thermally driven actuators such as shape memory alloy/polymer-based ones [70]. Light powered azobenzene-doped LCE or LCE fiber coated with a light-absorbing material [65] can respond much faster, which, however, is hard to be integrated with a compact control system.

To construct an electronically controllable and fast-response LCE-based actuator, in this study, we sputter a gold film with tens of nanometer thickness on the top of a thin pre-stretched LCE film with a thickness around 10 μm. The combination of an ultrathin LCE film and gold film coating dramatically decreases its thermal inertia and therefore increases the response speed, comparing with most of previously reported thermally driven LCE actuators [64]. We further integrate the LCE-based actuator with an electronic control system to construct the artificial motor unit. Finally, with external sensors integrated, we can build an artificial neuromuscular system, enabling the mimicry of voluntary movements of animals as shown in Figure 3.1.

In a biological motor unit, the motor neurons receive signals either from the central nervous system or the sensory receptors and then control the motion of the associated muscle fibers based on the received signals (Figure 3.1A). In the artificial neuromuscular system developed in the current study (Figure 3.1B), we regard the thin gold-film-coated LCE film with a connected MOSFET as a motor unit. The voltage pulses generated by an electronic controller are similar to the action potentials produced by motor neurons. The MOSFET is the power amplifier and signal receiver, in which its gate receives the voltage pulses as control signals, mimicking the synapse of motor neurons. By tuning the frequency and the time width of the voltage pulses, different dynamic behaviors of an artificial motor unit can be achieved, which enables the controlling strategies of rate coding [71], as employed by animals.

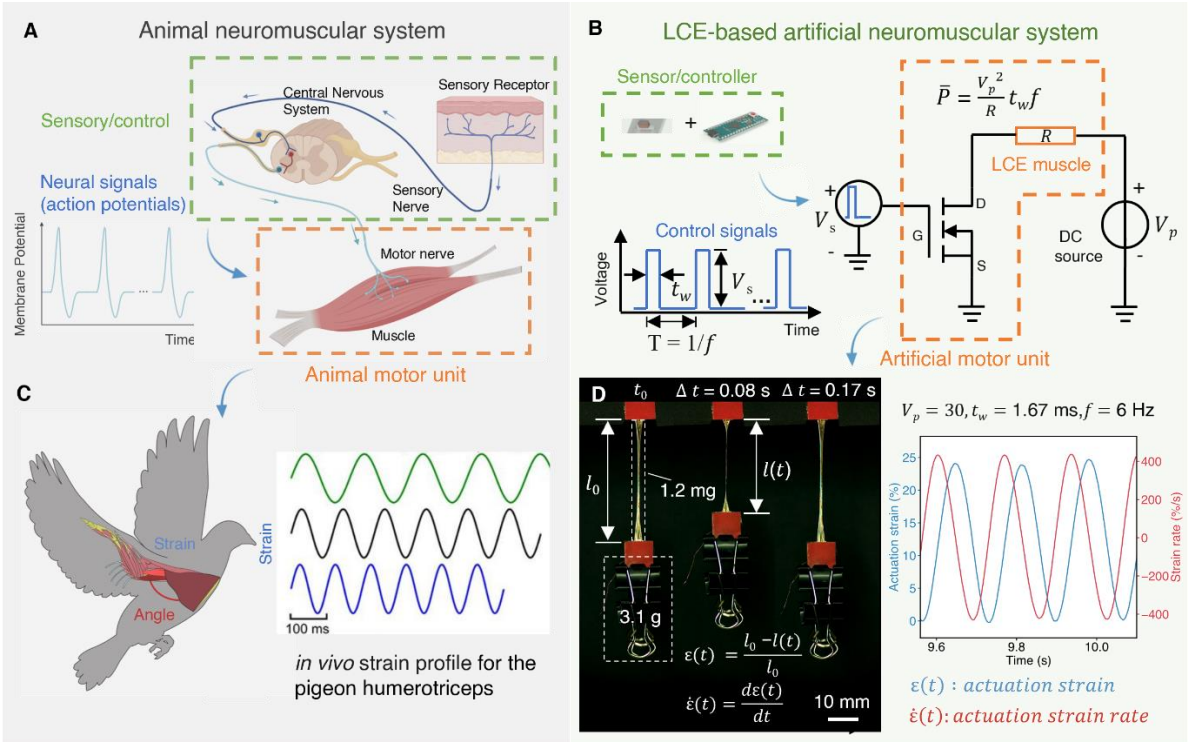

Figure 3.1: Biomimetic design of an LCE-based artificial motor unit.
(**A**) Schematics of neuromuscular systems of an animal: after receiving a signal from sensory receptor, a central nervous system generates a signal to control the motion of muscle. (**B**) Biomimetic design of an LCE-based artificial neuromuscular system. The electrical potential (V_s) is control signal and MOSFET is used to amplify the input power through connecting the LCE actuator with a DC source (V_p) (**C**) Schematics of pigeon humerotriceps and its time-dependent strain profile during flying [61]. (**D**) Cyclic oscillation of LCE-based motor unit with a frequency of 6 Hz, which can lift a weight of 2500 times of its own weight within 0.08 s and recover within another 0.08 s, outputting a mechanical power density of 1360 W/kg close to or even outperforming flight muscles of animals.

Besides the control strategies, the real time performance of the muscle is essential to many applications. Similar to the in vivo strain profile of an animal muscle as shown in Figure 3.1C, we demonstrate that our artificial motor unit can generate large deformation with an actuation strain of around 25% within 0.08 s under an applied stress of 1.5 MPa (Figure 3.1D). The LCE-based motor unit can output mechanical work with a power density of 1360 W/kg, which is several times

of the power density of mammalian skeleton muscles (20~300 W/kg) [72] and even insect flight muscles (400~800 W/kg) [73]. Overall, the similarities between the artificial neuromuscular system developed here and that of animals include their actuation dynamics, versatile control strategies and the compact integration of neurons and muscles. We hope that the artificial neuromuscular system developed in this article can inspire and enable the design of novel dexterous soft robots of various forms. Moreover, it may provide an experimental platform for biologists to investigate the physics of the various activities of animals.

3.2 Fabrication of the LCE-based motor unit

3.2.1 Preparation of the LCE precursor for the fabrication of the LCE thin film

We use the following chemicals to synthesize the LCE thin film (as shown in Figure 3.2): (1,4-bis-[4-(3-acryloyloxypropyloxy) benzoyloxy]-2-methylbenzene) (RM257) (Wilshire company, 95 %) as liquid crystal mesogens; 2,2'-(ethylenedioxy) diethanethiol (EDDET; Sigma-Aldrich; 95%) as chain extender; pentaerythritol tetrakis (3-mercaptopropionate) (PETMP, Sigma-Aldrich, 95%) as crosslinker; dipropylamine (DPA, Sigma-Aldrich, 98%) and (2-hydroxyethoxy)-2-methylpropiophenone (HHMP; Sigma-Aldrich; 98%) as catalysts. All the chemicals were used as received without further purification.

To obtain the ultrathin LCE film, we first fabricated the 1st cross-linked LCE film. We prepared the 1st cross-linked LCE following the previously reported work [74] with modification. To get the LCE film, liquid crystal mesogens RM257 (10.000 g, 16.65 mmol) was firstly added into toluene, and the mixture was heated at 85°C. The photo-initiator HHMP (0.077 g, 0.3 mmol)

was added into the mixture. Then, we added 1.902 g (9.9 mmol) of spacer EDDET, 1.529 g (2.9 mmol) of cross-linker PETMP, and 0.032 g (0.3 mmol) of catalyst DPA into the solution.

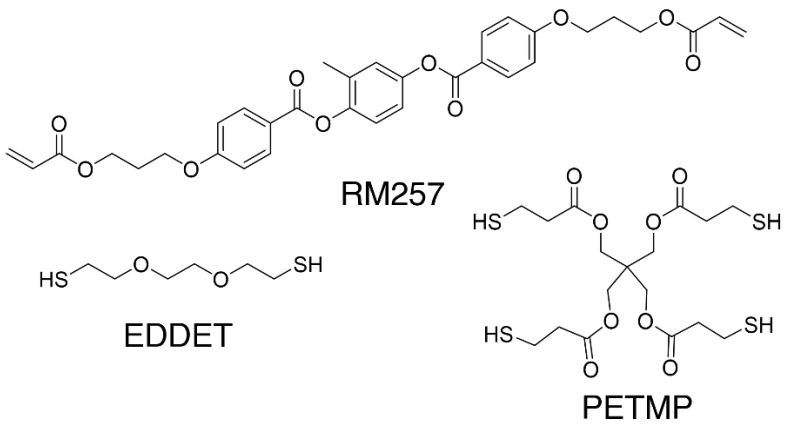

Figure 3.2: Molecular structure of the chemical components for synthesizing LCE thin film. RM 257 is the liquid crystal mesogens, EDDET is chain extender, and PETMP is the crosslinker. All the components are dissolved in toluene to form the liquid precursor.

3.2.2 Compression-assisted molding technique and characterization of the thickness

After stirring and degassing of the LCE precursor, we then used the compression-assisted molding technique to get the 1st cross-linked ultrathin polydomain LCE films as discussed in this section. To fabricate the ultrathin polydomain LCE film, we sandwiched certain amount of LCE precursor solution (mixture of EDDET, PETMP, RM 257 and catalyst in toluene) between two glass plates (24 cm by 24 cm) and put an extra weight on the top glass plate as shown in Figure 3.3A to provide compression. We then kept the whole structure in dark environment at room temperature for 24 hours waiting for the chemical synthesis to finish. After that, we removed the top glass plate and left the thin film exposed to air in the dark environment to evaporate the residual solvent for another 24 hours. After that, we obtained the 1st cross-linked ultrathin polydomain LCE

films as shown in Figure 3.3B. Moreover, the monodomain LCE film with thickness of 50 µm is obtained using standard molding technique [13] with a spacer of 0.1 mm during LCE synthesis.

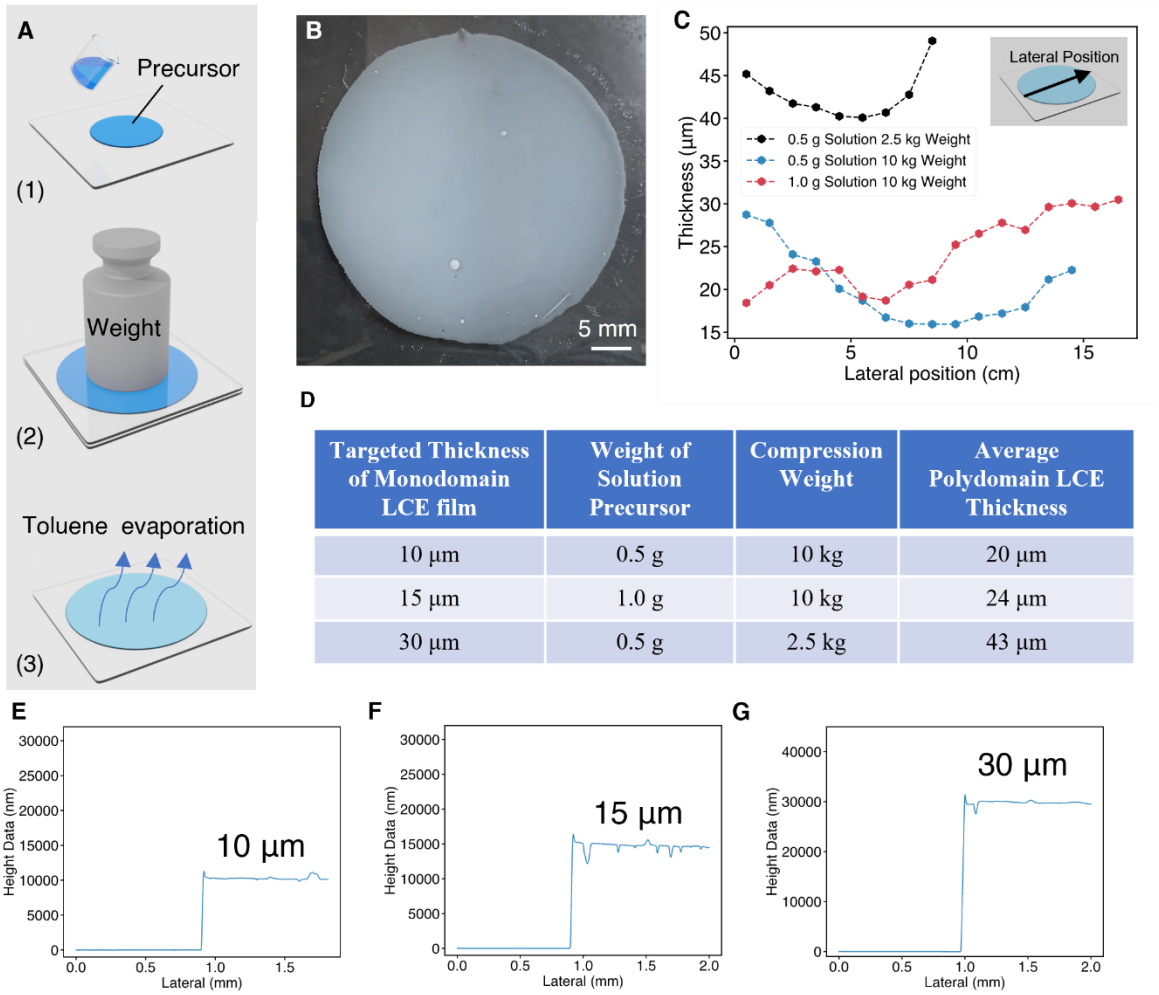

Targeted Thickness of Monodomain LCE film	Weight of Solution Precursor	Compression Weight	Average Polydomain LCE Thickness
10 µm	0.5 g	10 kg	20 µm
15 µm	1.0 g	10 kg	24 µm
30 µm	0.5 g	2.5 kg	43 µm

Figure 3.3: Compression-assisted LCE thin film molding process and its thickness measurements. (**A**) Compression-assisted fabrication process of a thin LCE film: (1) we pour the liquid LCE precursor on the top of one glass plate; (2) we gently cover the LCE precursor with another glass plate and put a weight on top to provide compression; (3) after the chemical synthesis is done, we remove the top glass plate and evaporate away the solvent (toluene) at room temperature in the dark environment for 24 hours. (**B**) Image of a polydomain LCE thin film (after toluene evaporation). (**C**) Thickness distribution along the lateral direction of LCE thin film (polydomain) under different fabrication conditions. (**D**) The parameters for obtaining targeted thickness of an LCE thin film. (**E**)-(**G**) Thickness measurements of the monodomain LCE thin films (after being stretched and UV cured) with different compression weights. The data is collected using stylus profiler (Dektak XT).

To measure the thickness of a polydomain LCE film, we cut it along its diameter (as in Figure 3.3B). We measured the thickness of the LCE film at different positions along the diameter using profiler Dektak XT as shown in Figure 3.3C. Different combinations of the amount of precursor of the LCE solution and the weight of the extra mass result in different thicknesses of the LCE thin film as shown in Figure 3.3C and Figure 3.3D.

3.2.3 Fabrication of monodomain LCE thin film

We first fabricated the dog-bone shape 1st cross-linked polydomain LCE films through laser cutting (as shown in Figure 3.4). They were then stretched to 2.75 times of its original length to align the mesogens. We then placed the stretched LCE thin films under UV light (365nm) and curing for 1 hour to finish the 2nd cross-linking and get the monodomain LCE films.

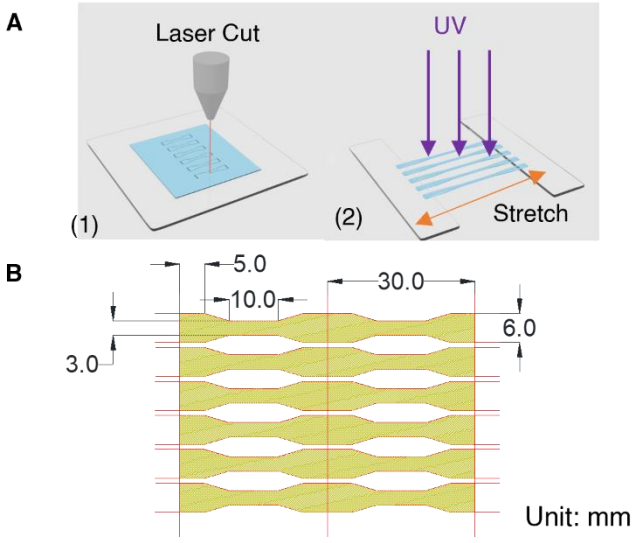

Figure 3.4: Preparations of LCE films before the sputtering of the gold film.
(**A**) The LCE thin film (polydomain) can be patterned by laser cutting with desired shapes. The monodomain LCE can be fabricated by applying stretch ($\lambda = 2.75$) and UV irradiation to initiate the second crosslinking reaction of LCE. (**B**) Laser cutting profile of polydomain LCE thin films.

3.2.4 Characterization of the monodomain LCE thin film

We next performed systematic characterizations of the monodomain LCE thin film. We first confirm the alignment of the mesogens inside the LCE thin film. As shown by Figure 3.5, the two images show the monodomain LCE thin film observed at two different angles with respect to the analyzer and polarizer. We observed the minimum light transmittance once the orientation of the mesogens inside the LCE thin film shared same direction as analyzer/polarizer, and it was shown as purely dark in Figure 3.5.

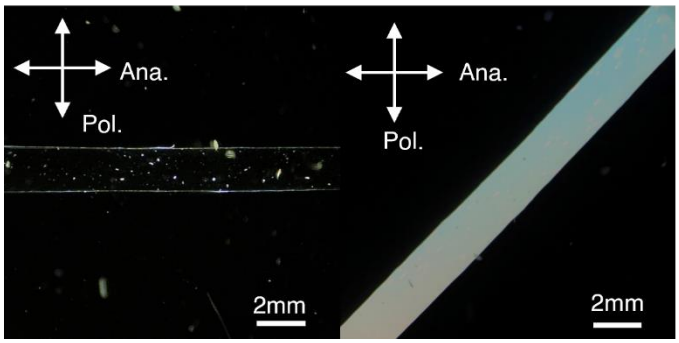

Figure 3.5: The alignment of the mesogens in monodomain LCE can be confirmed by microscopy images in dark field.

We increased the crosslink density of the LCE to increase the actuation stress, so that the decreasing of actuation force when making the whole structure thinner was compensated. We then study the thermal-mechanical properties of the new designed LCE material as discussed below.

As shown in Figure 3.6, we performed the differential scanning calorimetry (DSC) measurement using a Discovery DSC 250 (TA instruments) in the nitrogen atmosphere. The 2.1 mg monodomain LCE sample was sealed in the aluminum pans. The heating and cooling temperature range was between −35° and 150°C with a scanning rate of 5°C/min. With the given

DSC analysis results, the glass transition temperature of the LCE is around 4 °C. However, the phase transition temperature is not detectable due to the high crosslinking density of the LCE used in the current study, which is consistent with previous reports [75].

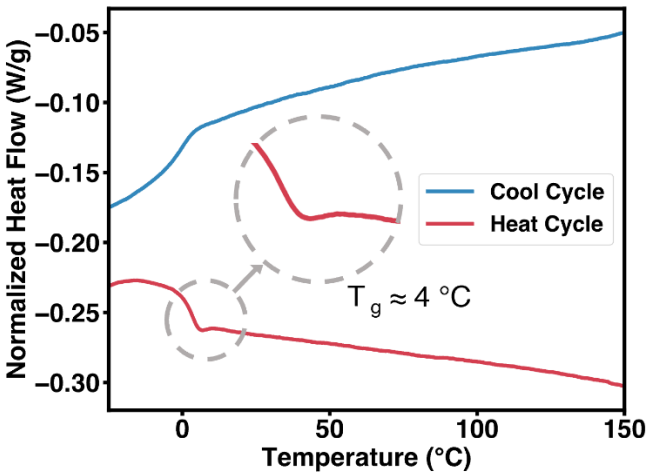

Figure 3.6: DSC analysis of monodomain LCE thin film.
The glass transition temperature T_g of the sample is around 4°C, and no clear nematic-isotropic phase transition temperature is observed due to the high crosslink density of current recipe.

Meanwhile, we also conducted the uniaxial tensile tests of the monodomain LCE (before gold sputtering) at different temperatures using a Dynamic Mechanical Analysis (DMA) system (RSA-G2, TA Instruments). All the monodomain LCE samples share the same dimension of 10 mm × 1.8 mm × 15 μm. We adopted a strain rate of 1%/s for all the tests. The testing temperatures were chosen between 25 °C (room temperature) and 170 °C. Representative tensile tests results are shown in Figure. 3.7 and Figure. 3.8. The mechanical test results of the LCE film at room temperature provides us some guidance for determining the amount of pre-stretch during the sputtering process. It also provides us an idea of the maximum load that the motor unit can withstand without breaking the sputtered gold film. The high-crosslinked LCE film shows a high

tensile strength of 150 MPa at room temperature (Figure 3.7). As shown in Figure 3.7B, LCE thin film with self-weight of 0.5 mg can withstand an applied load of 160 g (applied stress of 10.5 MPa), which is 320000 times of its self-weight. The LCE thin film also shows high strength of above 10 MPa at 100 °C (Figure 3.8). It is noted that the strength of the LCE decreases as the temperature increases.

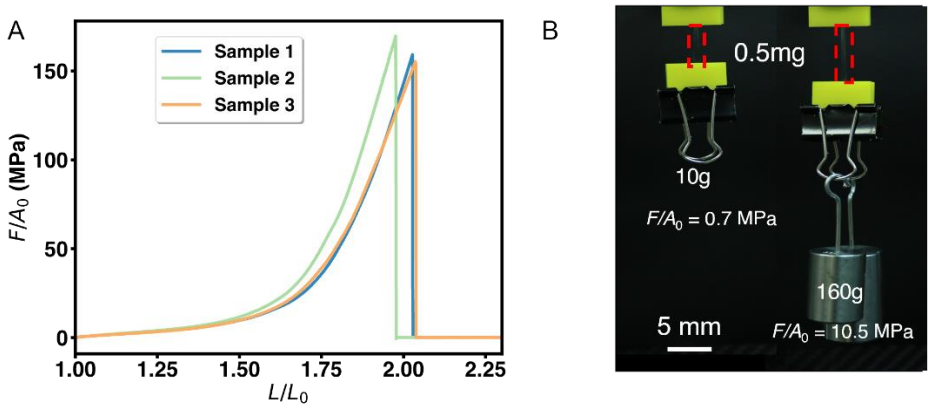

Figure 3.7: Mechanical performance of an LCE thin film at room temperature.
(**A**) Tensile test results of LCE thin films (10 mm × 1.8 mm × 15 μm). (**B**) Experimental photos showing high strength of LCE thin film at room temperature.

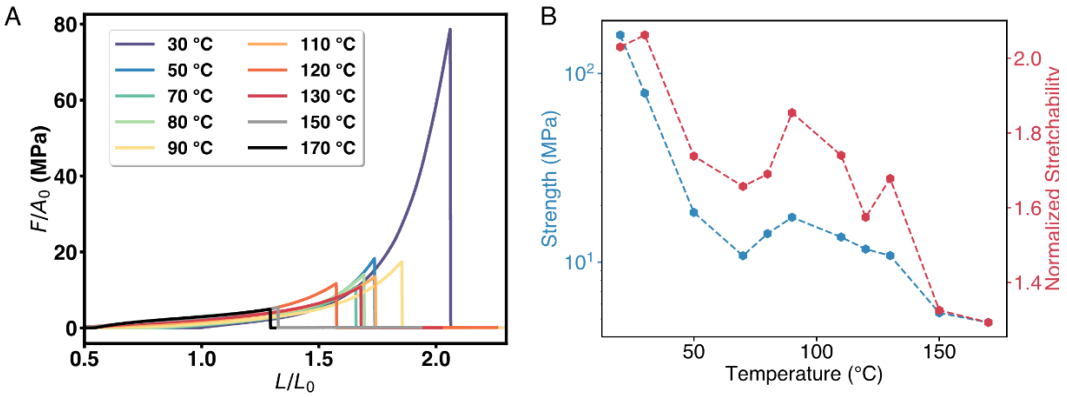

Figure 3.8: Mechanical performance of LCE thin film at different temperatures.
(**A**) Tensile test results of the LCE thin film (10 mm × 1.8 mm × 15 μm) at different temperatures. (**B**) Strength and stretchability of the LCE film (with respect to L_0 at room temperature) at different temperatures.

Furthermore, the actuation performance (both stress and strain) of the LCE film can also be obtained from the test results following the analysis method described in Figure 3.9. We then have the actuation strain of the LCE film under different temperatures with different applied stress as in Figure 3.9C and the actuation stress of the LCE film under different temperatures with different pre-stretches as in Figure 3.9E.

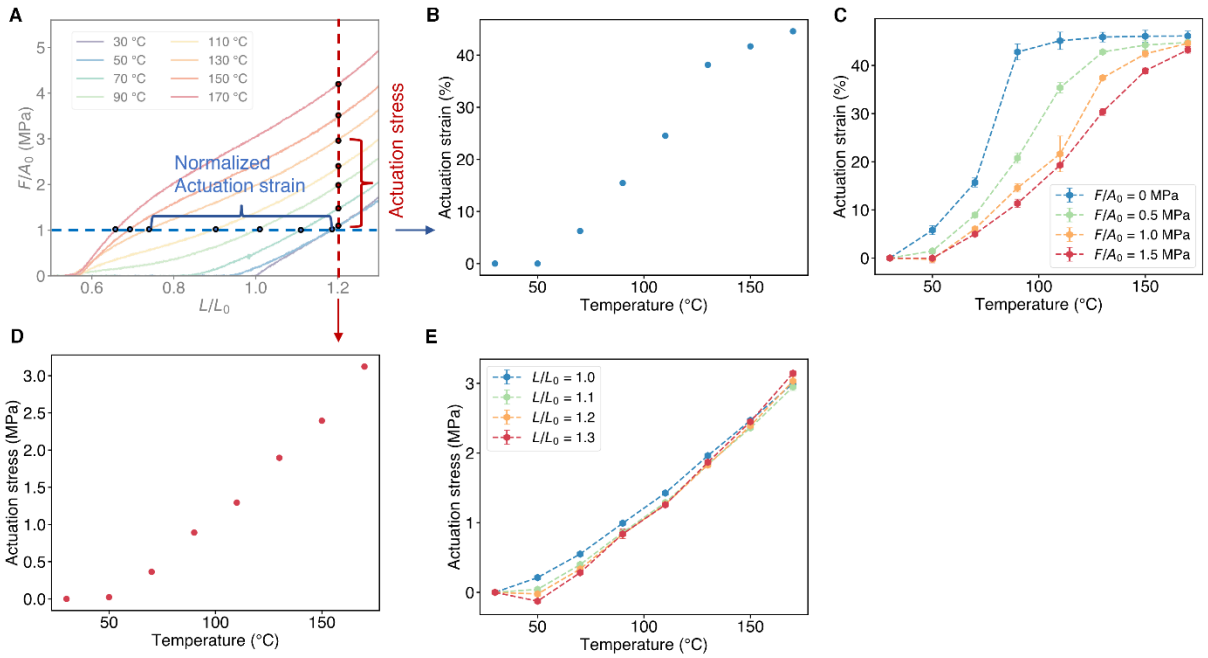

Figure 3.9: Measurement of actuation strain and actuation stress of an LCE film from the tensile test under different temperatures.
(**A**) The method of obtaining the actuation stress of the LCE film at a fixed L/L_0 ratio and the actuation strain at a fixed stress. (**B**) Actuation strain versus temperature when applied stress is 1 MPa. (**C**) Actuation strain versus temperature of LCE thin films at different applied stresses, extracted from the tensile test results of three different monodomain samples. (**D**) Actuation stress versus temperature when L/L_0 ratio is fixed at 1.2. (E) Actuation stress versus temperature of LCE thin film at different fixed pre-stretch (L/L_0), extracted from the tensile test results of three different monodomain samples.

3.3 Construction of LCE-based artificial motor unit

3.3.1 Fabrication of the LCE-based artificial motor unit

With the fabricated ultrathin LCE film, we then integrated the heating element with the LCE film to make it electronically actuatable. Previous work usually embedded heating wires inside the LCE [13, 76-79], which increases the overall thickness of the actuator. Instead, we coated a thin layer of gold on the surface of an LCE film, as shown in Figure 3.10A, with three steps: (1) We sputtered one layer of gold (~40 nm) on top of a pre-stretched LCE film. The surface of the gold film on top of the LCE after sputtering was flat without releasing the pre-stretch. (2) Once the pre-stretch in the film was released, the gold film coating formed a wrinkled configuration, which enabled its large stretchability. (3) After we obtained the LCE film with a gold film coating, we attached soft electrodes on its two ends. To achieve a low contact resistance, good stretchability, and high robustness of the electrodes against temperature changes, we sandwiched the two ends of the LCE film between two conductive tapes and a thin PET film (Figure 3.10A). After integrating a MOSFET with the coated LCE film, we finally constructed an LCE-based motor unit.

The detailed fabrication process is discussed as the following procedures. Without releasing the stretch of the monodomain LCE (as shown in Figure 3.4A), the UV-cured LCE thin films were placed inside a DC magnetron sputter deposition system (Denton Discovery 18) with a base pressure of 4.99×10^{-6} Torr. The working gas Ar pressure is around 2.5×10^{-3} Torr during sputtering. We first deposited a thin layer of Cr (thickness: ~5 nm) as adhesion layer onto the LCEs and then deposited Au (thickness: ~40 nm) on top of Cr immediately without breaking the vacuum. The DC

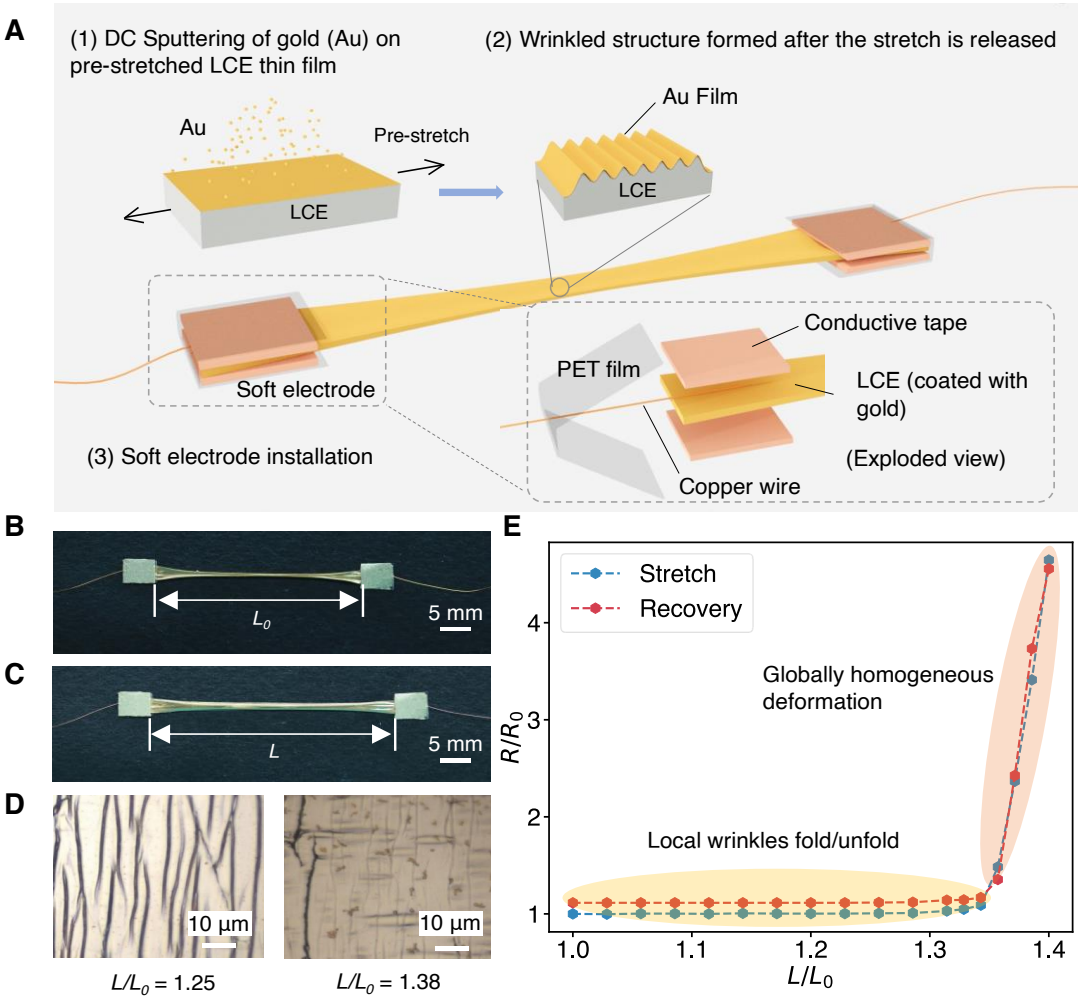

Figure 3.10: Fabrication of LCE-based motor unit with wrinkled gold film coating.
(**A**) Schematics showing three main fabrication steps. **(B)** and (**C**) Photos of the LCE motor unit in its free-standing state and stretched state. (**D**) Optical microscopic images of the surface of gold film under different stretches. When the applied stretch is small, surface wrinkles remain; when the applied stretch is large, surface flattens. (**E**) Electrical resistance of gold film under different stretches. When the applied stretch is less than 1.35, the electrical resistance remains unchanged as the stretch increases, corresponding to the process of wrinkle flattening and indicating a safe operation window of the applied stretch.

power was set as 200 W for sputtering of both Cr and Au. After sputtering, we released the fixed stretch, the contraction of the LCE film due to elastic deformation will help the gold film forming the wrinkled structure as shown in Figure 3.10A. We then installed the soft electrode to connect

the gold film with copper wirings for further connection to the external power source. The soft electrode consists of isotropic conductive tape (3M 9707) and 12.7 μm PET film as protection package layer. After the soft electrodes were installed, we then connected the LCE/gold film with a MOSFET Module (IRF540) to magnify the power and finally constructed an LCE-based artificial motor unit. During the later test, we used DC power source (Dr. Meter PS-305DM) to provide the heating power (V_p in Fig. 1B), and a function generator (Keysight, 33500B) to generate periodic voltage pulses as control signals (V_s in Figure 3.1B).

Figure 3.10B and Figure 3.10C show the images of the fabricated artificial motor unit before and after stretching, in which L_0 denotes the original length of the film without bearing any load and heating, and L is its length after stretching. The morphology of the surface of the LCE film at different stretched states is shown in Figure 3.10D. The surface flattens from a wrinkled state as the stretch increases. To examine the stretchability of the coated gold film, we stretched the film up to 1.4 times of its initial length and then gradually released the stretch, during which we measured the electrical resistance of the gold film as shown in Figure 3.10E. The electrical resistance of the gold film remained constant if the stretch was less than 1.35 ($L/L_0 < 1.35$), corresponding to the flattening process of the wrinkled configuration. If the stretch was beyond 1.35 and smaller than 1.4, the electrical resistance linearly increased with the applied stretch, which was caused by the increase of the strain in the gold film. It is also noted that electrical resistance of the gold film recovered to its original value once the applied stretch was reduced below 1.35, indicating that the gold film can be stretched by 1.4 times without damaging.

3.3.2 Morphology characterization of the wrinkled gold coating layer

The morphology of as-sputtered gold film fabricated on top of the ultrathin LCE film is shown in Figure 3.11. The gold film is flat before releasing the pre-stretches. We also verified the thickness of the gold film by sputtering the gold on top of a glass slide with same sputtering parameters as we used for fabricating the LCE-based motor unit. The thickness of around 40 nm was obtained through a surface profiler (Dektak XT) as shown in Figure 3.12.

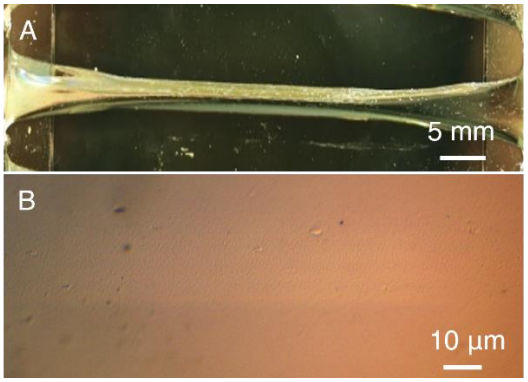

Figure 3.11: Pre-stretched monodomain LCE thin film with sputtered gold.
(**A**) Image of a pre-stretched (stretch of 1.4) LCE thin film (thickness of ~10 µm) with coated gold (thickness of 40 nm) film. (**B**) Microscopic images (Zeiss) of smooth surface of as-sputtered 40 nm gold film on top of the pre-stretched monodomain LCE thin film.

We then examined the wrinkled morphology of the gold film on top of the LCE film (after releasing the pre-stretches) using both optical microscope (Zeiss) and scanning electron microscope (FEI SEM) as shown in Figure 3.13. We performed the surface roughness measurements with an optical surface profiler (Filmetrics Profilm3D) as shown in Figure 3.13E. Because the gold was sputtered on surface of the pre-stretched LCE sample, the sample coils up along its width direction when it is released from the pre-stretched state. A small stretch to uncoil the sample was applied for its surface morphology characterization.

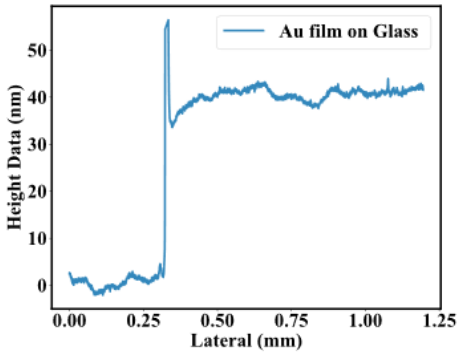

Figure 3.12: Thickness measurement of the sputtered gold film using surface profiler.

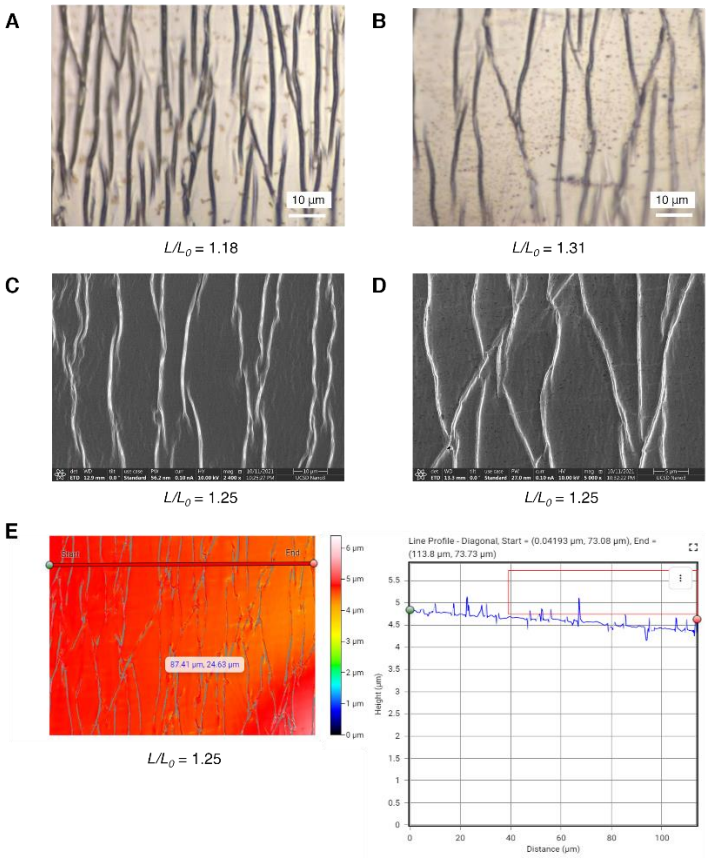

Figure 3.13: Characterization of the wrinkled surface morphology of a sputtered gold film. (**A**)-(**B**) Optical microscope images show the wrinkled morphology of gold film on the top of a LCE thin film. (**C**)-(**D**) SEM images show the wrinkled morphology of gold film on the top of a LCE thin film. A small stretch of 1.25 is applied to flatten the film while taking the images. (**E**) Height profile showing the wrinkled surface of Au/LCE structure obtained from optical surface profiler. (Filmetrics Profilm3D). A small stretch of 1.25 is applied to flatten the film during the measurement.

3.4 Quasi-static behavior of the LCE-based motor unit

3.4.1 Self-defined algorithms to obtain actuation strain from experimental videos

For all the actuation strain measurements of the LCE-based motor unit in the following text, we will use a self-defined image processing algorithm (as shown in Figure 3.15) to help us calculate the actuation strain from experimental videos of cyclic contractions of the motor unit upon different voltage stimulations.

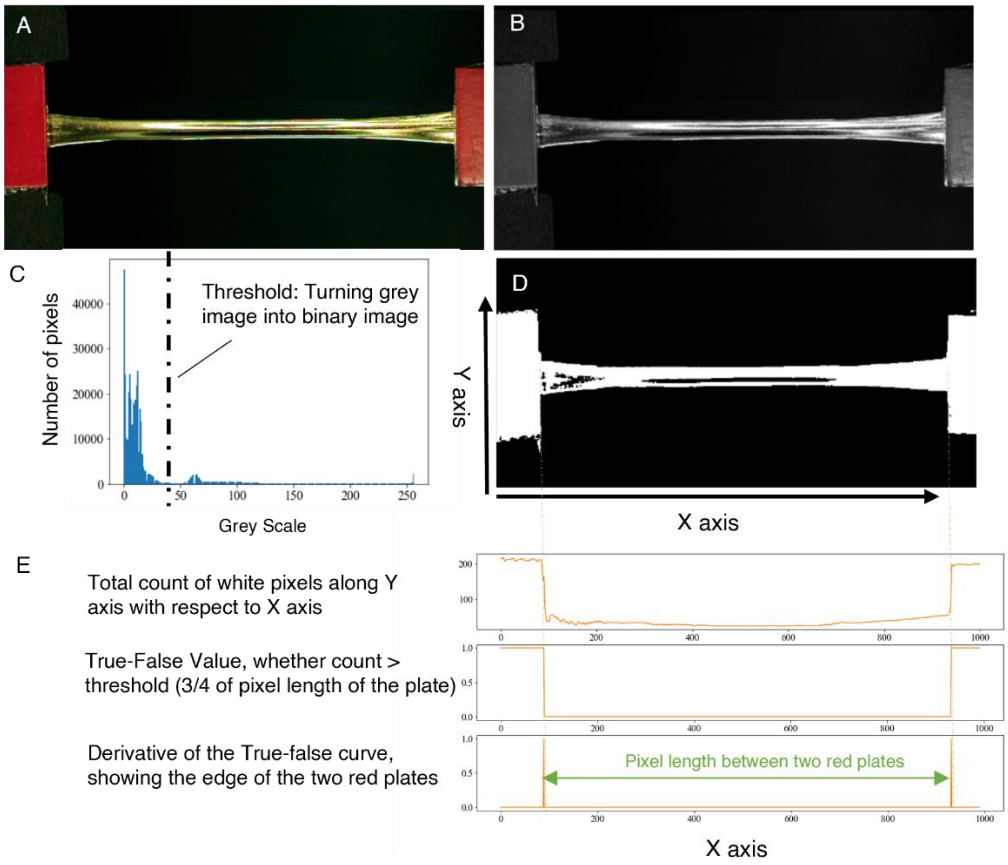

Figure 3.14: Method for measuring the actuation strain of the LCE film during the test. (**A**) Take a photo of the area of interests. (**B**) Convert the previously obtained RGB image into image stored with grey scale. (**C**) Get the histogram of pixel numbers with respect to grey scale which help to determine the threshold for binary image conversion. (**D**) Use the previous obtained threshold to convert the grey image into binary image. (**E**) Get the pixel length between the two ends. Actuation strain is then can be calculated from the pixel length change.

3.4.2 Isotonic tests and isometric tests with quasi-static stimulation conditions

With the constructed LCE-based motor unit, we then used 5 V voltage pulses with a sub-second pulse width (several hundred milliseconds) to stimulate the LCE-based motor unit. We first conducted isotonic tests as shown in Figure 3.15A, during which we measured the actuation strain of the LCE-based motor unit under different conditions. To measure the actuation strain versus time in isometric test (Figure 3.15A) with different voltage stimulation profiles, we characterize it by analyzing the videos taken from a high-speed camera (Edgertronic SC2); then, we used the self-defined algorithms (described in the previous section) to measure the actuation strain of LCE-based motor unit in each frame.

During the tests, we fixed the applied stress while stimulating the motor unit. Figure 3.15B shows that with an applied tensile stress of 1.4 MPa, the cyclic actuation strain of the motor unit with a peak value of 30% and a frequency of 0.25 Hz can be realized with the stimulating voltage pulses with a frequency (f) of 0.25 Hz and pulse width (t_w) of 0.5 s. We then repeated the tests with different applied stresses (0.25 MPa ~ 2.75 MPa) and pulse widths (t_w = 0.1 s ~ 0.5 s) of the stimulating voltage signals. Detailed result can be found in Figure 3.16. And the maximum actuation strain results are summarized in Figure 3.15C. Compared with the testing results of the uncoated LCE films (Figure 3.9), we conclude that the coated gold film shows a negligible effect on the actuation performance of the motor unit. Given the same pulse width, the maximum actuation strain decreases with increasing the applied stress. If we kept the applied stress as a

constant, the maximum actuation strain increases as the pulse width increases, due to the higher thermal energy input.

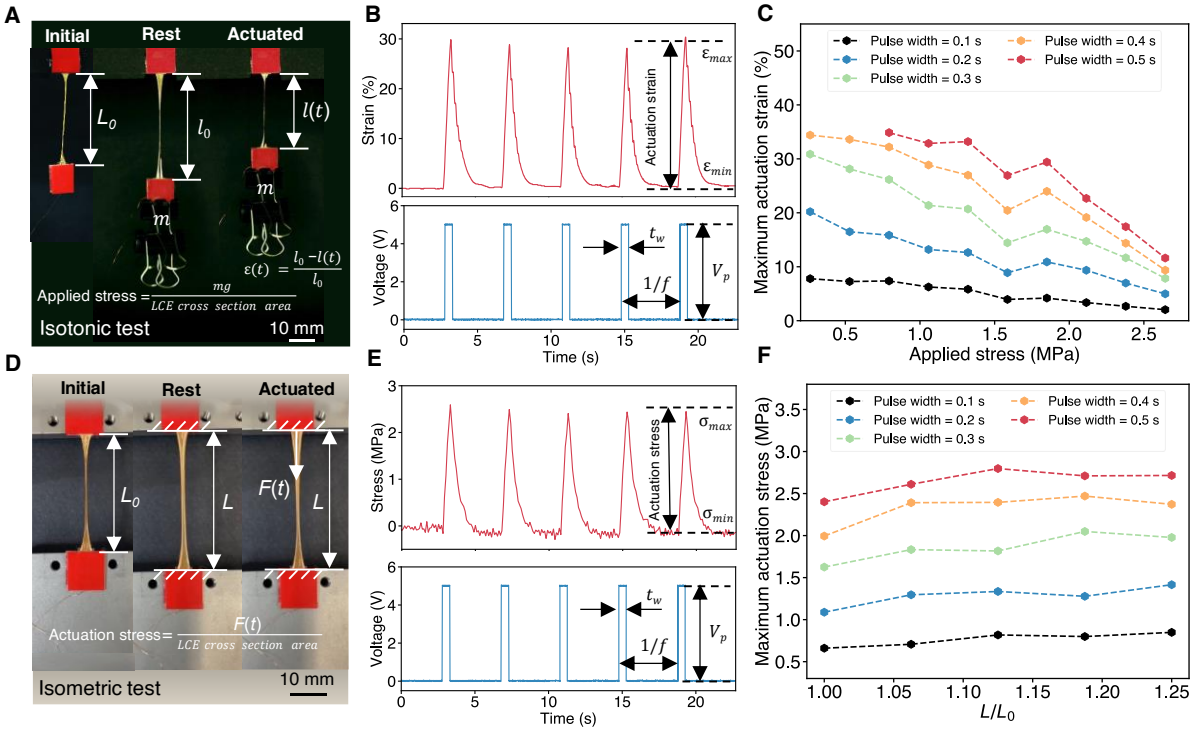

Figure 3.15: Quasi-static behavior of the LCE-based motor unit.
(**A**) Set up of an isotonic test: measurement of the actuation strain of the motor unit under voltage stimulations with a constant applied stress. (**B**) Actuation strain of the motor unit as a function of time when it is stimulated with periodical voltage pulses (V_p = 5 V, f = 0.25 Hz, t_w = 0.5 s) and a fixed applied stress of 1.4 MPa. (**C**) Summary of maximum actuation strain during isotonic tests with different applied stresses (0.25 MPa ~ 2.75 MPa) and different pulse width (t_w = 0.1 s ~ 0.5 s) of the stimulating voltage signals. (**D**) Set up of an isometric test: measurement of the actuation stress of the motor unit under voltage stimulations with a constant the stretch (L/L_0). (**E**) Actuation stress of the motor unit as a function as time when it is stimulated with periodical voltage pulses (V_p =5 V, f = 0.25 Hz, t_w = 0.5 s) and a fixed stretch ratio (L/L_0 = 1.25). (**F**) Summary of maximum actuation stress during isometric tests with different fixed stretches (1.0 ~ 1.25) and different pulse width (t_w = 0.1 s ~ 0.5 s) of the stimulating voltage signals.

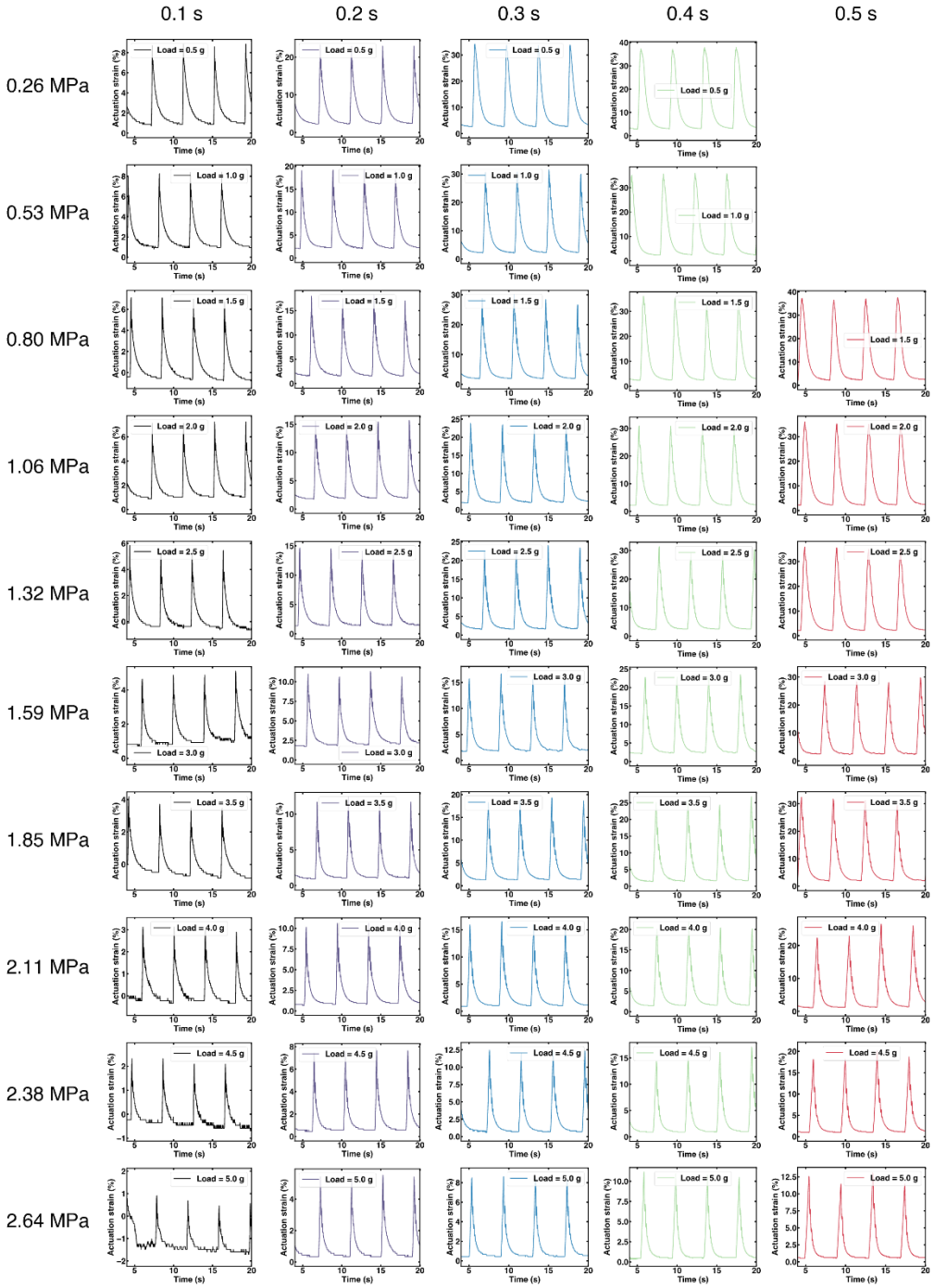

Figure 3.16: Actuation strain versus time of LCE-based motor unit during quasistatic tests. Different isotonic testing conditions of with the stimulation voltage at 0.25 Hz 5 V voltage pulses with pulse width from 0.1 s to 0.5 s were adopted and the applied stresses ranged from 0.26 MPa to 2.64 MPa. Actuation strains were obtained from the image processing of the video taken by Edgertronic high-speed camera.

Moreover, we also conducted isometric tests of the motor unit to measure its actuation stress as shown in Figure 3.15D. To measure the actuation stress vs time in isotonic test, we use the Instron Universal Testing System (Instron 5965) with a 10-N loading cell to read the actuation stress under different conditions. During the tests, we fixed the stretch (L/L_0) while stimulating the unit. Figure 3.15E shows that with the applied stimuli voltage (V_p = 5 V, f = 0.25 Hz, t_w = 0.5 s), the cyclic actuation stress generated by the motor unit has a peak value of 2.5 MPa at a constant stretch (L/L_0 = 1.25). We also systematically studied the actuation stress of the motor unit under different stretch states with changing the width of the voltage pulse as shown in Figure 3.17. The results are summarized in Figure 3.15F.

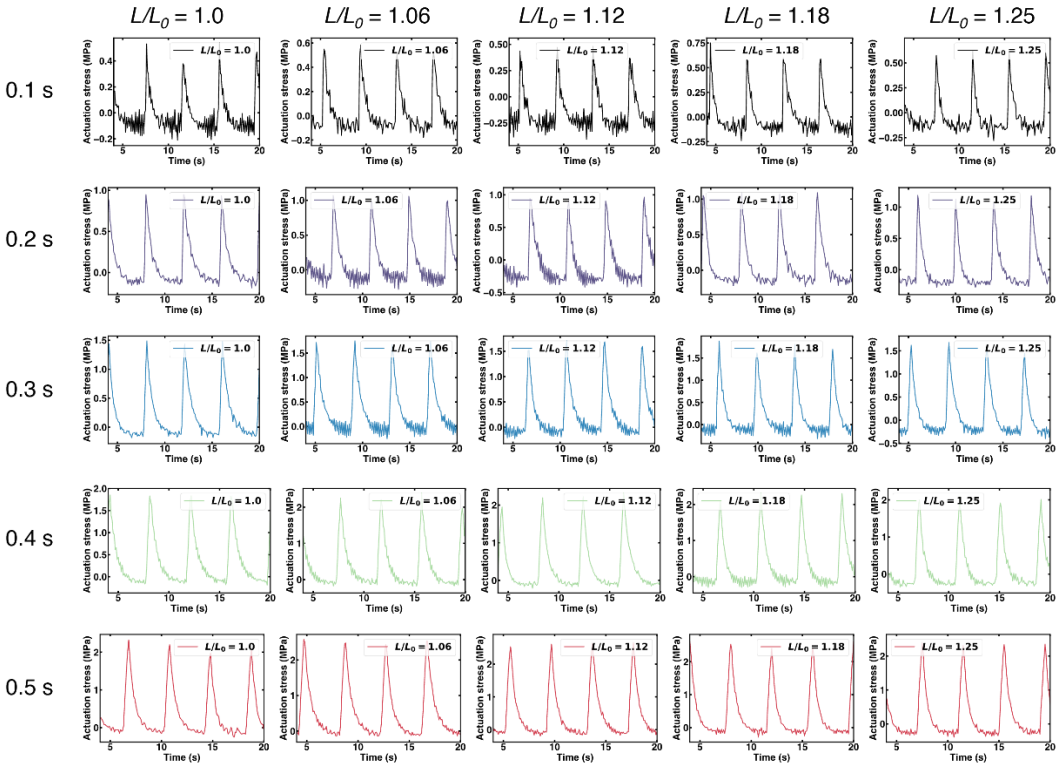

Figure 3.17: Actuation stress versus time of LCE-based motor unit obtained from isometric tests. The stimulations are 0.25 Hz 5 V voltage pulses with pulse width from 0.1 s to 0.5 s under different L/L_0 ratios.

Interestingly, for a given width of the voltage pulse, the maximum actuation stress is roughly a constant, independent of the stretched state, as shown in Figure 3.15F. Such features may enable higher controllability of the actuation stress produced by the LCE-based motor unit under different loading conditions. With a fixed stretch, the maximum actuation stress increases with the increase of the width of the voltage pulse from 0.1 s to 0.5 s, which saturates when the actuation stress approaches 3.0 MPa as shown in Figure 3.18, determined by the maximum actuation stress of the LCE material. This is consistent with the results in Figure 3.9E in which the maximum actuation stress reaches its maximum value when the temperature increases to 170 °C.

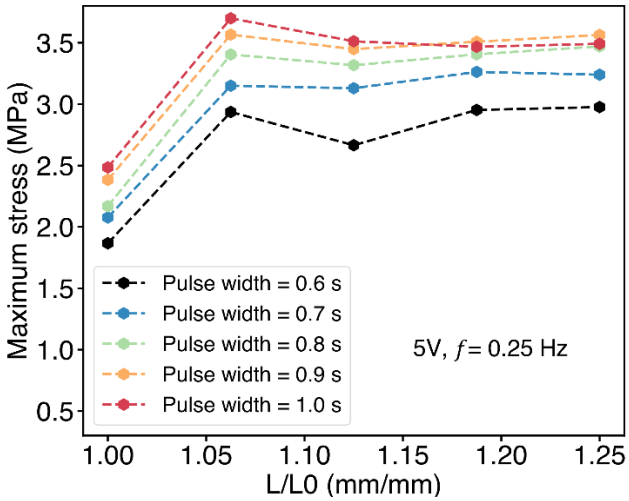

Figure 3.18: Maximum actuation stress during isometric tests with different stretches *(L/L_0)*. During the tests, the LCE-based motor unit is stimulated with 5 V pulses (0.25 Hz) of pulse width from 0.6 s to 1.0s. The peak value of the actuation stress changes little when the pulse width was increased to more than 0.8 s.

3.5 Dynamic behaviors of the LCE-based motor unit

For conventional LCE-based actuators, the time scales for the temperature change inside the material (determined by its thermal inertia) are often much larger than the time scales determined by their mass inertia, and therefore, their mass inertia has negligible influence on their actuation performance. However, in our design, due to the small thickness of the LCE film, the time for the temperature change inside the material can be shorter than the time set by its mass inertia, and thus the mass inertia of the motor unit with a hanging weight greatly influences its dynamics. It is noted that the influence of the mass inertia on the dynamics of animal muscles has been reported previously [80].

3.5.1 Representative dynamic behaviors

Representative dynamic behaviors of the LCE-based motor unit under the stimulation of periodic voltage pulses are shown in in Figure 3.19. For example, when the motor unit was subjected to an applied stress of 1.7 MPa, it was able to generate an actuation strain over 45% within 0.1 s, and a typical maximal velocity during the contraction or recovery can reach 0.3 m/s with a peak acceleration of around 10 m/s^2. In the experiment, we applied a voltage of 30 V with a pulse width of 5 ms and a frequency of 2 Hz onto the actuator. The pulse width is much shorter than the time scale determined by the mass inertia of the motor unit (100 ~ 200 ms). With the periodic voltage stimulation at 2 Hz, the motor unit oscillated cyclically at a higher frequency of 6 Hz, which was mainly determined by its resonant frequency (verified through Fourier analysis in the next section). Such frequency mismatch is a reminiscent of the dynamic behavior of

asynchronous muscle widely existing in insect flight muscles (IFMs). Though the working mechanisms are not identical [81], our work may provide an insight for understanding the dynamic behaviors of asynchronous muscles.

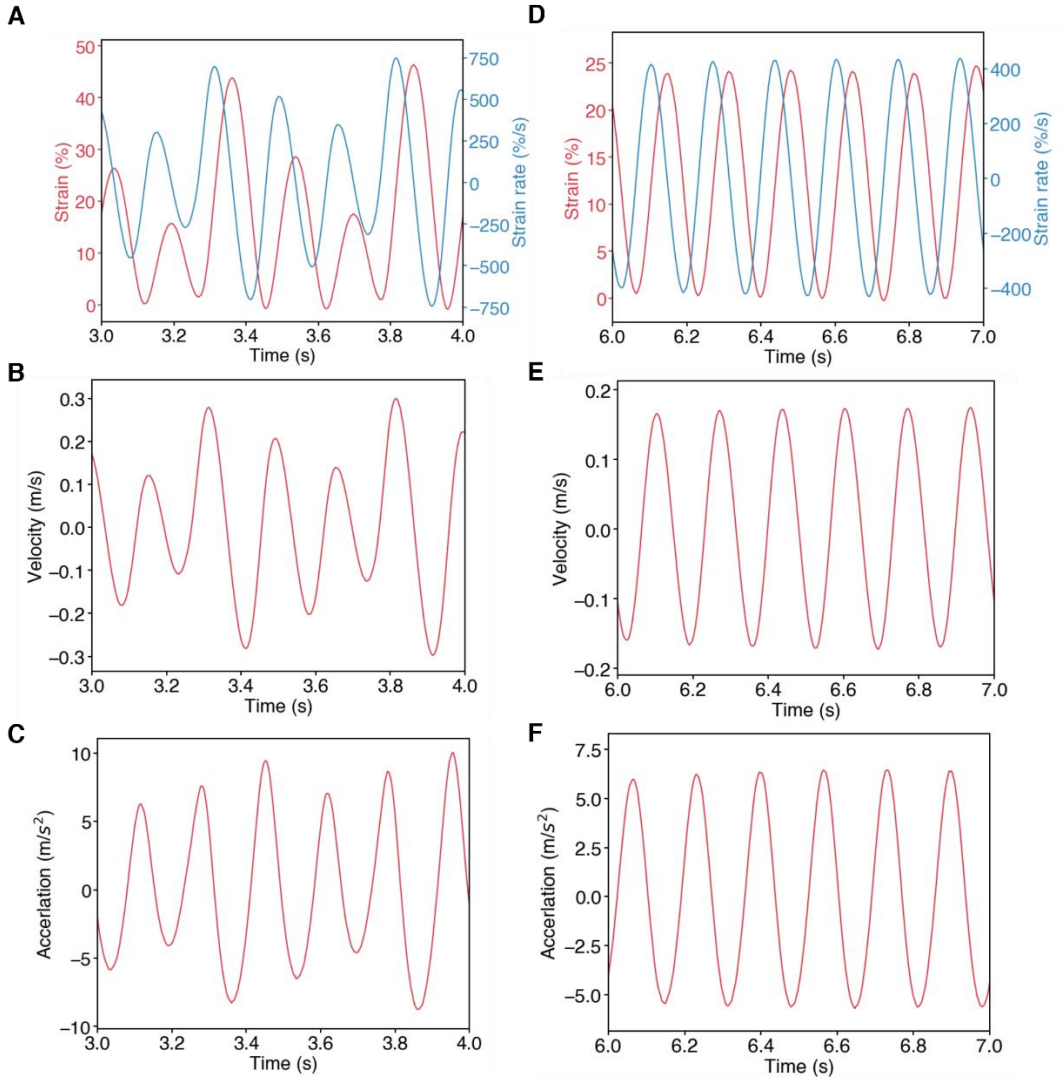

Figure 3.19: Typical velocity and acceleration versus time of the LCE-based motor unit during its dynamic tests.

(**A**) Actuation strain and the associated strain rate of LCE motor unit when it was stimulated with 30 V pulses (2 Hz frequency, 5 ms pulse width). (**B**)-(**C**) Velocity and acceleration of the hanging weight with the stimulation voltage of 30 V pulses (2 Hz frequency, 5 ms pulse width). (**D**) Actuation strain and the associated strain rate of LCE-based motor unit when it was stimulated with 30 V pulses (6 Hz frequency, 1.7 ms pulse width). (**E**)-(**F**) Velocity and acceleration of the hanging weight with the stimulation voltage of 30 V pulses (6 Hz frequency 1.7 ms pulse width).

3.5.2 Fourier analysis of the time-varying actuation strain (power density spectrum)

We collected the time-varying actuation strain of the motor unit with an applied stress of 1.5 MPa under cyclic 30 V voltage pulses as shown in Figure 3.20. We controlled the input electrical power as a constant of 320 mW while increasing the frequency from 2 Hz to 10 Hz. To avoid the fracture of the motor unit, the electrical power was 180 mW when the frequency of the voltage pulse is 1 Hz.

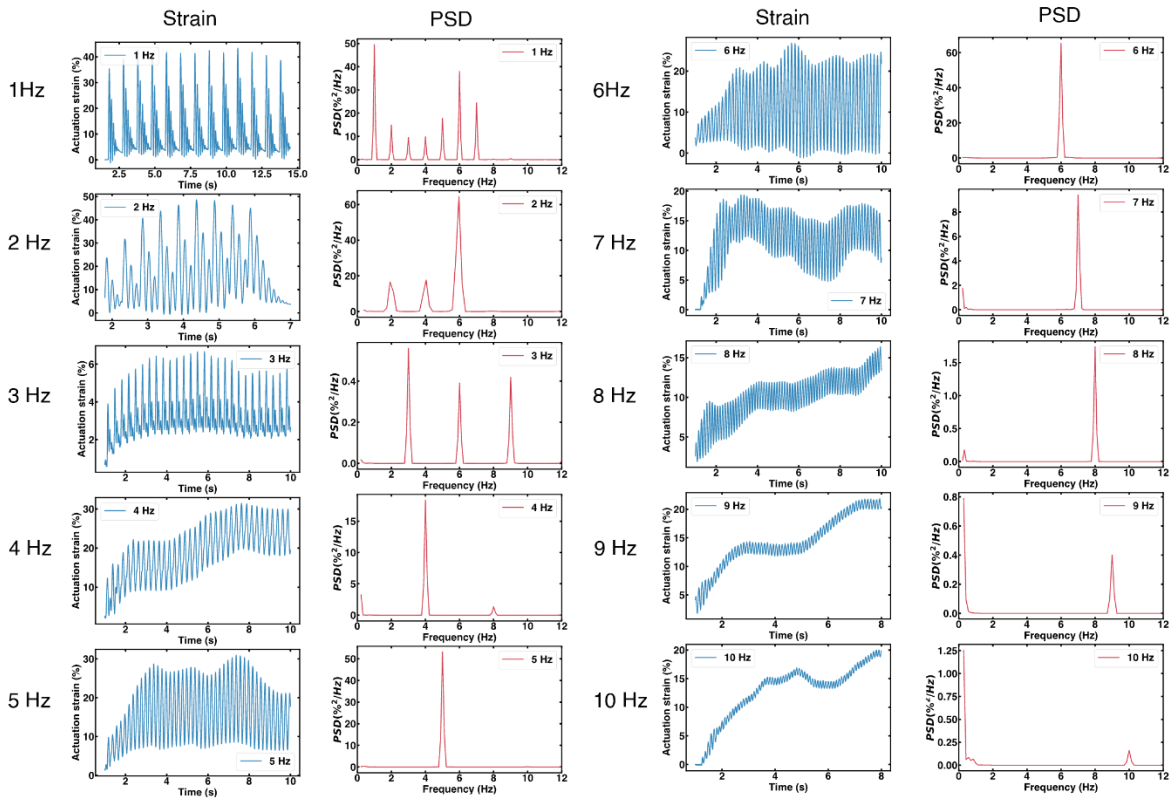

Figure 3.20: Fourier analysis of actuation strain versus time during the dynamic isotonic tests. The applied stress was 1.5 MPa, and the LCE motor unit was stimulated by a voltage of 30 V pulses at different frequencies. The input electrical power is controlled as a constant of 320 mW during the tests except for 1 Hz (180 mW). It can be concluded from the power spectrum density results that the dynamic oscillation is mainly determined by the resonant frequency of the mechanical system.

We then analyze the data of time-varying actuation strain by performing the Fourier transformation. The power spectrum density (PSD) of the actuation strain is also given in fig. S16. For the stimulation frequency between 1 Hz and 6 Hz, we can see several peaks in the PSD plot, some of which are associated with the resonance of the system. When the stimulation frequency is above 6 Hz, the stimulation frequency determines the oscillation dynamics of the LCE film. The actuation strain amplitude keeps decreasing as the stimulation frequency increasing over 6 Hz, indicating the possibility of adopting Pulse Width Modulation (PWM) and rate coding control strategies for the LCE motor unit.

3.5.3 Large strain rate observed in the dynamic behaviors

To quantitatively understand the dynamic performance of the motor unit, we first used 1 Hz 30 V voltage pulses with different pulse widths (1 ms ~ 5 ms) to perform the isotonic tests of the LCE-based motor unit subjected to different applied stresses (0.75 MPa ~ 1.75 MPa) as shown in Figure 3.21 with detailed strain versus time of the motor unit. With a longer pulse width, the motor unit generated a larger actuation strain. We further obtain the result of strain rate (Figure 3.21B) by taking the first derivative of the actuation strain (Figure 3.21A). It is noted that moving average algorithm is used to smooth the actuation strain results before taking derivatives.

Under a specific pulse width (i.e., t_w = 5 ms), the maximum strain rate of the LCE-based motor unit decreases with increasing the applied stress. Notably, the highest strain rate during either actuation or recovery is about 600 %/s (when t_w = 5 ms, applied stress = 0.75 MPa). As a comparison, the typical strain rate of human muscles is about 50 %/s [63, 82].

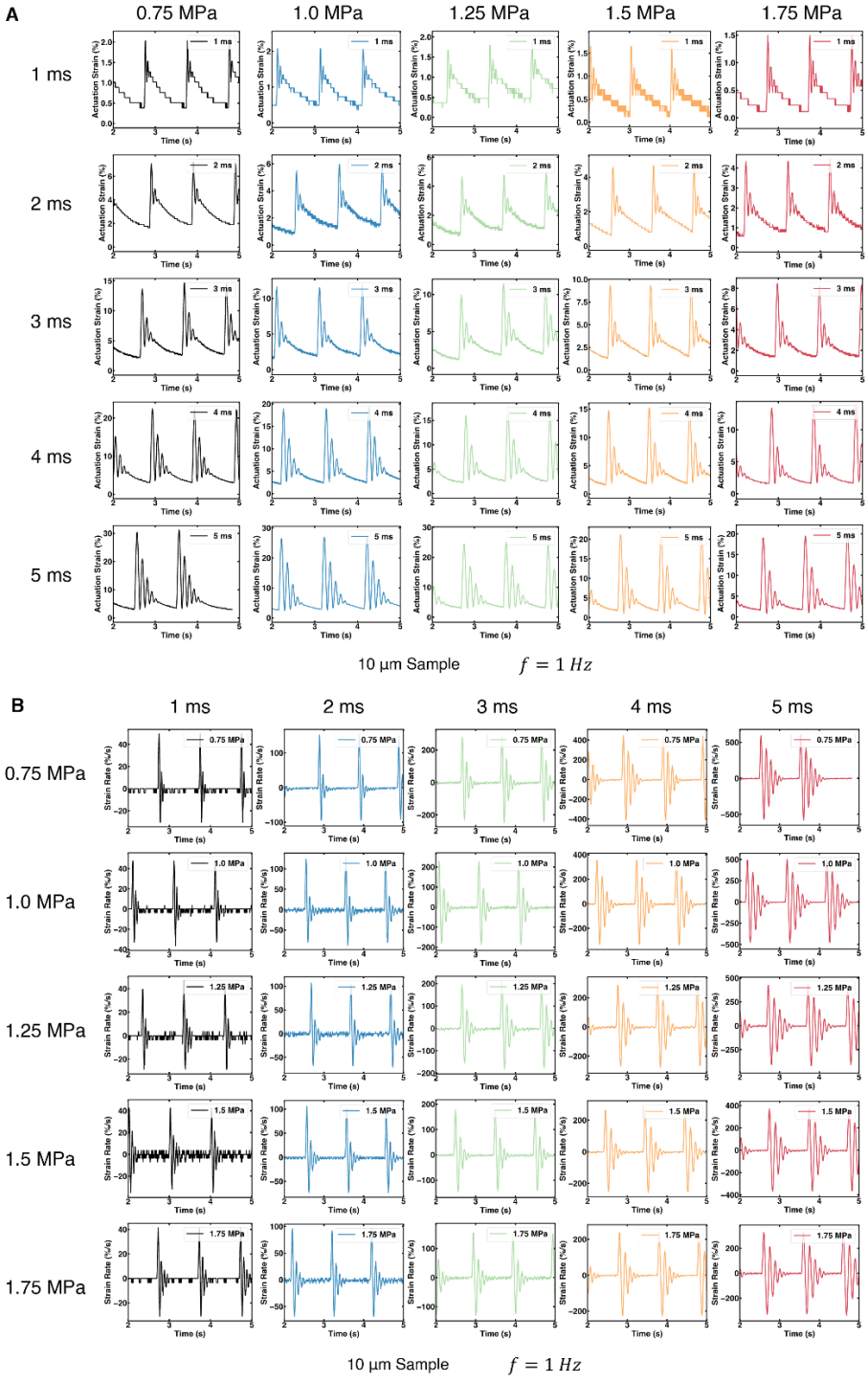

Figure 3.21: Actuation strain and strain rate versus time of LCE-based motor unit when it is stimulated by a cyclically applied voltage pulse of 30 V at 1 Hz frequency.
(**A**) Actuation strain vs time when varying the pulse width from 1 ms to 5 ms and the applied stress from 0.75 MPa to 1.75 MPa. (B) Actuation strain rate vs time when varying the pulse width from 1 ms to 5 ms and the applied stress from 0.75 MPa to 1.75 MPa.

3.5.4 Isometric test of LCE-based motor unit with 30 V pulses

We also characterized the actuation stress of the motor unit in an isometric condition with the voltage pulses of 30 V (pulse width of a few milliseconds). The actuation stress measurements during isometric tests under these periodic short pulses (V_p = 30 V, t_w = 1~5 ms, f = 0.25 Hz) exhibits a similar behavior to the quasi-static cases but with a lower value not exceeding 1.0 MPa (Figure 3.22) which can be explained by lower electrical power input. For a voltage pulse of 30V (0.25 Hz) with pulse width of 5 ms, the electrical power input is no more than 150 mW. While for the voltage pulse we used in generating quasistatic behaviors such as a voltage pulse of 5 V (0.25 Hz) with a pulse width of 500 ms, the electrical power is as high as 400 mW. Meanwhile, we can further compare the ratio of cooling time over period of one stimulation cycle (4 s in this case). For quasistatic case, this ratio is 0.875 when pulse width is 500 ms while for dynamic stimulation case this ratio increases to 0.999 when the pulse width is 5 ms. In other words, we allow more cooling time for this sharp and concentrated voltage pulses (30 V for several milliseconds) which leads to a more efficient cooling while sacrificing a little on the actuation stress.

We obtained the results by fixing the LCE motor unit at different stretches (L/L_0 = 1.0 ~ 1.25) while stimulating it by 0.25 Hz 30 V pulses with pulse width from 2 ms to 5 ms (Figure 3.22A-D). The actuation stress of the motor unit increases with increasing the pulse width. However, as we increased the stretch, the passive stress of the LCE increased, but the active actuation stress induced by the stimulation does not significantly change, which can be seen in Figure 3.22E.

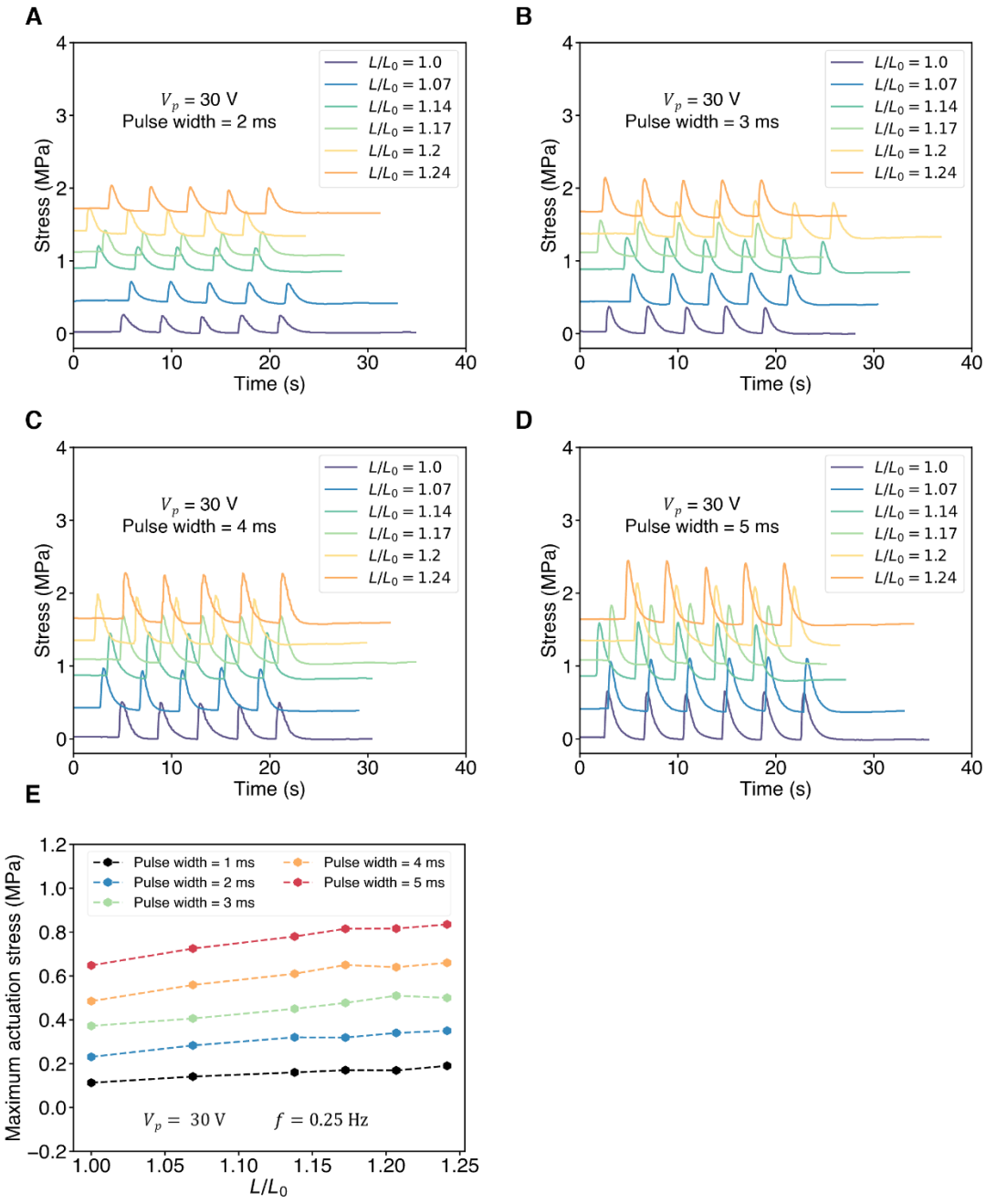

Figure 3.22: Actuation stress profile of the LCE actuator during isometric tests with different stimulation condition and stretches (L/L_0)
(**A**) 30 V, 0.25 Hz, 2 ms; (**B**) 30 V, 0.25 Hz, 3ms; (**C**) 30 V, 0.25 Hz, 4 ms; (**D**) 30 V, 0.25 Hz, 5 ms. (**E**) Maximum actuation stress vs pre-stretches for several different pulse widths.

3.5.5 Systematic study of the dynamic behaviors

To study the output power density of the LCE-based motor unit under different stimulation conditions, we then performed a series of isotonic tests by varying the frequency of the voltage pulse from 2 Hz to 10 Hz while controlling the input electrical power (energy provided by the voltage pulses per second, see Figure 3.1B) as a constant (250 mW). The frequency of applying the voltage pulses ranges from 2 Hz to 10 Hz and the applied stress ranges from 0.75 MPa to 1.75 MPa. During the tests, the input electrical power was fixed as a constant of 250 mW. We obtained the actuation strain from the image processing of the video taken by Edgertronic high-speed camera. The selected results under different conditions are plotted in a matrix form as shown in Figure 3.23. For the electrical signal with the same voltage and pulse width, the actuation strain maintains its high level and starts to decrease as the stimulation frequency increases over 6 Hz, as shown by the Bode Plot in Figure 3.24.

We next estimated the output of the mechanical power density of the motor unit by computing the work done during the first contraction cycle immediately after the voltage pulse was applied. For example, as shown in Figure 3.19A, the power density is estimated to be around 900 W/kg in this case. The number is calculated by dividing the output work from the LCE in one second by its own weight (1.2 mg), during which the LCE film lifts a weight of 3.1 g (applied stress of 1.7 MPa) by a height of 16 mm (actuation strain of 45%) with a stimulation of 2 Hz. Such power density is close to that of the flight muscle of some insects [73].

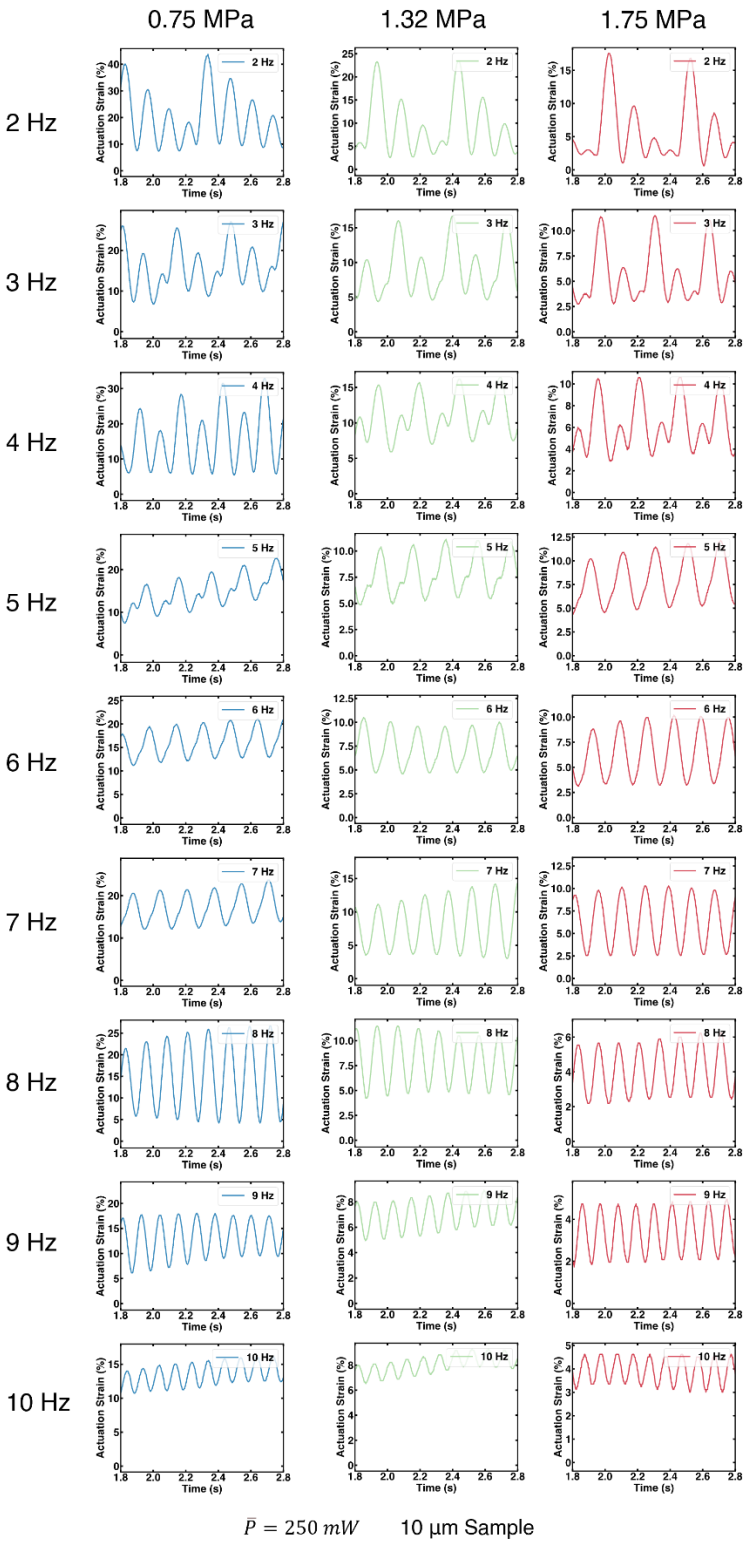

Figure 3.23: Actuation strain vs time of the LCE-based motor unit for different isotonic test conditions with the stimulation voltage at 30 V.

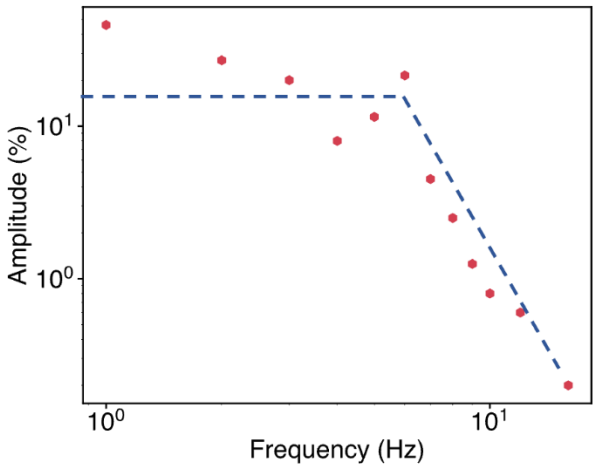

Figure 3.24: Bode plot of the actuation strain versus frequency (log-log) of the LCE motor unit during isotonic test under 30 V voltage stimulation with the frequency varying from 1 Hz to 16 Hz. The blue dashed line indicates the cutoff frequency at around 6 Hz, which is regarded as bandwidth of the LCE motor unit.

Based on Figure 3.23, we then summarized the actuation strain with different stimulation frequencies and plotted them in Figure 3.25. from. This result will be used to calculate the output mechanical power density of the LCE-based motor unit.

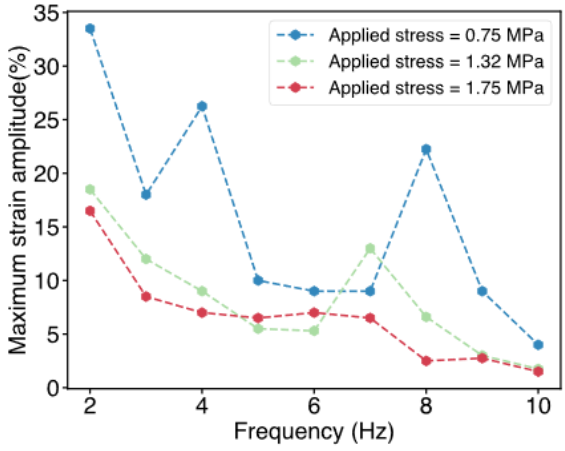

Figure 3.25: Difference between the largest and the smallest actuation strain of the LCE motor unit for different testing conditions. We calculated the results from Figure 3.23 and denoted it with "maximum strain amplitude" in the vertical axis. We use this result to calculate the power density which will be discussed later.

3.5.6 Output power density of LCE-based motor unit in isotonic tests

Since this oscillatory motor unit can be regarded as a mass-spring damping system, the natural frequency of the system can then be estimated by the following equation:

$$\omega_n = \sqrt{\frac{k}{m}} \quad , \quad (3.1)$$

where ω_n is the nature frequency of the LCE-based motor unit with a hanging weight, k is the spring constant of the LCE-based motor unit and m is the mass of the hanging weight.

To maintain the applied stress unchanged, we changed the mass of the hanging weight for the motor units of different thicknesses accordingly:

$$m = \frac{\sigma_{applied} W_{LCE} \delta_{LCE}}{g} , \quad (3.2)$$

where $\sigma_{applied}$ is the applied stress (namely, 1.7 MPa), W_{LCE} is the width of the LCE film, δ_{LCE} is the thickness of the LCE and g is the gravitational acceleration. We can further estimate the spring constant of the motor unit:

$$k = \frac{E W_{LCE} \delta_{LCE}}{L_{LCE}} , \quad (3.3)$$

where E is the Young's Modulus of LCE and L_{LCE} is the length of the LCE film. We then combine equation (3.1), (3.2) and (3.3) to obtain the natural frequency as:

$$\omega_n = \sqrt{\frac{E}{\sigma_{applied}} \frac{g}{L_{LCE}}} \quad , \quad (3.4)$$

which is independent of the thickness of the LCE. After plugging the numbers, $E \approx 6.6$ MPa (estimated based on Figure 3.9), $\sigma_{applied}$ = 1.7 MPa, g = 9.8 m/s^2, and L_{LCE} = 40 mm, we have $\omega_n \approx 31$ rad/s or $f_n \approx 4.9$ Hz. To verify the analysis, we then collected the actuation strain of the

LCE-based motor unit under the applied stress of 1.7 MPa and with 30 V voltage stimulations as shown in Figure 3.26. We obtained the actuation strain from the image processing of the video taken by Edgertronic high-speed camera.

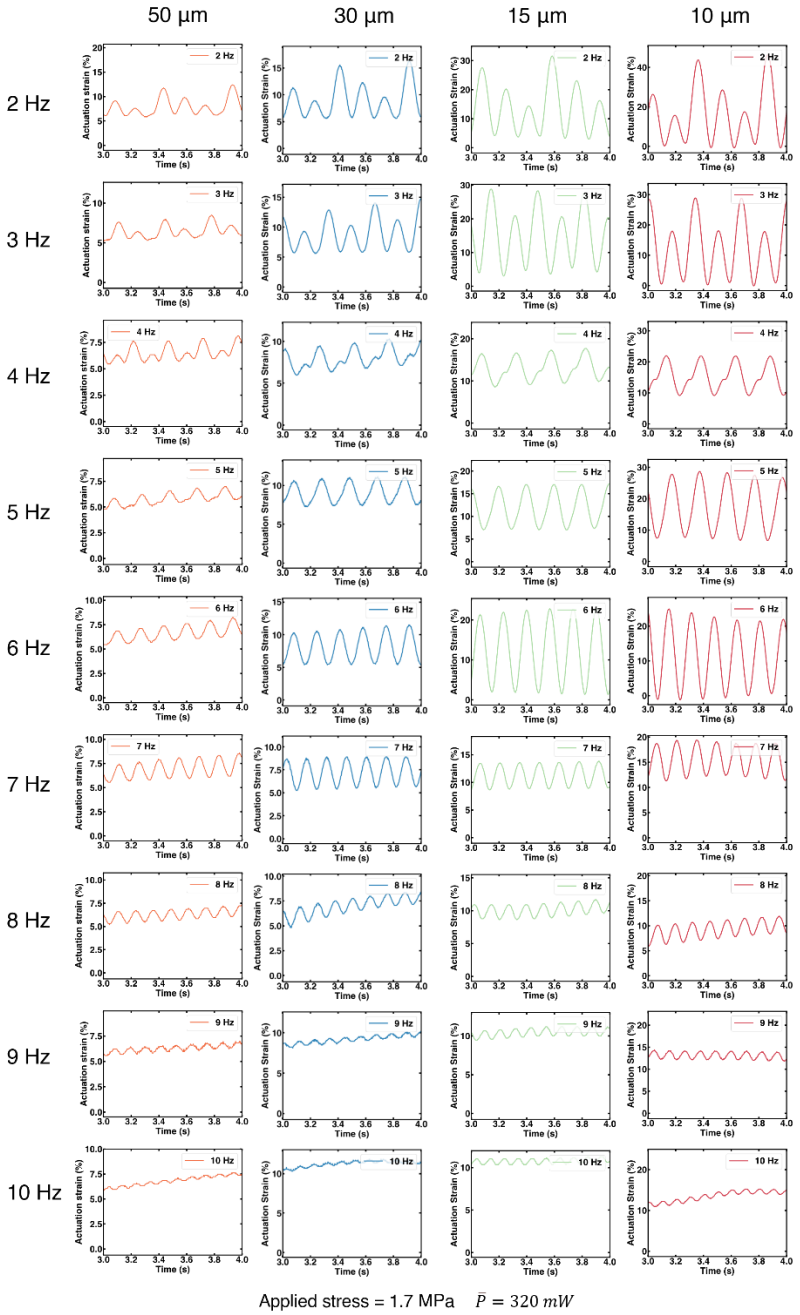

Figure 3.26: Actuation strain versus time from different isotonic test conditions of the LCE-based motor unit with different LCE thickness and a constant applied stress of 1.7 MPa.

During the experiment, we controlled the input electrical power as a constant of 320 mW while increasing the frequency from 2 Hz to 10 Hz. The LCE motor units have different thicknesses from 10 μm to 50 μm. The results can be further plotted as output power density versus frequency as shown in Figure 3.24. The power density was calculated using the method described in the previous section. For the LCE film with the thickness of 10 μm, its maximum power density is around 1360 W/kg when the stimulation frequency is 6 Hz, which is a remarkable high value and outperforms most of biological muscles [63].

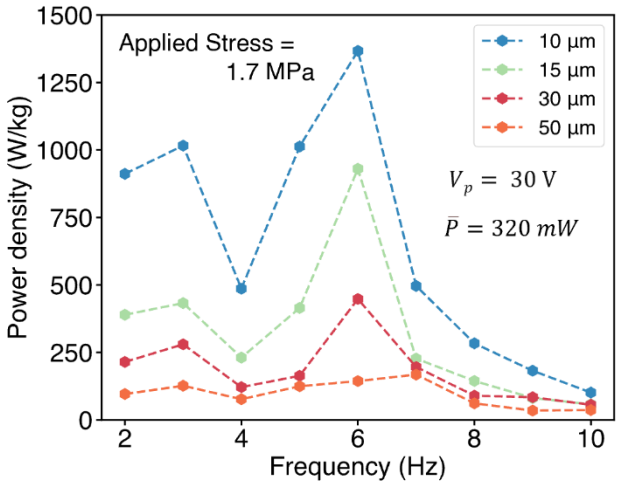

Figure 3.27: The peak of the power density always occurs at 6 Hz with different LCE thicknesses and a constant applied stress (1.7 MPa) during isotonic tests.

More importantly, the applied stress was controlled as 1.7 MPa for all the tests shown in Figure 3.26, following the analysis we have done at the beginning of this section, we shall have a consistent natural frequency (~4.9 Hz) regardless of the thickness of the LCE. The experimental results from Figure 3.27 do support our analysis, in which the maximum value of power density appears at 6 Hz regardless of the thickness of the LCE.

3.5.7 Comprehensive performance of the LCE-based motor unit outperforming real muscle

Real biological muscle is known as soft actuator with extraordinary performance in all the main metrics of an actuator such as actuation stress, actuation strain, power density, work density, bandwidth and so on. Such comprehensive performance of the biological muscles makes most of the engineering actuating materials hard to compete with. While with the LCE-based motor unit, we developed, we show a comprehensive performance which is close to or even outperform the biological muscles.

We have already shown the large actuation stress in Figure 3.16 with a maximum value of over 3.0 MPa. We have also demonstrated large actuation strain of over 50% as shown in Figure 3.28, in which the LCE-based motor unit can lift 2.6 g weight (~2100 times of its own weight) within 0.083 s and reach a large actuation strain of over 50%.

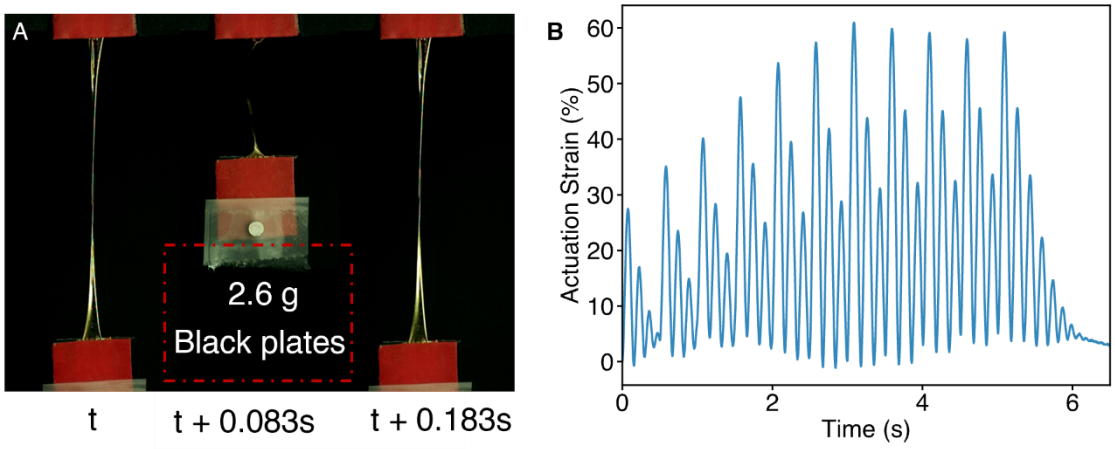

Figure 3.28: LCE-based motor unit shows a large actuation strain (40% ~ 60%) during isotonic test with applied stress of 1.5 MPa.
(**A**) The LCE-based motor unit lift weight within 0.083 s. Black plate is used as a mechanical load. (**B**) Experimental data of actuation strain obtained from this test. The magnitude of the stimulation voltage pulse is 30 V, its frequency is 2 Hz and the pulse width is 6 ms.

Based on the actuation strain results from Figure 3.26, we can further obtain the work density of the LCE-based motor unit under different loading conditions as shown in Figure 3.29: The work density increases as the pulse width increases, due to the larger energy input. It is noted that the maximum work density with the help of resonance can be as high as 455 J/kg.

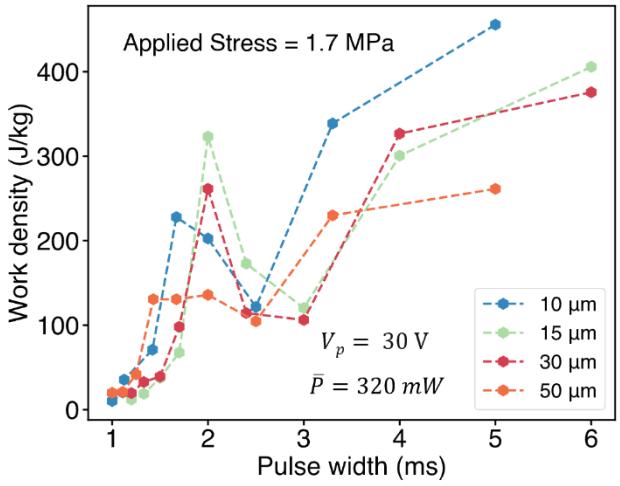

Figure 3.29: For the LCE film with the thickness of 10 µm, its work density can reach 455 J/kg under applied stress of 1.7 MPa.

To further show the comprehensive performance of the LCE-based motor unit, we summarize the main results of the dynamic behaviors in Figure 3.30. We plotted the maximum actuation strain of the motor unit versus the pulse width in Figure 3.30B and then plotted the peak strain rate versus the applied stress in Figure 3.30C. Based on Figure 3.23 and Figure 3.25 (actuation strain versus time), we plotted the output mechanical power density of the motor unit for different voltage pulse frequency under different applied stresses (0.75 MPa ~ 1.75 MPa) as shown in Figure 3.30D. The output power density becomes larger as the frequency of the simulation voltage becomes closer to the resonance frequency of the mechanical system. The appearance of the peak of the output power

density shifts from 7 Hz to 8 Hz as applied stress decreases from 1.75 MPa to 0.75 MPa. Meanwhile, as shown in Figure 3.30E, with fixing all the other controlling parameters, the mechanical power density increases dramatically as the thickness of the LCE decreases from 50 μm to 10 μm.

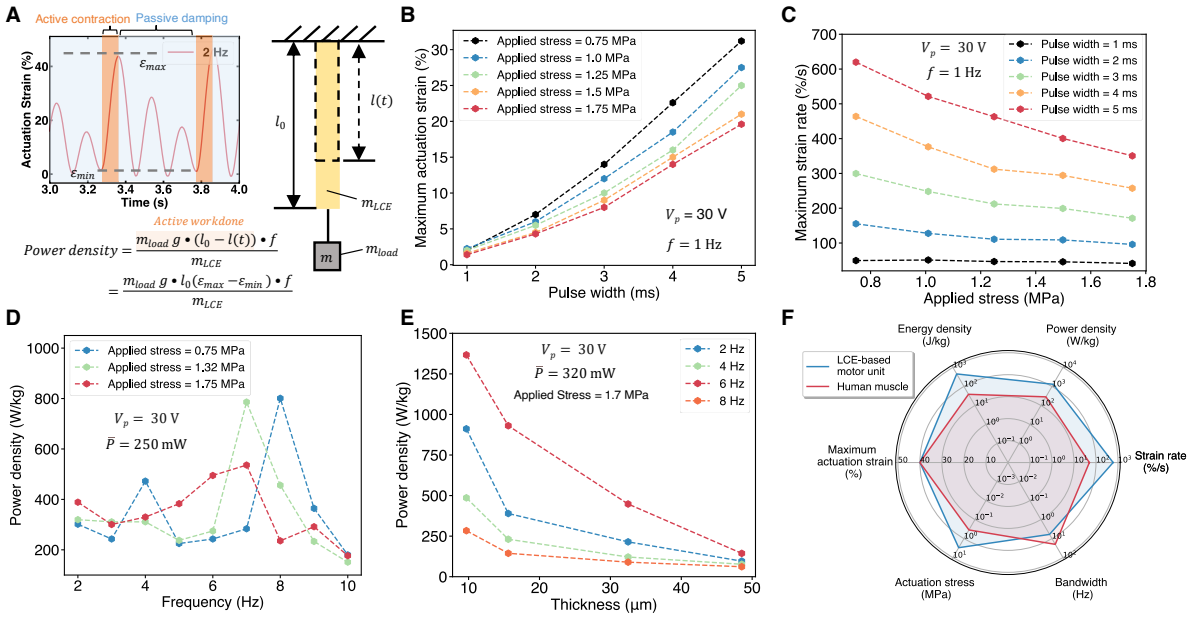

Figure 3.30: Dynamic behaviors of the LCE-based motor unit.

(**A**) Representative dynamic behavior of the LCE-based motor unit under the stimulation of periodic voltage pulses (V_p = 30 V, f = 2 Hz, t_w= 5 ms), when it is subjected to an applied stress of 1.7 MPa. (**B**) Maximum actuation strain vs voltage pulse width (t_w = 1 ms ~ 5 ms, V_p = 30 V, f = 1 Hz) under different applied stresses (0.75 MPa ~ 1.75 MPa). (**C**) Maximum strain rate vs different applied stress (0.75 MPa ~ 1.75 MPa) by taking derivative of previous actuation strain vs time results. (**D**) The peak of power density shifts with varying the applied stress (0.75 MPa ~ 1.75 MPa) during isotonic tests. (**E**) Increase of power density with decreasing the LCE thickness. (**F**) Radar plot showing the similar performance between the LCE motor unit and the human muscle in terms of actuation strain, actuation stress, bandwidth, strain rate, power density and energy density.

Finally, we summarized all the measured performance metrics and plotted the highest value in a radar plot (Figure 3.30F). As shown in the radar plot, LCE-based motor unit has the maximum

actuation stress of 3 MPa, the maximum actuation strain over 50%, the maximum energy density of 455 J/kg, the maximum power density of 1360 W/kg, the maximum strain rate of 750 %/s, and the bandwidth of 6 Hz. Noticeably, the overall performance of the LCE-based motor unit is comparable to or better than that of human muscles.

3.6 Actuation stress control of the motor unit

Force control (or stress control) in robotics is known to be more complex than position control (or strain control), but force control is critical in many applications, especially in grasping and manipulation [83]. Herein, we show that we can control the actuation stress produced by the LCE-based motor unit using two different control strategies: rate coding and pulse width modulation (PWM). For animals, the magnitude of the contraction force of biological muscle can be controlled through varying the firing rate of the motor neuron, known as rate coding [84]. As the firing rate increases, the output muscle force changes from single twitch to fused tetanus [85]. We used the motor unit to mimic such behavior, as shown in Figure 3.31A, during the isometric tests. When the motor unit is stimulated by voltage pulses with a frequency of 0.25 Hz, the produced actuation stress shows a typical shape of single twitches. After increasing the stimulation frequency to 100 Hz, all the twitches fuse together showing a smooth summation of twitches or tetanus contraction in biological muscles. The actuation stress remained at a constant magnitude (0.6 MPa) in the test. In Figure 3.31B, we show that by increasing the frequency of the stimulating voltage from 10 Hz to 50 Hz while keeping the pulse width as a constant, the actuation stress increased from 0.4 MPa to above 1.5 MPa, emulating the rate coding process in animal muscles.

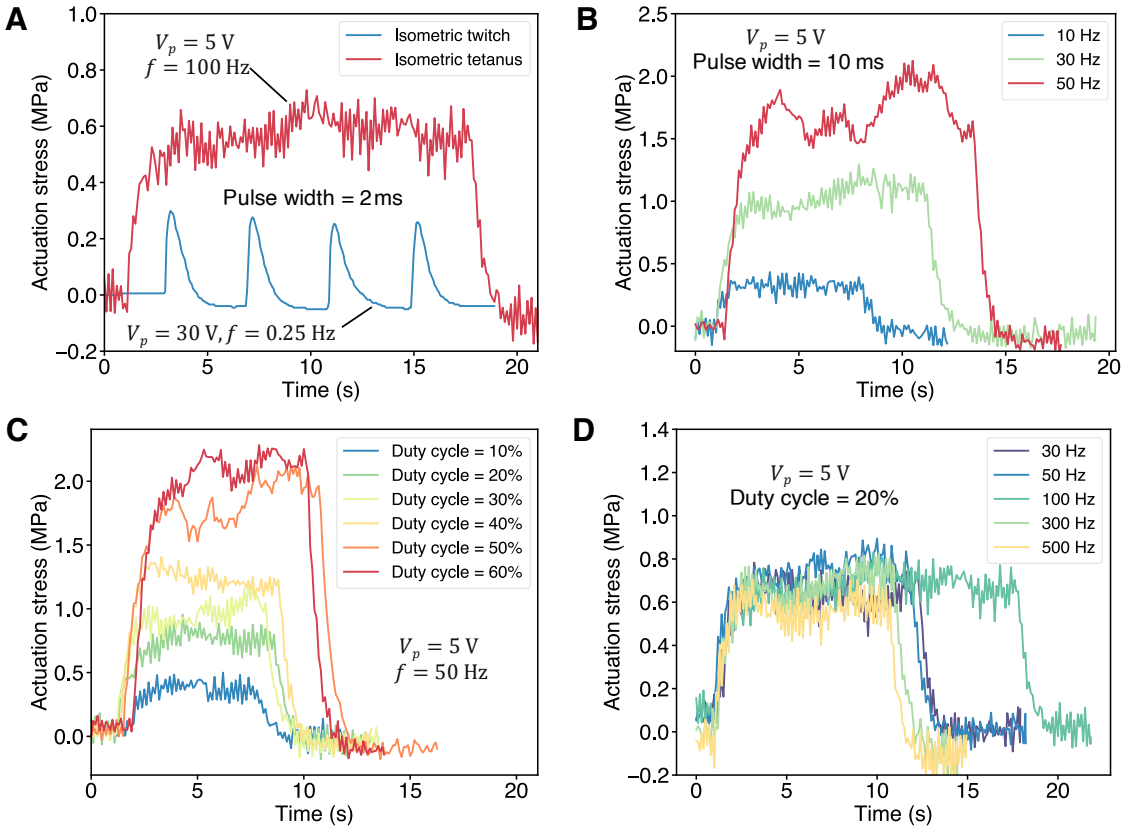

Figure 3.31: Control of the actuation stress of the motor unit in isometric tests. (**A**) The actuation stress changes from single twitch to fused tetanus as the stimulation frequency increases from 0.25 Hz to 100 Hz. (**B**) We use the LCE motor unit to emulate the rate coding process in animal muscle. Actuation stress is tuned through increasing the voltage frequency from 10 Hz to 50 Hz while maintaining the pulse width as a constant. (**C**) Actuation stress control through changing the duty cycle (10% ~ 60%) based on the PWM control strategy. (**D**) Actuation stress is independent of voltage pulse frequency with a fixed duty cycle in PWM control strategy.

In real electronic robotic systems, pulse width modulation (PWM) control strategy is widely adopted, which can be more easily achieved by most microcontrollers. Herein, we show that the actuation stress of the LCE-based motor unit can also be controlled through the PWM strategy. In Figure 3.31C, the actuation stress level is controlled through setting different values of the duty cycle. With a fixed voltage (5 V) and stimulation frequency (50 Hz) of the applied voltage, the actuation stress increased from below 0.5 MPa (duty cycle = 10%) to above 2.0 MPa (duty cycle

= 60%). In Figure 3.31D, we show that once the PWM controller is applied, the actuation stress is mainly determined by the duty cycle instead of the stimulation frequency. However, it is noted that to reach a stable stress level, the stimulation frequency needs to be higher than 10 Hz as shown in Figure 3.32.

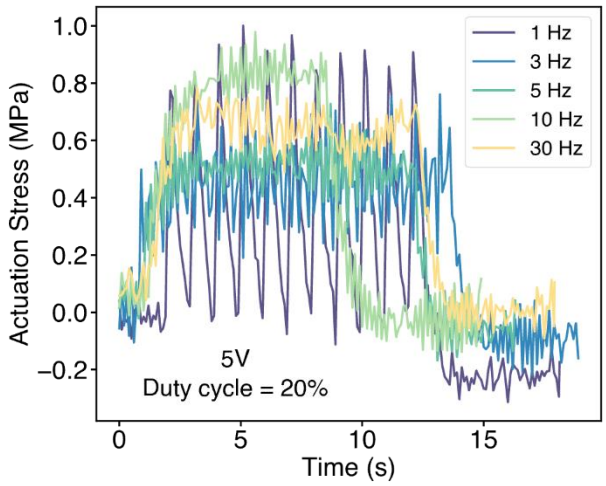

Figure 3.32: The sharp peaks of the actuation stress merge to form a stable plateau once the stimulation frequency is larger than 10 Hz in isometric tests.
The actuation stress is tunable through pulse width modulation (PWM). During the test, the length of the LCE film is fixed at its original length (L_0), and the stimulation voltage is 5 V pulses with a fixed duty cycle of 20%.

3.7 Electro-thermo-mechanical model of the LCE-based motor unit

To better understand the performance of the LCE-based motor unit, we developed an electro-thermo-mechanical model to predict the system responses under the stimulation of voltage pulses. Due to the small thickness of the LCE film, its Biot number is much smaller than 1 (approximately 0.0002), implying that the temperature field inside the material is nearly homogenous. Therefore, the temperature of the film can be easily computed, assuming Joule heating is entirely caused by the coated gold film, which can be obtained from Joule's law. By connecting the electrical heating with the actuation characteristics of the LCE, we can then build up the electro-thermo-mechanical model of the LCE-based motor unit.

3.7.1 Solving the temperature profile with given voltage pulses

The power provided by Joule heating can be calculated by:

$$P_{in}(t) = \frac{V_p(t)^2}{R} \quad (3.5)$$

where P_{in} is the electrical power generated by the voltage pulses applied to the LCE-based motor unit, $V_p(t)$ is the profile of the input voltage, and R is the electrical resistance of the gold film. The Biot number for this LCE-based motor unit can be given by:

$$Bi = \frac{\delta_{LCE}/K_{LCE}}{1/h} \quad (3.6)$$

where δ_{LCE} is the thickness of the LCE motor unit ($\delta_{LCE} = 10\ \mu m$), K_{LCE} is the thermal conductivity of the LCE (0.6 W/m/K from reference [55]) and h is the heat transfer coefficient (air,

free, 10 W/m^2/K, from reference [86]). After plugging those numbers in to the equation, we have $Bi \approx 0.0002 \ll 1$. Therefore, we can assume the temperature in the LCE is homogeneous.

The thermal loss the film results from radiation and convection, which can be modelled by the following equations:

$$P_{radi}(t) = (e_{LCE} + e_{Au})\sigma_{s-B} L_{LCE} W_{LCE}\left(\mathrm{T}(t)^4 - \mathrm{T}_\infty{}^4\right), \quad (3.7)$$

and

$$P_{conv}(t) = 2hL_{LCE}W_{LCE}(T(t) - \mathrm{T}_\infty), \quad (3.8)$$

where P_{radi} is the power of heat dissipation through radiation, e_{LCE} is the emissivity of the LCE, e_{Au} is emissivity of the gold, σ_{s-B} is the Stefan-Boltzmann constant, L_{LCE} (W_{LCE}) is the length (width) of the LCE film ($L_{LCE}W_{LCE}$ gives area of surface for thermal energy dissipation), $\mathrm{T}(t)$ is the temperature of the LCE-based motor unit, T_∞ is the room temperature, P_{conv} is the power of heat dissipation through heat convection, h is the heat transfer coefficient,

As a result, the energy balance of the system is given by:

$$c_{LCE}m_{LCE}(T(t) - T_\infty) = \int_0^t [P_{in}(t) - P_{conv}(t) - P_{radi}(t)]dt, \quad (3.9)$$

where c_{LCE} is the specific heat capacity of the LCE and m_{LCE} is the mass of the LCE film. The values of all the parameters can be found in Table 3.1.

With any given voltage input profile ($V_p(t)$), we can obtain the temperature evolution of the LCE-based motor unit ($T(t)$) from (3.5) and (3.7) - (3.9). Finally, we can use this temperature profile as the input and calculate the dynamic performance (namely, $\varepsilon(t)$) of the LCE-based motor unit.

3.7.2 Temperature-dependent equilibrium strain of an LCE-based motor unit

To relate the temperature profile with the actuation dynamics of the LCE-based motor unit, we first have to measure the temperature-dependent equilibrium strain ($\varepsilon^*(t)$) of the LCE-based motor unit. Therefore, we put the unit inside a thermal chamber (TA ElectroForce 3300). We fixed one end of the unit and hanged a weight at the bottom. We gradually increased the temperature in the chamber from 20 °C to 160 °C. At each set temperature, we waited for 5 min to reach the steady state. Meanwhile, we used a digital camera (Canon 80D) to take photos of the motor unit. We measured its length under different temperatures by analyzing the images using ImageJ and then calculated the actuation strain. We further fit the results of temperature-dependent equilibrium strain using polynomial functions as shown in Figure 3.33. Next, we will relate the temperature profile solved from the voltage input profile with the experimental results we obtained here to find the dynamic behaviors of the LCE-based motor unit.

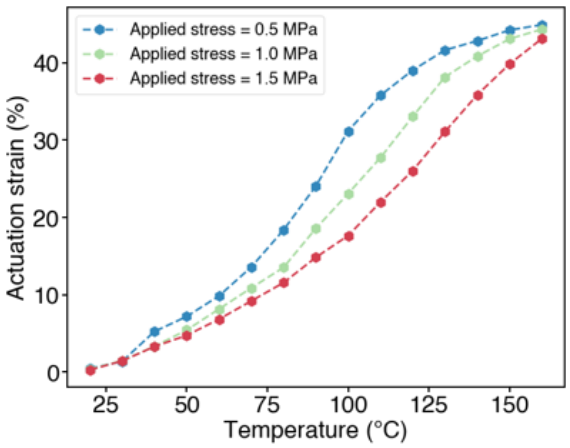

Figure 3.33: Experimental measurements of the equilibrium strain ($\varepsilon^*(T)$) of LCE motor unit versus temperature under different applied stresses (0.5 MPa ~ 1.5 MPa).

3.7.3 Electro-thermo-dynamic model

To predict the dynamics of the LCE-based motor unit with a hanging weight, we further adopted a mass-spring model (as shown in Figure 3.34A) to relate the mass of the hanging weight, its position, and the temperature in the LCE film based on the following equation:

$$m\frac{dx^2}{dt^2} + b\frac{dx}{dt} = k\left(l_0 - x - l^*\big(T(t)\big)\right), \qquad (3.10)$$

where x is the position of the weight and $x = 0$ at the beginning, m is the mass of the hanging weight, b is the coefficient of the damping, k is the spring constant of the LCE motor unit, l_0 is the initial length of the LCE film with a hanging weight before any stimulation, l^* is the equilibrium length of the LCE film, which is a function of the temperature of the LCE film, $T(t)$.

Recall the equations of natural frequency $\omega_n = \sqrt{\frac{k}{m}}$, the definition of damping ratio $\zeta = \frac{b}{2\omega_n m}$, the definition of actuation strain $\varepsilon(t) = x(t) \,/\, l_0$ and the definition of temperature-dependent equilibrium strain $\varepsilon^*(t) = (l_0 - l^*)/l_0$, (3.10) can be rewritten as:

$$\frac{d\,\varepsilon^2}{dt^2} + 2\zeta\omega_n\frac{d\varepsilon}{dt} + \omega_n^2\varepsilon = \omega_n^2\varepsilon^*(T(t)), \quad (3.11)$$

The term on the right-hand side of (3.11) provides the driving force for the oscillation of the motor unit, which is originated from the dependence of the equilibrium strain on the temperature changes: $\varepsilon^*(T(t))$. Such dependence can be measured experimentally with a constant applied stress of 1.5 MPa, a typical applied stress of the motor unit as shown in Figure 3.33. The dependence can be further given by a quadratic fitting, as shown in Figure 3.34B. Furthermore, we can solve the temperature profile *T*(t) of the LCE film under a given voltage stimulation by

solving the thermal equation involved with Joule heating, heat convection, and radiation as discussed previously. With the electro-thermo-mechanical model developed above, we can then predict the time varying strain of the LCE-based motor unit for quasi-static testing (Figure 3.34C, V_p = 5 V, f = 0.25 Hz, t_w = 0.5 s) and dynamic testing (Figure 3.34D, V_p = 30 V, f = 2 Hz, t_w = 4 ms).

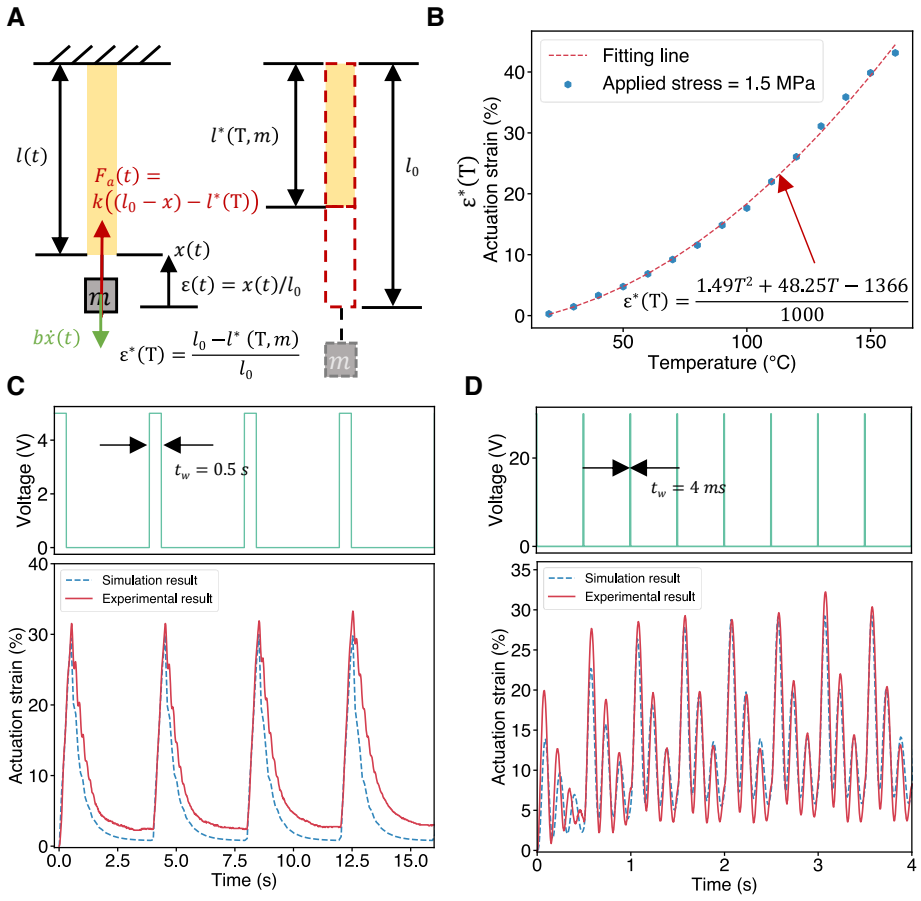

Figure 3.34: Electro-thermo-mechanical model of an LCE-based motor unit.
(**A**) Schematics defining the main variables of the system. (**B**) Experimental measurements of the equilibrium strain (ε*(T)) vs temperature under applied stress of 1.5 MPa and the associated quadratic fitting equation. (**C**) Comparison between the experimental result and simulation result of the actuation strain versus time in quasi-static case (V_p = 5 V, f = 0.25 Hz, t_w = 0.5 s, applied stress = 1.5 MPa). (**D**) Comparison between experimental result and simulation result of actuation strain versus time in dynamic case (V_p = 30 V, f = 2 Hz, t_w = 4 ms, applied stress = 1.5 MPa).

The value of input parameters in the electro-thermo-dynamic modeling is listed in the following Table 3.1. More simulation results under different voltage profiles can be found in Figure 3.35 and Figure 3.36. The prediction agrees well with the experimental data which confirms the validity of our thermo-mechanical dynamic model. Since the LCE-based motor unit is coiled due to the fabrication process, we cannot measure the surface temperature of the gold film directly. The electro-thermo-dynamic model we derived here provide us the indirect estimation of the surface temperature of the gold film sputtered on top of the LCE film.

Table 3.1 Value of input parameters in electro-thermo-dynamic modeling

Parameters	*Description*	*Value (unit)*
L_{LCE}	Length of the LCE film	40 (mm)
W_{LCE}	Width of the LCE film	1.8 (mm)
δ_{LCE}	Thickness of the LCE film	10 (μm)
m_{LCE}	Mass of the LCE film	1.2 (mg)
R	Resistance of the gold film	24 (Ω)
k	Spring constant of the LCE-based motor unit	4.24 (N/m)
m	Hanged weight at the end of motor unit in simulation	3.1 (g)
ζ	Damping ratio	0.1
σ_{s-B}	Stefan-Boltzmann constant	5.67×10^{-8} ($W/m^2/K^4$)
h	Heat transfer coefficient (air, free)	10 ($W/m^2/K$)
c_{LCE}	Specific heat capacity of the LCE	2000 (J/kg/K)
T_∞	Room temperature	25 (°C) or 298 (K)
e_{Au}	Emissivity of gold film	0.3
e_{LCE}	Emissivity of LCE film	0.9

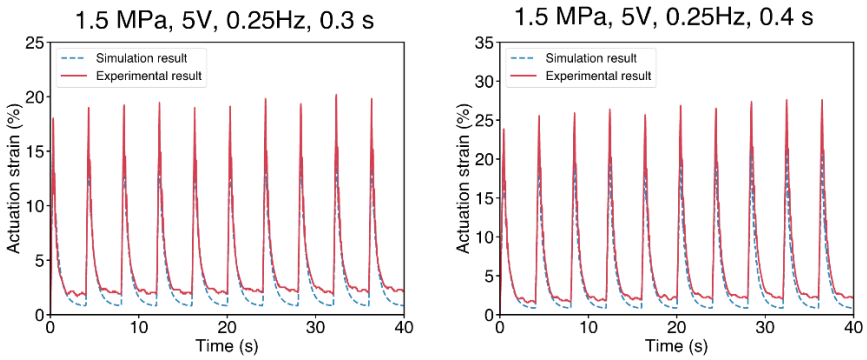

Figure 3.35: Comparisons between the experimental results and simulation results of the actuation strain in quasi-static cases (V_p = 5 V, f = 0.25 Hz, t_w = 0.3~0.4 s, applied stress = 1.5 MPa).

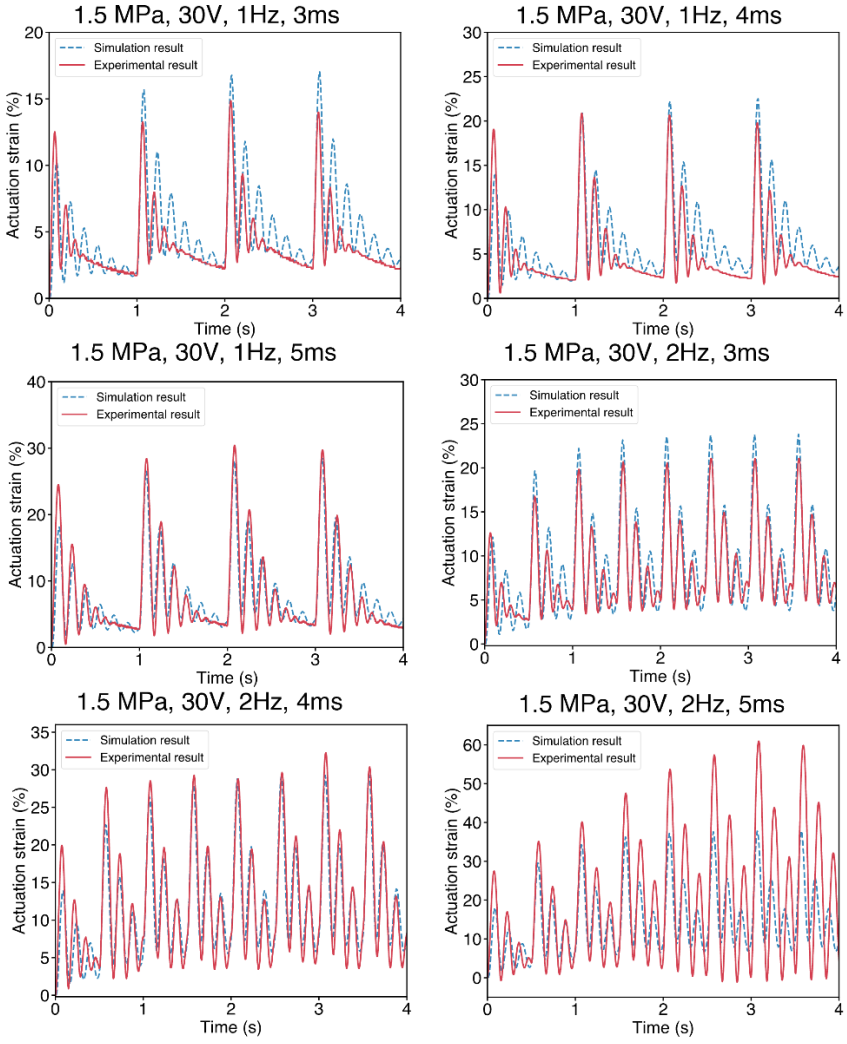

Figure 3.36 Comparison between the experimental results and simulation results of the actuation strain versus time for dynamic cases (V_p = 30 V, f = 1~ 2Hz, t_w= 3~5 ms, applied stress = 1.5 MPa).

3.7.4 Amplification of actuation strain and output power density through system resonance

Based on the model we derived, we can further explain the high output power density (1360 W/kg) of the LCE motor unit reported in this work. It can be partly explained by its resonance. Recall the equation of magnification factor in system undergoing a forced vibration:

$$|H| = \frac{1}{\sqrt{\left(1-\frac{\omega^2}{\omega_n^2}\right)^2 + \left(2\xi\frac{\omega}{\omega_n}\right)^2}} = \frac{1}{\sqrt{\left(1-\frac{f^2}{f_n^2}\right)^2 + \left(2\xi\frac{f}{f_n}\right)^2}} \quad , \quad (3.12)$$

where $|H|$ is the magnification factor, ω (or f) is the stimulation frequency, ω_n (or f_n) is the natural frequency, and ξ is the damping ratio. By plugging the numbers which we estimated from the model and measured from the experiment (ξ = 0.1 and f_n = 6 Hz), we have $|H|$ = 5 when f = f_n. We observed an actuation strain amplitude of 25% during the experiment (Fig. 1D) when resonance peak is approached. Taking the $|H|$ = 5 into consideration, we can estimate the equilibrium actuation strain (ε*) to be around 5%. Such small actuation strain can be produced in a short time through relatively slow cooling process. For example, we can estimate the characteristic time of convection as following:

$$\tau_{conv} \sim \frac{c_{LCE} m_{LCE}}{h L_{LCE} W_{LCE}} = \frac{c_{LCE} \rho_{LCE} \delta_{LCE}}{h} \quad , (3.13)$$

where ρ_{LCE} is the density of the LCE with a value of ~1.2 g/cm^3 (measured). After plugging the numbers of all the other variables (see Table S2), we have τ_{conv} of around 2.4 s. Even though the characteristic time of cooling is larger than 1 s, we can still realize an oscillation with frequency higher than 1 Hz (6 Hz) and with large actuation strain (~25%). Since power density can be estimated through:

$$power\ density \sim \frac{\sigma_a \varepsilon f}{\rho_{LCE}}, \quad (3.14)$$

where σ_a is the actuation stress and ε is the actuation strain amplitude during the oscillation. The combination of large actuation strain and stimulation frequency finally leads to a high value of power density.

3.8 Work loop of the artificial motor unit

Conventionally, artificial muscle has been often regarded as a synonym of soft actuator, which outputs positive work to the connected structures. However, it has been known that a muscle in animals behaves more than an actuator: it can also behave like a brake, spring, or strut [58]. From the energy perspective, during the motion of a muscle, it may output mechanical work, dissipate energy or store/release energy, which can be simply controlled by the time when the muscle is stimulated by a neuron signal [62]. Such multifunctionalities of the muscle can be classified through a standard technique called work loop technique. In this section, we will explore the multifunctionalities of the LCE-based motor unit using the work loop analysis.

3.8.1 Experimental setup and data processing of the work loop analysis

The key idea of work loop analysis in biology tests is performing cyclic displacement loading to the muscle while stimulating the muscle at different time through neural signals, during which the stress versus strain data is recorded as a work loop. Herein, we used a micromechanical tester (MFS, Linkam) equipped with a 2N loading cell to perform the cyclic loading. Once the LCE-based motor unit was fixed to the tester, the motors of the tester can be programmed to give controlled strain movements. The stimulation time is controlled by defining different phase values

in MATLAB which will further command the function generator (Keysight, 33500B) to generate corresponding control signals. The data processing procedures are shown in Figure 3.37:

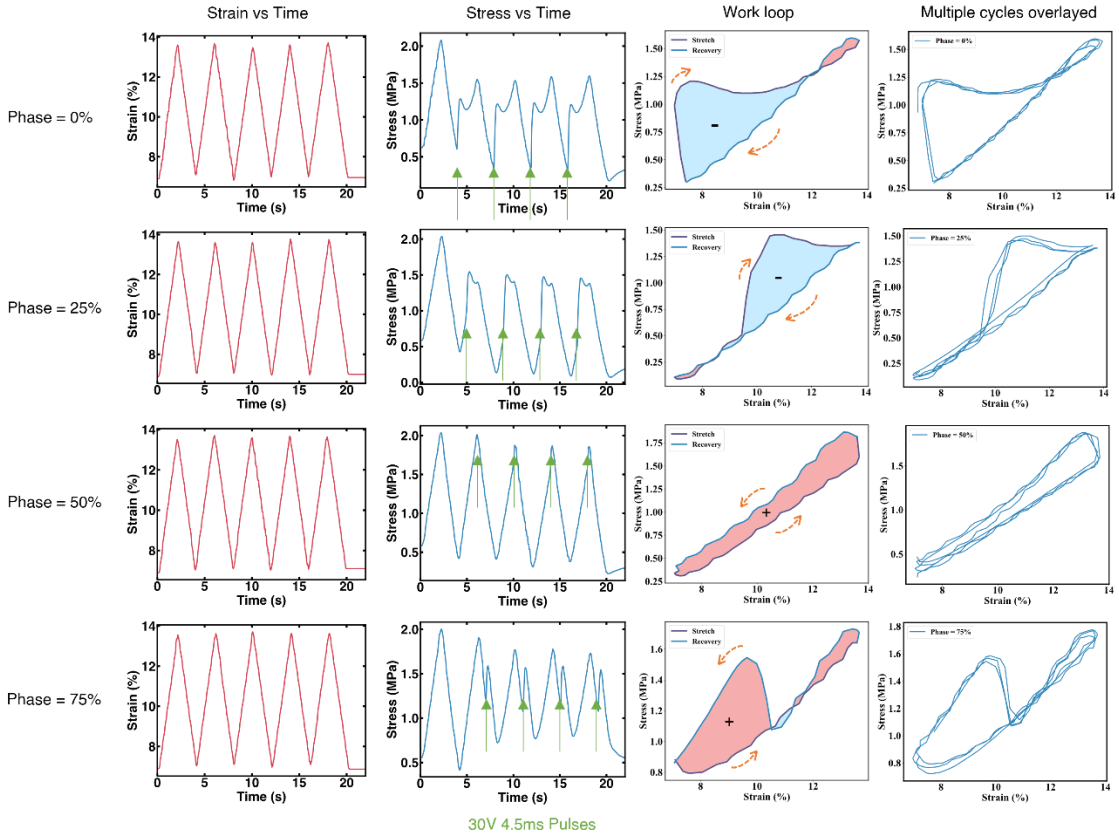

Figure 3.37: Data processing of the work loop experiment.

The LCE motor unit is controlled to cyclically deform from strain of 7% to 13% with a frequency of 0.25 Hz. A cyclic voltage pulse of 30 V with pulse width of 4.5 ms and frequency of 0.25 Hz is applied to the motor unit with phase values varies from 0% to 75%. We plot the work loop of the motor unit on the right two columns, which are based on the data of strain vs time and stress vs time shown on the left two columns. As a comparison, there is no voltage stimulation during the first strain cycle, and the shape change of measured stress can be clearly seen after the voltage stimulation is involved. We plot the work loops on the right two columns from the second cycle.

3.8.2 Analysis of the results

Using the work loop technique [87] (Figure 3.38A), we investigated the mechanical work and power output of the LCE-based motor unit by sending a stimulating signal to it at different times.

In the tests, the periodic voltage stimulation shares the same frequency as the controlled cyclic motion, while the phase (%) defined in Figure 3.38A tells the phase difference between the two

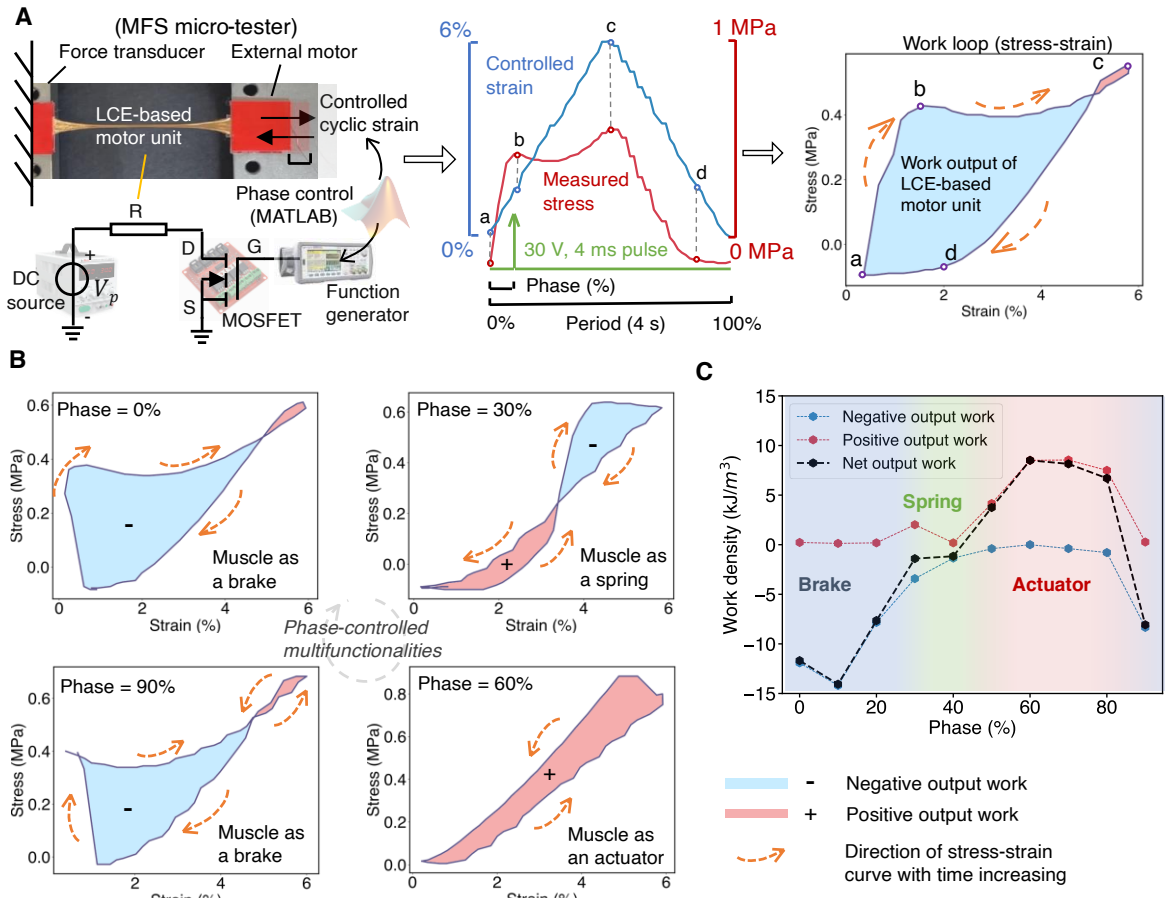

Figure 3.38: Work loop of the LCE-based motor unit.
(**A**) The setup of the work loop technique and the data processing procedure. (**B**) Typical work loop of the LCE-based motor unit by setting different phase values (0%, 30%, 60%, and 90%) indicating different functionalities as a brake, as a spring and as an actuator. (**C**) Output work density (in one cycle) of LCE-based motor unit for different phase values of the voltage stimulations. When the phase value is below 20% or above 90%, the LCE-based motor unit outputs negative total work (in one cycle) and behaves like a brake. When the phase value is 30% or 40%, the LCE-based motor unit outputs nearly zero total work (in one cycle) and behaves like a spring. When the phase value is between 50% and 80%, the LCE-based motor unit outputs positive total work (in one cycle) and behaves like an actuator/motor.

periodic events. We controlled the cyclic deformation of the LCE-based motor unit with the strain varying between 0% and 6% at a frequency of 0.25 Hz while stimulating it with voltage pulses (V_p

= 30 V, t_w = 4 ms) of the same frequency (0.25 Hz) but at the phase varying from 0% to 90%. Both real-time strain and stress data were collected simultaneously to generate work loop plots (stress versus strain) as shown in Figure 3.38A. We show four typical work loops (phase = 0%, 30%, 60% and 90%) in Figure 3.38B.

3.8.3 Phase-controlled multifunctionalities of the LCE-based motor unit

To understand the energetic process in the LCE more quantitively, we further studied and calculated its output work density within one cycle based on the work loop plots with stimulation signals at different phases as shown in Figure 3.39:

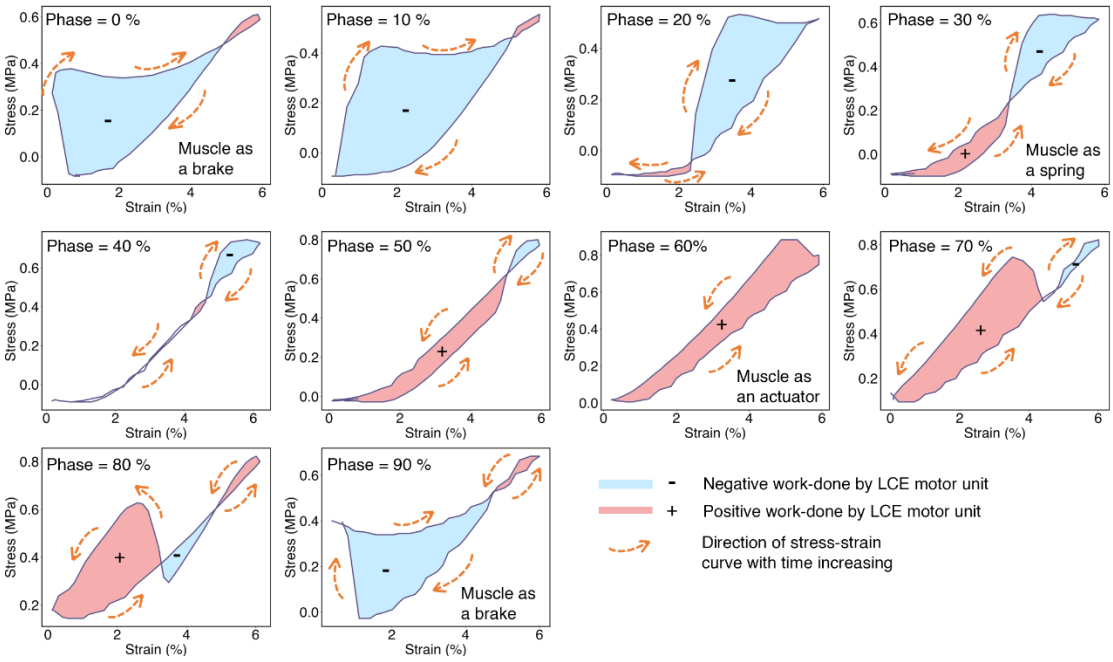

Figure 3.39: Work loops of the LCE-based motor unit for different phases (0% ~ 90%) when the stimulating voltage pulse (30 V, 0.25 Hz, 4 ms pulse width) was applied. Different shapes and directions of the loop indicate different energy conversion processes in the motor unit.

Same as Figure 3.38, the direction of the work loop determines whether the LCE produces negative work (absorb energy) or positive work (output energy), which can be tuned by the phase when the stimulation signal is sent. During the tests, the LCE-based motor unit can behave differently as a brake (phase = 0% and 90%), as a spring (phase = 30%) or as an actuator/motor (phase = 60%), which is similar to the performance of animal muscles [58].

We integrated the area inside the work loop to obtain the positive work (counterclockwise loop), negative work (clockwise loop) done by the LCE-based motor unit within one cycle of movement. For some cases (as shown in Figure 3.39), we found two work loops in the stress versus strain plots. As a result, in one cycle of motion, we computed the two work densities for the two work loops separately, as shown in Figure 3.38C. By adding up the two works, we obtained the net output work of the LCE-based motor unit in one cycle of movement for different phase values. Based on that, we were able to better classify the behaviors the LCE-based motor unit based on the energetic process, as shown by different colors in Figure 3.38C: brake-like behavior (negative work in one cycle); actuator-like behavior (positive work); and spring-like behavior (nearly zero output work).

3.9 Dexterous artificial neuromuscular system

3.9.1 Demonstrations with open-loop control

Thanks to its fast response and the easy controllability, we next integrated the LCE-based motor unit with various sensory components and a control system to build an artificial neuromuscular system. First, we demonstrated an autonomous object capturing by the system, inspired by the ruler drop test (Figure 3.40A) for assessing the reaction time of a person. An optical sensor was used to mimic the visual systems (eyes) of human in the system. We created the components of the falling object catching frame from acrylic plates (thickness of 3 mm) using a laser cutting machine (OMTech). The gripper is made with a 3D printer (Flashforge Guider II). An LCE-based motor was adhered to the gripper to provide actuation. Carbon reinforced fiber (McMaster) with diameter of 1 mm is used as gripper sliding guides. Photoresistor modules (Gowoops) was used as the optical sensor and Arduino Mega 2560 was used as the microcontroller instead of the function generator. We used DC power source (Dr. Meter PS-305DM) to provide the heating power with V_P set at 30 V. We used small magnets keep the gripper at its opened state before we dropped the object, and the LCE-based motor unit was thus in a pre-stretched state. A voltage pulse with length of 5 ms can be generated by the Arduino once the falling object blocks the light sensed by the photoresistor. The whole system thus formed an open-loop control, as shown in Figure 3.40B.

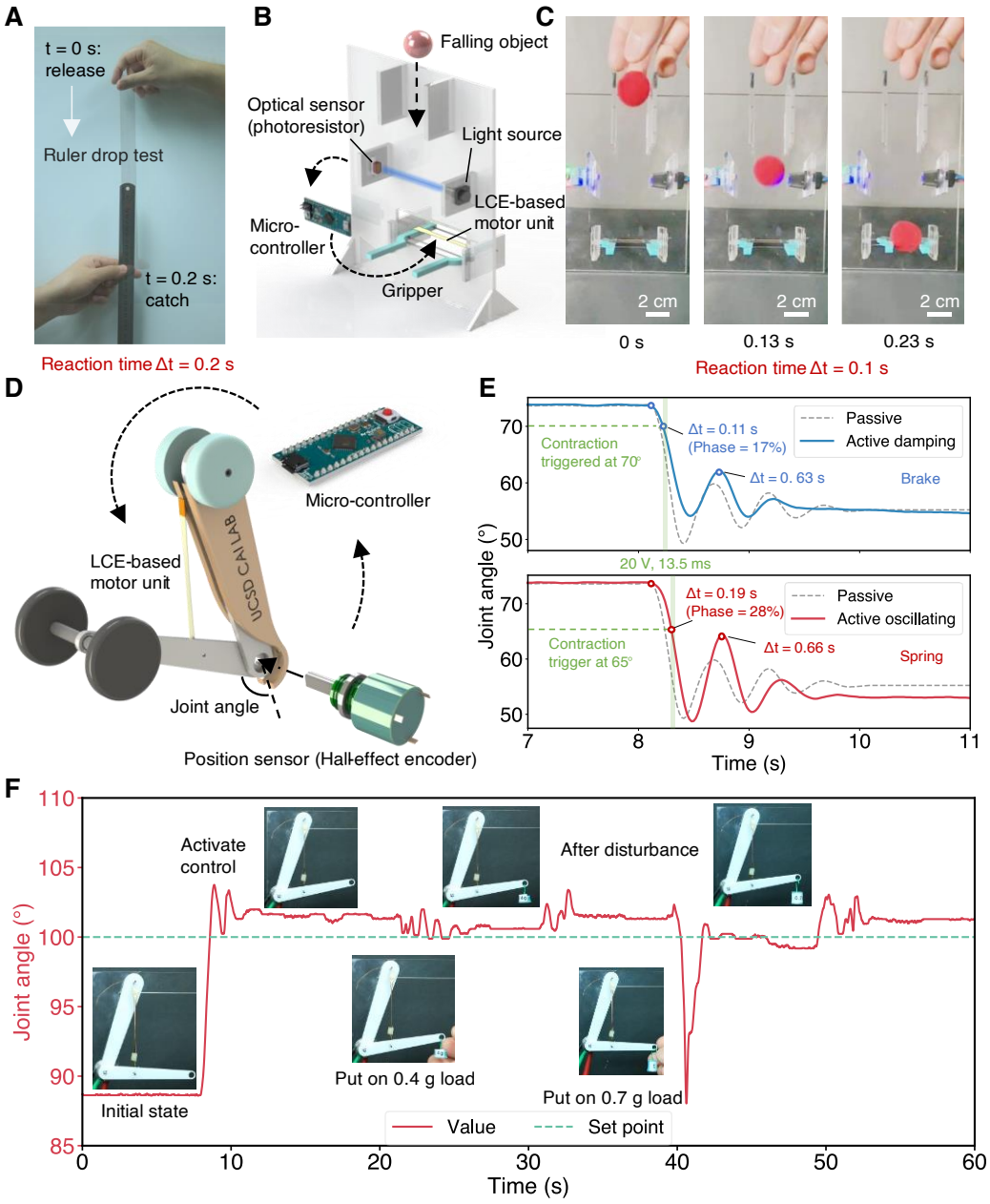

Figure 3.40: Dexterous artificial neuromuscular system.

(**A**) Ruler-drop test for estimating the reaction time of a person. (**B**) Schematics of system integrated by the LCE motor unit, an optical sensor and a microcontroller which can capture a falling object. (**C**) Images show the object capturing process. The system has a reaction time (0.1 s) comparable to a person (0.2 s). (**D**) Schematics of the LCE-based motor unit integrated with a position sensor forming an arm-joint system. (**E**) By controlling the stimulation time of the LCE motor unit, the oscillation dynamics of the arm after one perturbation can be tuned. During the oscillation, the LCE motor unit acts differently as a brake or as a spring. (**F**) Active close-loop PID control of the joint angle. The joint angle is maintained at the set point with different disturbances.

As shown in Figure 3.40C, once a falling ball blocked the light from the LED, a triggering signal was generated by the optical sensor and sent to the micro-controller, and then the micro-controller generated a stimulation voltage pulse and triggered the MOSFET to provide the LCE with thermal energy to contract and catch the falling ball. The whole process resembles the brain controlling the finger movements to catch the ruler through visual feedback in reaction time test. It is noted that the reaction time of our artificial neuromuscular system (0.1 s) is comparable to the average reaction time of human being (0.2 s), indicating the high dexterity of the artificial neuromuscular system.

We next integrated the LCE-based motor unit with a position sensor to mimic the control of forearm through biceps of a person, as shown in Figure 3.40D. We fabricated the forearm from acrylic plates (thickness of 1 mm) using a laser cutting machine (OMTech). We installed one Hall-effect encoder (CALT) at the joint position to read the joint angle in real time, and we used Arduino Mega 2560 as the microcontroller. We fixed the arm-joint structure to an acrylic frame which was also fabricated through laser cutting (OMTech). The hall-effect sensor was installed at the joint position to detect the joint angle of the arm (defined in Figure 3.40D). An LCE-based motor unit was used to move the arm. As shown in Figure 3.40E, initially, the joint angle equals 72°. After we suddenly hung a weight of 0.7 g at the end of the lower arm, the arm fell down and oscillated for several cycles before reaching the equilibrium position, as shown in Figure 3.40E. As we have shown previously through the work loop technique, the timing difference between the mechanical

movements and the stimulation signals can dramatically change the functionality of the LCE-based motor unit.

We next showed that the LCE-based motor unit behaved like a brake. When the arm fell down, the joint angle detected by the position sensor decreased. Once the joint angle passed a pre-set joint angle (trigger angle, set to be 70°), a pre-programmed voltage pulse was sent from the microcontroller to the motor unit to trigger the contraction of the LCE. After a sudden release of a weight of 0.7 g, as shown in Figure 3.40E (blue curve), the amplitude of the arm oscillation decreased and the number of oscillation cycles also reduced before the arm reached the equilibrium, as compared to the experiment without stimulating the LCE (grey dash curve in Figure 3.40E). In this case, the LCE-motor unit behaved like a brake, dissipating the mechanical energy of the system, which also resembled eccentric contraction of muscles. In contrast, the amplitude of the arm oscillation increased slightly (red curve in Figure 3.40E), if we set the trigger angle as 65° in the experiment with the same electrical signal being employed. In this case, the LCE-motor unit behaved like a spring, slightly reducing the system damping. Based on the work loop results shown in Figure 3.38C, we can readily understand the behaviors of the LCE-motor unit described above. We regard the ratio between the time when the triggering signal was sent and the time when the arm reached its highest position as the phase value in Figure 3.38C. If the trigger angle is 70°, the phase is 17%, and consequently, the LCE behaves like a brake according to Figure 3.38C, which is consistent with the results shown in Figure 3.40E. Likewise, if the trigger angle is 65°, the phase is 28%, and consequently, the LCE behaves like a spring according to Figure 3.38C.

3.9.2 Demonstrations with close-loop control

At last, we demonstrated a close-loop proportional–integral–derivative (PID) control of the joint angle, as shown in Figure 3.40F. Herein, we showed the arm could be stabilized around the set point with joint angle of 100°. In the demonstration of PID control based on joint-arm system, we programmed the Arduino controller to continuously generating 50 Hz PWM control signals with tunable duty cycle between 0% to 60%. Safety limit of the duty cycle was set as 60% to protect the motor unit from overheating. We set the voltage of DC power source (Dr. Meter PS-305DM) to 5 V. The script encoded in Arduino continuously calculates the error ($e(t)$) between the current joint angle measured through Hall-effect encoder and our set point. Through the pre-programmed PID controller (library, PID_v1), we then adjusted the duty cycle of the stimulation voltage pulses accordingly to approach the target value of the joint angle following the control function as:

$$u(t) = K_P e(t) + K_i \int_0^t e(\tau)\, d\tau + K_d \frac{de(t)}{dt}, \quad (3.15)$$

where $u(t)$ is the output duty cycle, and K_P, K_i, K_d are the coefficients for the proportional, integral, and derivative terms respectively.

In the experiment, we dropped a load (0.4 g or 0.7 g) at the end of the arm. It is shown that with these perturbations, the joint angle can be stabilized around the set value through effective PID control within several seconds. The response speed we showed here was significantly faster than the previously reported close-loop control results using LCE-based actuator [88], which made our motor unit more adaptive to the random disturbances from the environment. As shown in

Figure 3.41, we introduced several random disturbances to the front arm, but the joint angle quickly went back to its set level.

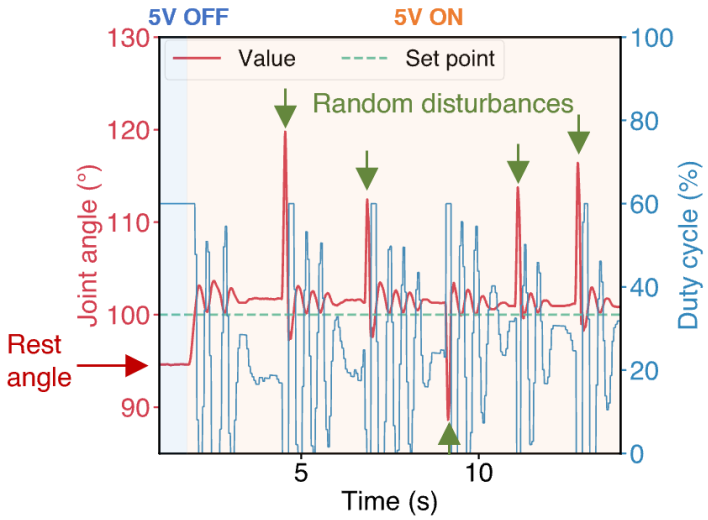

Figure 3.41: Active close-loop PID control of the joint angle.
The joint angle maintained at the set point after random disturbances. The red curve shows the joint angle versus time while the blue curve shows the duty cycle of the actuator calculated from the PID controller.

3.10 Conclusion

In summary, in this chapter we demonstrate an LCE-based motor unit, which exhibits muscle-like performance in terms of large actuation strain/stress, high power density, large bandwidth and so on. Though various soft actuators, sensors, and the control systems associated with them have been intensively explored in the past, the compact integration of these elements has been much less studied, which hinders the construction of dexterous soft robots. In this study, we developed a gold-film-coated ultrathin LCE-based motor unit which was electronically controlled. The wrinkled configuration of coated gold film enabled its great stretchability. The entire fabrication process of the LCE-based motor unit reported is compatible with the well-established 2D planar

microfabrication techniques, making the scale up of the production extremely facile. We further demonstrated that the LCE-based motor unit showed a superior actuation performance with the main performance metrics (actuation strain, actuation stress, power density and bandwidth) close to or outperforming those of biological muscles. Recently, it has been demonstrated that a high actuation frequency of a thermally driven nylon-based artificial muscle in either helium or water [4]. Our current design realized the same high frequency of 6 Hz at room temperature in air.

Moreover, the electronical controllability of the LCE-based motor unit makes it compatible with most electronic devices. Integrating the LCE-based motor unit, sensors, and electronic control systems, we can easily build an artificial neuromuscular system, which shows great dexterity in autonomous robotic structures. Like biological muscles, by varying the time of sending the stimulating signal, we demonstrated that the LCE-based motor unit could behave as an actuator, a brake, or a spring in a mechanical system.

Finally, we would like to the discuss the future research opportunities based on the design presented in the current study.

(1) Though we only demonstrated a simple motion (contraction) of the LCE-motor unit in this work, more complex motions can be easily achieved with different arrangement of multiple motor units.

(2) The fast response of the LCE-motor unit results from the ultrathin LCE structure, with sacrificing the magnitude of the actuation force. Increasing the actuation force could be achieved

by the assembly of multiple thin LCE film-based motor units, like the structural hierarchy of a biological muscle.

(3) Though we have only demonstrated the artificial neuromuscular system with optical sensors and Hall-effect sensor, they can be easily replaced by different types of sensors for various purposes.

(4) Our results showed that the LCE-based motor unit can stably generate a cyclic strain of 25% for more than 400 cycles without performance degradation, but its actuation performance decreased significantly after 800 cycles of contractions (Fig. 3.42). It is worthwhile to further improve the durability of the gold-film-coated thin LCE film structure.

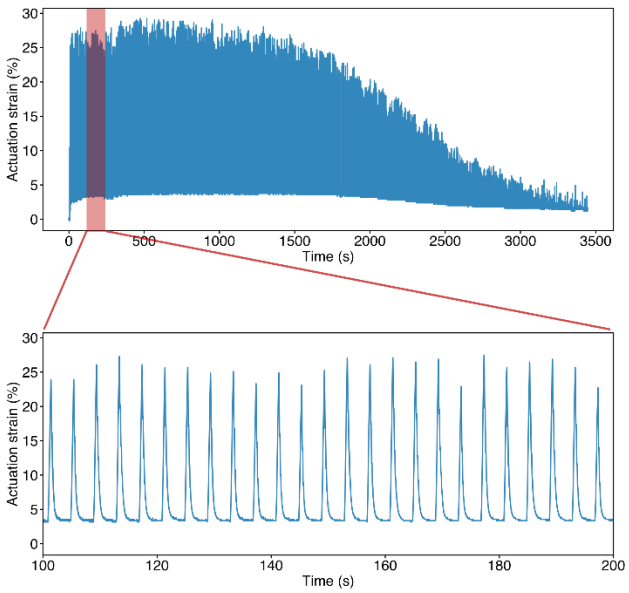

Figure 3.42: Durability of the LCE-based motor under cyclic actuation.
A voltage pulse of 5 V with frequency of 0.25 Hz and pulse width of 0.5 s is cyclically applied to the LCE motor unit, during which the motor unit can generate a cyclic strain of 25% for more than 400 cycles without performance degradation, but its actuation decreases significantly after 800 cycles.

(5) For small structures like microrobots (less than 1 cm), a smart material-based actuation mechanism shows a great advantage over electrical motor-based ones on actuation mechanism. Though the prototype shown in the current study is not small, it is not hard to significantly shrink the physical size of the entire system for a more compact design [8].

Acknowledgements

Chapter 3, in full, is currently being prepared for publication by Yang Wang, Qiguang He, Zhijian Wang, Shengjia Zhang, Chenghai Li, Zijun Wang, Yong-Lae Park, Shengqiang Cai. The dissertation author was the primary investigator and first author of this paper.

Chapter 4 Stretchable and Transparent Ionic Diode and Logic Gates

4.1 Introduction

Hydrogel is a crosslinked polymer network swelled in water. Volume percentage of water in a fully swollen hydrogel can be as high as 95%. Thanks to many appealing features of hydrogel such as the high fluid permeability, high optical transparency, excellent biocompatibility, various applications of hydrogels have been explored during the past several decades. Most notable applications of hydrogel in the past include contact lens, drug carrier, diapers, and wound dress [89-94]. In recent years, some unusual applications of hydrogels have been proposed, which include ionic conductors for neuron probe [95, 96], transparent loudspeaker [97], stretchable ionic cables [26], stretchable sensors [28, 98], electroluminescent device [99] and flexible displays [100].

Considering that biological system is usually wet and ionic, it has been proposed to make ionic device using hydrogels as complementary to traditional electronic devices [24, 101-107]. Ionic conductor/ionic cable can be regarded as the most basic element for ionic devices. Besides ionic conductors and cables, it can be expected that, analogous to electronic diode, ionic diode can be integrated into ionic devices with advanced functions. As a matter of fact, ion channels in biological cells are often regarded as ionic diodes, where the ion flows ("current") can be regulated by the membrane potential ("voltage") [108].

The idea of solution-based ionic diode can be traced back to ionic bipolar membrane structure first proposed by Frilette [109]. Following this initial idea, many similar structures have been designed and studied [96, 110, 111]. Recent examples include ionic diode in a microchip [27, 112] and a full-wave ionic current rectifier [113]. In all those devices, ionic diodes are in liquid state, which can potentially result in several technique problems in the real applications such as liquid leakage and the difficulties of assembly and packaging. Researchers have recently fabricated ionic diode using polyelectrolyte gels such as agarose and cellulose [25, 114, 115]. However, hydrogels used in most previous studies are brittle and can be easily fractured under small stretch, which limits their applications in stretchable and wearable devices. In addition, no study has been conducted to investigate how the mechanical deformation of a hydrogel diode may affect their electrical performance.

In this work, we fabricate ionic diode using highly stretchable PAAm (polyacrylamide) gel doped with two different polyelectrolytes with opposite fixed charges. Thanks to the high stretchability of the ionic diode, in the article, we study how mechanical stretch can affect the electrical performance of the ionic diode. We further investigate the capability of the diode of sustaining cyclic mechanical stretch. We also construct two logic gates using the hydrogel-based ionic diodes. Potential applications of the stretchable hydrogel ionic diode developed in the current work may include human-machine interface, wearable devices, stretchable ionotronics and soft machines.

4.2 Results and discussion

4.2.1 Synthesis of polyelectrolyte doped hydrogels

Analogous to the doping in semiconductors, polyelectrolytes with opposite charges can serve as dopants in hydrogel-based ionic diode. We adopt poly(sodium 4-styrenesulfonate) powder (PSS, Sigma Aldrich 243051, MW 70kDa) and poly(diallyldimethylammonium chloride) solution (PDAC, Sigma Aldrich 409030, MW400-500kDa) as the doping polyelectrolytes. To fabricate PSS-doped PAAm gel, we first dissolve monomer acrylamide (AAm) powder (Acros) (14.0wt %) and PSS powder (7.0wt %) in Milli-Q water, then add cross-linker N,N'-methylenebisacrylamide (MBAA) (Sigma Aldrich, M7279) 0.14mol % with respect to AAm and initiator (2-hydroxyethoxy)-2-methylpropiophenone (HHMP, Sigma-Aldrich,95%) 0.49mol % with respect to AAm. We then stir the mixture continuously at room temperature until it forms a transparent and homogeneous solution. After degassing the solution, we pour the solution into a glass mold and seal it well with glass slide. The gels are cured under UV irradiation for 1 hour. Synthetic processes of PDAC-doped hydrogels are almost the same except for: (1) PDAC is initially in solution state and the doping ratio of PDAC is 5.0wt%; (2) the corresponding amounts of MBAA, HHMP is 0.028mol % and 0.49mol % with respect to AAm monomers.

4.2.2 Fabrication of hydrogel-based ionic diode

An ionic diode composed of a pair of hydrogels doped with PSS and PDAC, respectively, is shown in Figure 4.1. As shown in Figure 4.1A, we first cut both PSS-doped and PDAC doped PAAm hydrogel (with the thickness of 1.5mm) into isosceles trapezoid shape with two bases of

10mm and 5mm long, respectively. We then cut a dumbbell-shaped hole, which fits to the shape of the hydrogel diode, from two stacked VHB films (4910 and 4905, 3M company), acting as the spacer in the sandwich structure. To reduce the water evaporation, we cover the hydrogel diode by two additional stretchable VHB films (4905, 3M company) of rectangular shape with the dimension of 3cm x 2cm. We use platinum foils (99.9%, 0.025mm thick, Sigma Aldrich 267244) to connect the diode to external electrical circuits, as shown in Figure 4.1A. We fabricate the hydrogel ionic diode by assembling all the components mentioned above and then connect it with an external source measure unit (SMU, Keysight) to conduct later measurements.

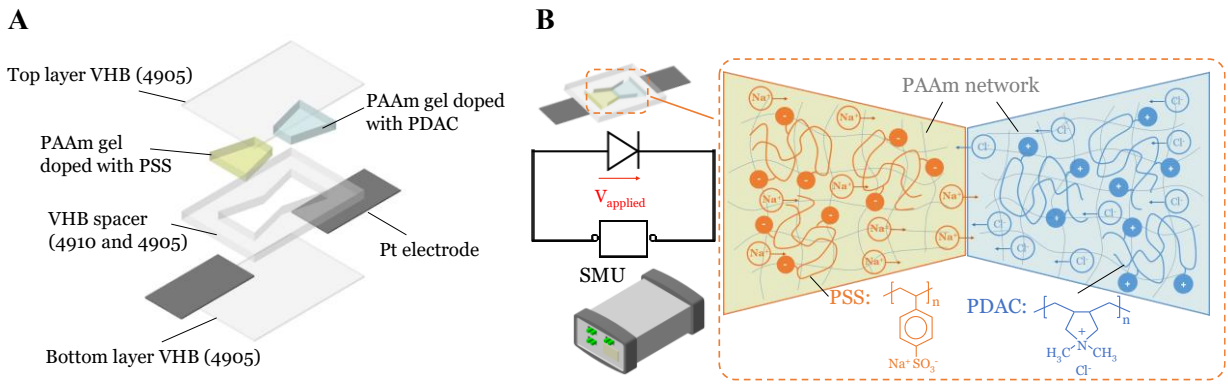

Figure 4.1: Structure and fabrication of a hydrogel-based ionic diode.

(A) The components of a hydrogel-based ionic diode. (B) Schematic of the ionic diode after assembly, and its electrical testing circuit for obtaining its IV characteristic curve. The movement of the counterions is shown in the schematic when forward-bias voltage is applied onto the diode.

4.2.3 Experimental setup

The testing electrical circuit for obtaining the characteristic curve of Current (I) vs. Voltage (V) of the hydrogel diode (IV curves) is shown in Figure 4.1B. We use one Source Measure Unit (SMU) (Keysight, U2722A) to output voltage and measure the current simultaneously. Scanning

and sampling processes of U2722A are controlled through VISA interface supported by MATLAB. We set the bias voltage to sweep from a reverse-bias voltage to a forward-bias voltage (e.g. -4.5V to +4.5V) with a fixed ramp rate of 2mV/s. By recording the corresponding current variations, we are able to obtain the IV characteristic curves of the hydrogel diode. According to the previous studies, the distribution of non-reactive counterions from the polyelectrolytes in the hydrogel determines its current rectification behavior [116]. However, it takes time for the ions to redistribute when external electric field varies too quickly. Therefore, a constant reverse-bias voltage (e.g. -4.5V) is applied to the diode for 5 minutes before each sweep scanning starts, so steady state distribution of counterions can be guaranteed before each scanning test.

We conduct electrical measurements of the hydrogel ionic diode after it is subjected to cyclic mechanical stretching. In the experiments, we attach the two ends of the diode onto two acrylic plates, which are then tightly clamped by the grippers of a universal mechanical testing machine (Instron 5965). The aforementioned IV characteristic tests of the diode in a free-standing state are performed after it is subjected to every 80 cycles of stretching.

We also construct two ionic logic gates: OR gate and AND gate. We use hydrogel-based ionic diodes together with metallic film resistors (PIXNOR) and one resistor decade box (Extech 380400) to build up the two logic gates. For the AND gate, we use one more DC voltage source (Dr. Meter HY1803D) as its power supply. Details of the circuit diagram of the logic gates are discussed in next section. To verify that the two logic gates can perform the expected logic operations, we use U2722A to construct the test circuits. Thanks to the independence of three

channels of U2722A, we program two of them to generate square wave voltage signals as binary inputs for logic gates, like function generators. We then make use of the third channel to measure the voltage signals at the output terminal of logic gates simultaneously.

4.2.4 Stretchable and transparent diode with rectification effect

We first demonstrate that the PAAm hydrogel-based ionic diode fabricated in the current work is highly stretchable and transparent. As shown in Figure 4.2A, the length of the fabricated ionic diode can be stretched by more than 6.5 times without rupture. High transparency of the ionic diode is also maintained during the stretch as shown in Figure 4.2B.

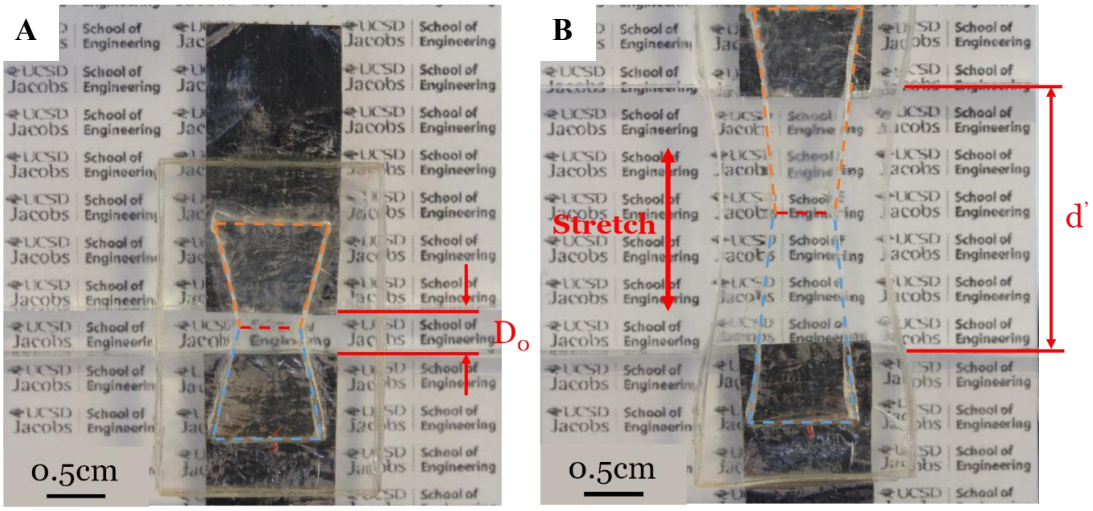

Figure 4.2: High transparency and stretchability of hydrogel-based ionic diode.

(**A**) The ionic diode in undeformed state: the diode is attached to two acrylic plates with the clearance of 4mm, denoted by D0. The texts on the background can be seen clearly through the diode; (**B**) Ionic diode with a stretch $\lambda = d'/D_0$.

We next study current rectification of the ionic diode when it is subjected to different stretches. By using a customized stretch device, we are able to measure the IV (Current-Voltage) characteristic curves of the ionic diode under different stretches. As mentioned in the measurement

section, we adopt Source Measure Unit to perform all the electrical tests. We apply the similar test procedure to diode samples subjected to different stretches ranging from 1.0 to 4.0 (the definition of stretch can be found in Figure 2). For undeformed state (or stretch equal to 1.0), we use (-4.5V, 4.5V) as the scanning scope. For stretched state, we use the scanning scope of (-5.5V, +5.5V), (-7.0V, +7.0V) and (-7.5V, +7.5V) for the stretch equal to 1.5, 3.0 and 4.0, respectively. In Figure 4.3, we show the measured IV characteristic curves of the diode with different stretches. In the undeformed state (stretch=1.0), the current passing through the diode is around 3mA when the bias voltage is +4.5V.

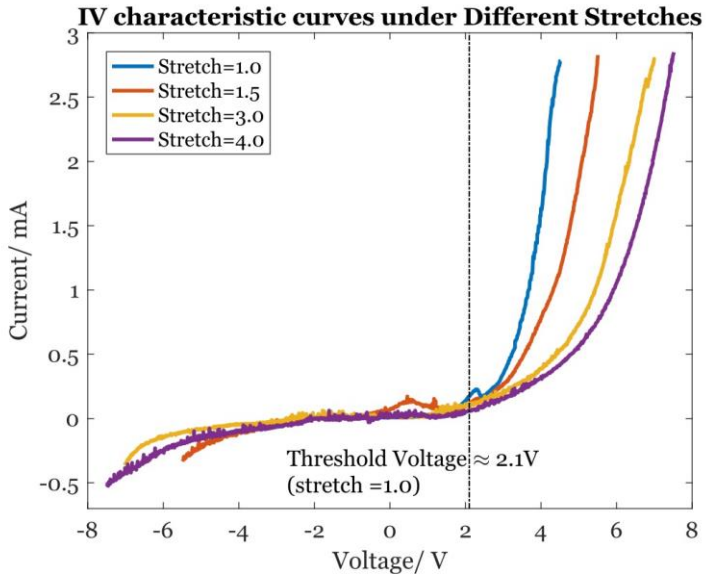

Figure 4.3: Current-Voltage characteristic curves of the ionic diode with several different stretches. The voltage threshold of the ionic diode with no stretch is around 2.1V. Rectification behavior of ionic diode is mostly maintained as stretch increases.

The current density across the interface of two hydrogels (the red dash line shown in Figure 4.2A) is around 40mA/cm2. The rectification ratio, defined as the ratio between the current measured at +4.5V and that measured at -4.5V, is around 18.5. Both rectification ratio and

current/current density of the hydrogel diode are all comparable to those values reported in the previous studies [114, 115].

As shown in Figure 4.3, we find that large rectification ratio of the diode can be still maintained for moderate stretch. At the maximal reverse-bias and forward-bias voltage, we have the rectification ratio of 9.1, 7.7 and 5.6 for the stretch of the diode equal to 1.5,3.0 and 4.0, respectively. The effects of the stretch on the rectification ratio can be roughly understood as following: although the main voltage drops happen at gel-electrode interface and gel-gel interface [116], the additional voltage drop inside the gel is responsible for the effects of the stretch on the performance of the diode. With the increase of the stretch, the length of gel diode increases and its cross-sectional area decreases. Such geometry change directly leads to the change of electrical resistance of the gel. Therefore, compared to the undeformed state, larger external voltage is needed for a stretched diode to obtain the same potential drop at the interfaces. For example, as shown in Figure 4.3, to generate the same current in a unstretched diode subjected to 4.5V forward-bias voltage, 5.5 V forward-bias voltage is required for the diode with stretch of 1.5.

4.2.5 Electrical performance of ionic diode under cyclic loading

We also measure the IV characteristic curves of the hydrogel diode after it is subjected to cyclic mechanical stretching. We cyclically stretch the diode for 80 times with the maximal stretch of 2.5 and with a fixed strain rate of 25% s^{-1} as shown in Figure 4.4A. We measure the IV characteristic curves of the diode after every 80 cycles as shown in Figure 4.4B. It can be clearly

seen that the performance of the diode has been almost unaffected by the cyclic stretching, which is important for the ionic diode for long-term applications.

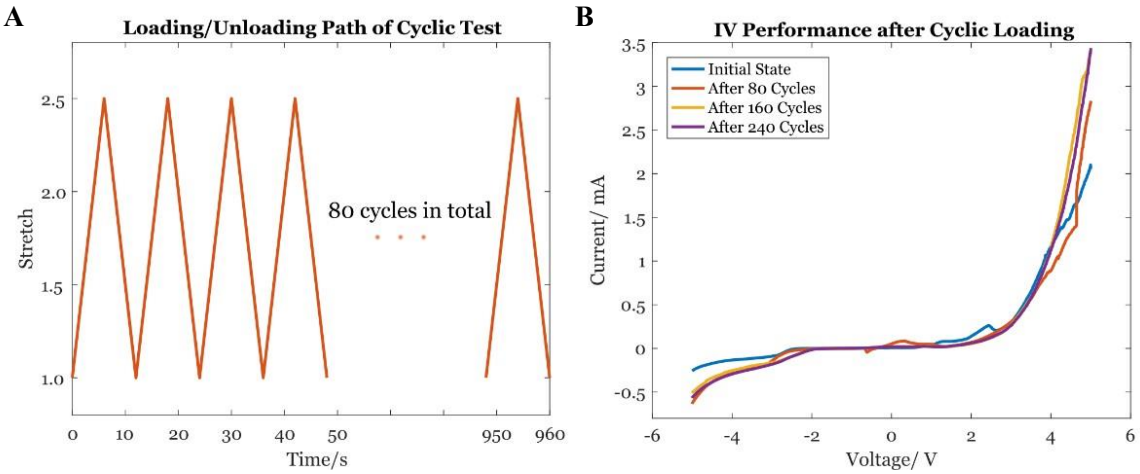

Figure 4.4: Performance of the hydrogel-based ionic diode after cyclic stretch.

(**A**) Cyclic stretch is applied onto the hydrogel ionic diode. The maximal stretch is set to be 2.5. (**B**) IV characteristic curves of the ionic diode after every 80 cycles of stretch. The performance of the diode changes negligibly after total 240 cycles of stretch.

4.2.6 Ionic logic gates

To further demonstrate the functionalities of the hydrogel diode in ionic circuits, we build two ionic logic gates: OR gate and AND gate. From the previously obtained IV characteristic curves of the diode as shown in Figure 4.3, we can identify a stable threshold voltage of it in undeformed state, which is around 2.1V (the dash line in Figure 4.3A). If the voltage across the ionic diode is larger than the threshold voltage, it is considered as conductive. Otherwise, the diode is regarded as non-conductive. Based on that, we construct the hydrogel-based ionic logic gates as shown in Figure 4.5 and Figure 4.6.

The hydrogel-based OR gate is shown in Figure 4.5A. When voltage at either the input terminal A or B is higher than the threshold voltage (2.1V), e.g., 4.5V, the corresponding ionic diode is considered as conductive as explained above. Consequently, the voltage at the output terminal C1 should be high or in logical "1" state. To verify that in the experiments, voltage signals with the shape of square waves of designed frequencies ($f_A \approx 0.018$ Hz, $f_B \approx 0.036$ Hz, $f_B = 2 f_A$) are programmed to be the inputs of the OR gate.

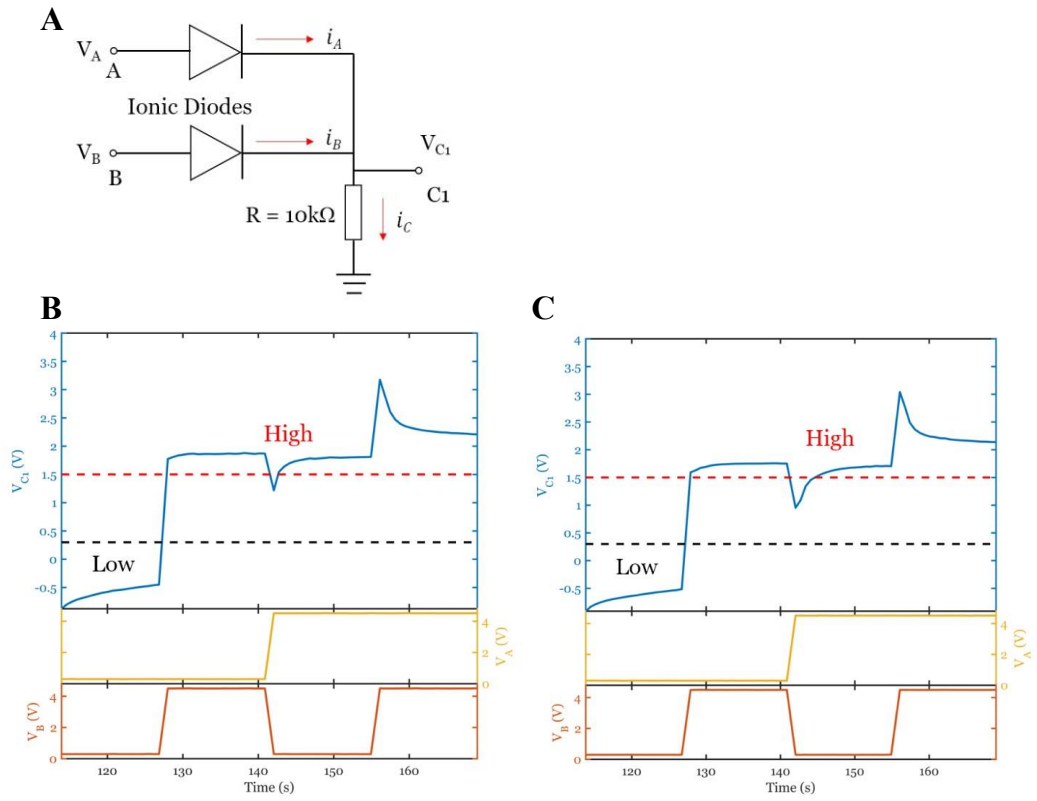

Figure 4.5: Hydrogel-based ionic OR gate.
(**A**) A circuit diagram of an ionic OR gate. A and B are the input terminals and C1 is the output terminal. (**B**) Demonstration of the logic OR operation: square waves with certain frequencies are programmed as binary inputs for the OR gate. Logic stated (0,0), (0,1), (1,0), (1,1) are generated as the inputs periodically. Voltage at C1 is measured as the output. The results confirm that this logic gate implements the logical expression: C1= A OR B. (**C**) Performance of OR gate under stretch state. Both of the two ionic diodes are stretched to 1.5 times of their original length. Input signals are the same as the ones in undeformed state.

As a consequence, all logic state combinations as inputs can be realized periodically (e.g. (0,0), (0,1), (1,0), (1,1)). The output voltage at terminal C1 (Figure 4.5A) is shown in Figure 4.5B. When the input voltage at either A terminal or B terminal is high (or in logical "1" state), the output voltage at terminal C1 is high or in logical "1" state (signal is higher than the red dash line in Figure 4.5B). When the input voltage of both A terminal and B terminal are low (or in logical "0" state), the output voltage at terminal C1 is low or in logical "0" state (signal is lower than the black dash line in Figure 4.5B). Therefore, we demonstrate an effective OR gate which implements the logical expression: C1= A OR B with inputs A and B and output C1. We also show that with the stretch of 1.5, the performance of OR gate is only slightly affected (Figure 4.5C).

Similarly, we use two ionic diodes to construct an AND gate as shown in Figure 4.6A. When the input voltage at either terminal A or B is low, e.g., 0.3V, the corresponding ionic diode is considered as conductive because the voltage difference between Vcc and input voltage is larger than the threshold value, 2.1V. Consequently, the voltage at the terminal C2 is limited by the voltage drop across the corresponding diode and can only output a low voltage signal. To verify that in the experiments, we also use same voltage signals with the square waves as of OR gate ($f_A \approx 0.018$ Hz, $f_B \approx 0.036$ Hz, $f_B = 2 f_A$) to produce periodically repeated logic state combinations as inputs for the AND gate. The output voltage at terminal C2 (Figure 4.6A) is shown in Figure 4.6B. When the input voltage at either A or B is low (or in logical "0" state), the voltage at terminal C2 is low or in logical "0" state (signal is lower than the black dash line in Figure 4.6B). When the input voltage of both A terminal and B terminal are high (or in logical "1" state), the output voltage

at terminal C2 is high or in logical “1” state (signal is higher than red dash line in Figure 4.6B). Therefore, we show an effective AND gate which implements the logical expression: C2= A AND B with inputs A and B and output C2. We also show that with stretch of 1.5, the performance of AND gate is only slightly affected (Figure 4.6C).

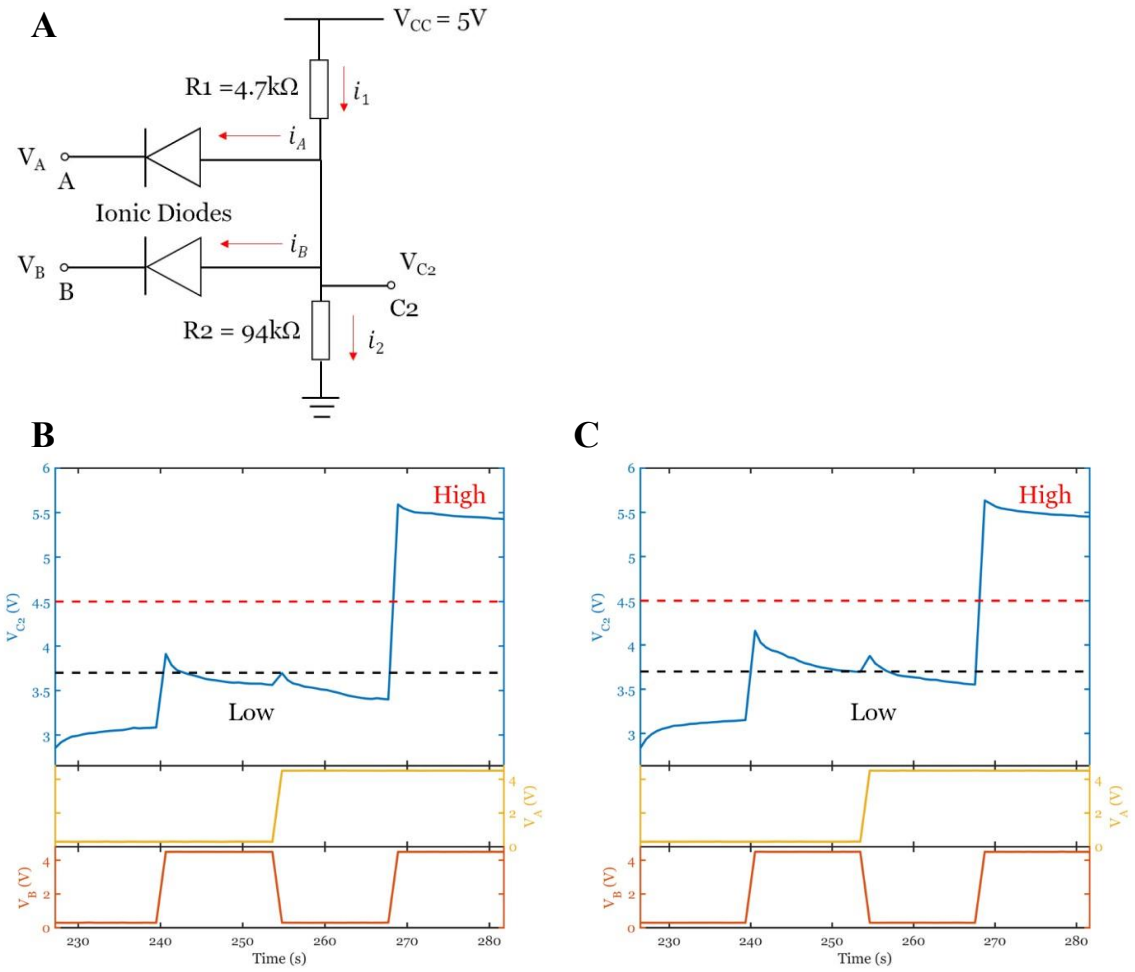

Figure 4.6: Hydrogel-based ionic AND gate.
(**A**) A circuit diagram of an ionic AND gate. A and B are the input terminals and C2 is the output terminal. (**B**) Demonstration of the logic AND operation: square waves with certain frequencies are programmed as binary inputs for the AND gate. Logic stated (0,0), (0,1), (1,0), (1,1) are generated as the inputs periodically. Voltage at C2 is measured as the output. The results confirm that this logic gate implements the logical expression: C2= A AND B. (**C**) Performance of AND gate under stretch state. Both of the two ionic diodes are stretched to 1.5 times of their original length. Input signals are the same as the ones in undeformed state.

It is noted that because of the different definitions of low and high voltage for OR gate and AND gate, we cannot simply connect the two gates together to achieve complex functions. It is very challenging to solve the problem at the current stage. Reducing the size or changing the shape of the diode can be the possible ways to solve the problem, which will be systematically investigated in the following studies. However, we would also like to point out the AND gate or OR gate can at least realize some relatively simple functions individually.

4.3 Conclusion

In this chapter, we have built a highly stretchable and transparent hydrogel-based ionic diode. We have shown that the ionic diode is highly stretchable. Although its performance such as current rectification can be affected by the applied stretch, relatively large rectification ratio of the ionic diode can be maintained when it is subjected to moderate stretch. In addition, we have also constructed ionic AND gate and OR gate, by making use of the ionic diodes. The ionic logic gates can perform specific logic operation as designed even at stretched state. We hope that the hydrogel-based ionic diode and logic gates can find potential applications in different areas including human-machine interface, stretchable ionotronics and soft robots and machines.

Acknowledgements

Chapter 4, in full, is a reprint of the material as it appears in "Stretchable and transparent ionic diode and logic gates", *Extreme Mechanics Letters,* vol. 28, 2019, by Yang Wang, Zhijian Wang, Zhengliang Su, Shengqiang Cai. The dissertation author was the primary investigator and first author of this paper.

Chapter 5 Conclusion

5.1 Summary of the dissertation

Soft materials in general provides solid foundation for development of soft robotics in many respects. Herein, we design and fabricate various LCE-based actuator and hydrogel-based ionic diode which can potentially be used for soft sensing or computing. The results we obtained has clearly demonstrated the advantages of using soft materials for either actuation or sensation. The main results of each chapter are summarized as follows:

In Chapter 2, we designed and constructed the reprogrammable LCE-based actuation using stretchable heating wire design and chemical structure design with dynamic bonds. In this work, an electrically controlled soft actuator with multiple and reprogrammable actuation modes is designed and fabricated. The soft actuator is composed of two layers of disulfide liquid crystal elastomer (ss-LCE) film with embedded resistive heating wires of serpentine shape. The actuation mode of the actuator can be programmed by introducing certain alignment of liquid crystal mesogens in the ss-LCE film, which is achieved by the controlled deformation of the actuator at room temperature and the rearrangement of polymer network through disulfide exchange reaction in the material. Actuation mode of the actuator can be easily erased by heating it up to 180°C, and a new mode of actuation can be introduced by deforming the actuator to a new shape at room temperature. With the reprogrammable and multiple actuation modes, this work demonstrates a reusable and general-purpose soft actuator which can meet various requirements in constructing new soft active devices.

In Chapter 3, we designed an artificial motor unit which owns performance close to or even outperform biological muscles. In this work, we developed an integrated artificial motor unit based on gold-coated ultrathin liquid crystal elastomer (LCE) film. Subjected to a voltage, Joule heating generated by the gold film coating increases the temperature of the LCE film underneath and causes it to contract. Due to the small thermal inertial of the ultrathin LCE structure, its cyclic actuation speed is fast and easily controllable. We showed that under electrical stimulation, the actuation strain of the LCE-based motor unit reaches 45%, strain rate is as high as 750 %/s, and the output power density is as high as 1360 W/kg. We further demonstrated that the LCE-based motor unit behaves like an actuator, a brake, or a nonlinear spring on demand, analogous to most animal muscles, controlled by electrical signals. Finally, as a proof-of-concept, we demonstrate highly dexterous artificial neuromuscular systems through the integration of the LCE-based motor unit, electronic sensors, and an electronic control system.

In Chapter 4, we demonstrated a stretchable ionic diode based on hydrogel doped with polyelectrolytes. The ionic diode is made up of polyacrylamide hydrogel doped by two different polyelectrolytes with opposite fixed charges. Due to the asymmetric distribution of the fixed charges, the hydrogel diode shows ion rectification capability. Our experiments further showed that large rectification ratio of the diode can be maintained when the diode is under moderate stretch. Using the ionic diode, we further successfully constructed two types of ionic logic gates: OR gate and AND gate, which can perform logic operations on binary inputs and produce a single

output. We hope the transparent and stretchable ionic diode, as well as the logic gates, can be used as the basic functional elements for advanced and integrated stretchable ionic circuit system.

5.2 Outlook for future work

For the LCE-based actuation, our work provides a new solution by using liquid crystal elastomer (LCE) with its own uniqueness. As for the reprogrammable LCE actuator, multiple actuation modes have been demonstrated, while the number of reprogram cycles are still limited. As for the LCE-based motor unit, the actuation frequency range of the LCE artificial muscle can cover the natural frequency of the mechanical system it is actuated by stimulating it with electrical pulses, which can amplify outputted power density through resonance. The durability of the current design still has space to further improve to meet the requirements of real applications. For the hydrogel-based ionic diodes, the current capability of information processing is limited, we may further develop ionotronics which enrich the functions to perform “soft” computation in the soft robotic systems.

Bibliography

1. Chubb, K., D. Berry, and T. Burke, *Towards an ontology for soft robots: what is soft?* Bioinspiration & Biomimetics, 2019. **14**(6): p. 063001.

2. Rus, D. and M.T. Tolley, *Design, fabrication and control of soft robots.* Nature, 2015. **521**(7553): p. 467.

3. Xiong, J., J. Chen, and P.S. Lee, *Functional Fibers and Fabrics for Soft Robotics, Wearables, and Human–Robot Interface.* Advanced Materials, 2021. **33**(19): p. 2002640.

4. Haines, C.S., M.D. Lima, N. Li, G.M. Spinks, J. Foroughi, J.D. Madden, S.H. Kim, S. Fang, M.J. de Andrade, and F. Göktepe, *Artificial muscles from fishing line and sewing thread.* Science, 2014. **343**(6173): p. 868-872.

5. Bartlett, N.W., M.T. Tolley, J.T.B. Overvelde, J.C. Weaver, B. Mosadegh, K. Bertoldi, G.M. Whitesides, and R.J. Wood, *A 3D-printed, functionally graded soft robot powered by combustion.* Science, 2015. **349**(6244): p. 161-165.

6. Laschi, C. and R.J. Wood, *Smarter materials for smarter robots*. 2021, American Association for the Advancement of Science. p. eabh4443.

7. Yang, G.-Z., J. Bellingham, P.E. Dupont, P. Fischer, L. Floridi, R. Full, N. Jacobstein, V. Kumar, M. McNutt, and R. Merrifield, *The grand challenges of Science Robotics.* Science Robotics, 2018. **3**(14): p. eaar7650.

8. Hines, L., K. Petersen, G.Z. Lum, and M. Sitti, *Soft actuators for small-scale robotics.* Advanced Materials, 2017. **29**(13): p. 1603483.

9. Kanik, M., S. Orguc, G. Varnavides, J. Kim, T. Benavides, D. Gonzalez, T. Akintilo, C.C. Tasan, A.P. Chandrakasan, and Y. Fink, *Strain-programmable fiber-based artificial muscle.* Science, 2019. **365**(6449): p. 145-150.

10. Hawkes, E.W., C. Majidi, and M.T. Tolley, *Hard questions for soft robotics.* Science Robotics, 2021. **6**(53): p. eabg6049.

11. Chen, Y., H. Zhao, J. Mao, P. Chirarattananon, E.F. Helbling, N.-s.P. Hyun, D.R. Clarke, and R.J. Wood, *Controlled flight of a microrobot powered by soft artificial muscles.* Nature, 2019. **575**(7782): p. 324-329.

12. Na, H., Y.-W. Kang, C.S. Park, S. Jung, H.-Y. Kim, and J.-Y. Sun, *Hydrogel-based strong and fast actuators by electroosmotic turgor pressure.* Science, 2022. **376**(6590): p. 301-307.

13. He, Q., Z. Wang, Y. Wang, A. Minori, M.T. Tolley, and S. Cai, *Electrically controlled liquid crystal elastomer–based soft tubular actuator with multimodal actuation.* Science Advances, 2019. **5**(10): p. eaax5746.

14. Drotman, D., S. Jadhav, D. Sharp, C. Chan, and M.T. Tolley, *Electronics-free pneumatic circuits for controlling soft-legged robots.* Science Robotics, 2021. **6**(51): p. eaay2627.

15. Zhang, Y.-Z., K.H. Lee, D.H. Anjum, R. Sougrat, Q. Jiang, H. Kim, and H.N. Alshareef, *MXenes stretch hydrogel sensor performance to new limits.* Science Advances, 2018. **4**(6): p. eaat0098.

16. Naficy, S., F. Oveissi, B. Patrick, A. Schindeler, and F. Dehghani, *Printed, Flexible pH Sensor Hydrogels for Wet Environments.* Advanced Materials Technologies, 2018. **3**(11): p. 1800137.

17. Yamada, T., Y. Hayamizu, Y. Yamamoto, Y. Yomogida, A. Izadi-Najafabadi, D.N. Futaba, and K. Hata, *A stretchable carbon nanotube strain sensor for human-motion detection.* Nature nanotechnology, 2011. **6**(5): p. 296-301.

18. Duncan, P.N., T.V. Nguyen, and E.E. Hui, *Pneumatic oscillator circuits for timing and control of integrated microfluidics.* Proceedings of the National Academy of Sciences, 2013. **110**(45): p. 18104-18109.

19. Preston, D.J., P. Rothemund, H.J. Jiang, M.P. Nemitz, J. Rawson, Z. Suo, and G.M. Whitesides, *Digital logic for soft devices.* Proceedings of the National Academy of Sciences, 2019. **116**(16): p. 7750-7759.

20. Herbert, K.M., H.E. Fowler, J.M. McCracken, K.R. Schlafmann, J.A. Koch, and T.J. White, *Synthesis and alignment of liquid crystalline elastomers.* Nature Reviews Materials, 2021.

21. Ahn, C., X. Liang, and S. Cai, *Inhomogeneous stretch induced patterning of molecular orientation in liquid crystal elastomers.* Extreme Mechanics Letters, 2015. **5**: p. 30-36.

22. Jampani, V., R. Volpe, K.R. de Sousa, J.F. Machado, C. Yakacki, and J. Lagerwall, *Liquid crystal elastomer shell actuators with negative order parameter.* Science Advances, 2019. **5**(4): p. eaaw2476.

23. Boothby, J.M., H. Kim, and T.H. Ware, *Shape changes in chemoresponsive liquid crystal elastomers.* Sensors and Actuators B: Chemical, 2017. **240**: p. 511-518.

24. Yang, C. and Z. Suo, *Hydrogel ionotronics.* Nature Reviews Materials, 2018: p. 1.

25. Koo, H.J., S.T. Chang, and O.D. Velev, *Ion - Current Diode with Aqueous Gel/SiO2 Nanofilm Interfaces.* Small, 2010. **6**(13): p. 1393-1397.

26. Yang, C.H., B. Chen, J.J. Lu, J.H. Yang, J. Zhou, Y.M. Chen, and Z. Suo, *Ionic cable.* Extreme Mechanics Letters, 2015. **3**: p. 59-65.

27. Han, J.H., K.B. Kim, H.C. Kim, and T.D. Chung, *Ionic circuits based on polyelectrolyte diodes on a microchip.* Angewandte Chemie International Edition, 2009. **48**(21): p. 3830-3833.

28. Sun, J.Y., C. Keplinger, G.M. Whitesides, and Z. Suo, *Ionic skin.* Advanced Materials, 2014. **26**(45): p. 7608-7614.

29. Mirfakhrai, T., J.D. Madden, and R.H. Baughman, *Polymer artificial muscles.* Materials Today, 2007. **10**(4): p. 30-38.

30. Tolley, M.T., R.F. Shepherd, B. Mosadegh, K.C. Galloway, M. Wehner, M. Karpelson, R.J. Wood, and G.M. Whitesides, *A Resilient, Untethered Soft Robot.* Soft Robotics, 2014. **1**(3): p. 213-223.

31. Miriyev, A., K. Stack, and H. Lipson, *Soft material for soft actuators.* Nature communications, 2017. **8**(1): p. 596.

32. Marchese, A.D., C.D. Onal, and D. Rus, *Autonomous Soft Robotic Fish Capable of Escape Maneuvers Using Fluidic Elastomer Actuators.* Soft Robotics, 2014. **1**(1): p. 75-87.

33. Li, J., Y. Wang, L. Liu, S. Xu, Y. Liu, J. Leng, and S. Cai, *A Biomimetic Soft Lens Controlled by Electrooculographic Signal.* Advanced Functional Materials, 2019. **29**(36): p. 1903762.

34. Wehner, M., M.T. Tolley, Y. Mengüç, Y.-L. Park, A. Mozeika, Y. Ding, C. Onal, R.F. Shepherd, G.M. Whitesides, and R.J. Wood, *Pneumatic Energy Sources for Autonomous and Wearable Soft Robotics.* Soft Robotics, 2014. **1**(4): p. 263-274.

35. Yuan, J., W. Neri, C. Zakri, P. Merzeau, K. Kratz, A. Lendlein, and P. Poulin, *Shape memory nanocomposite fibers for untethered high-energy microengines.* Science, 2019. **365**(6449): p. 155-158.

36. Amjadi, M. and M. Sitti, *Self-Sensing Paper Actuators Based on Graphite–Carbon Nanotube Hybrid Films.* Advanced Science, 2018. **5**(7): p. 1800239.

37. Yang, D., M.S. Verma, E. Lossner, D. Stothers, and G.M. Whitesides, *Negative-Pressure Soft Linear Actuator with a Mechanical Advantage.* Advanced Materials Technologies, 2017. **2**(1): p. 1600164.

38. Wang, Z., H. Tian, Q. He, and S. Cai, *Reprogrammable, reprocessible, and self-healable liquid crystal elastomer with exchangeable disulfide bonds.* ACS applied materials & interfaces, 2017. **9**(38): p. 33119-33128.

39. Wang, Z., Q. He, Y. Wang, and S. Cai, *Programmable actuation of liquid crystal elastomers via "living" exchange reaction.* Soft Matter, 2019. **15**(13): p. 2811-2816.

40. Petsch, S., B. Khatri, S. Schuhladen, L. Köbele, R. Rix, R. Zentel, and H. Zappe, *Muscular MEMS—the engineering of liquid crystal elastomer actuators.* Smart Materials and Structures, 2016. **25**(8): p. 085010.

41. Ohm, C., M. Brehmer, and R. Zentel, *Liquid crystalline elastomers as actuators and sensors.* Advanced Materials, 2010. **22**(31): p. 3366-3387.

42. Guin, T., M.J. Settle, B.A. Kowalski, A.D. Auguste, R.V. Beblo, G.W. Reich, and T.J. White, *Layered liquid crystal elastomer actuators.* Nature communications, 2018. **9**(1): p. 2531.

43. Ge, F. and Y. Zhao, *Microstructured Actuation of Liquid Crystal Polymer Networks.* Advanced Functional Materials, 2020. **30**(2): p. 1901890.

44. He, Q., Z. Wang, Z. Song, and S. Cai, *Bioinspired design of vascular artificial muscle.* Advanced Materials Technologies, 2019. **4**(1): p. 1800244.

45. Xiao, Y.-Y., Z.-C. Jiang, X. Tong, and Y. Zhao, *Biomimetic Locomotion of Electrically Powered "Janus" Soft Robots Using a Liquid Crystal Polymer.* Advanced Materials, 2019. **31**(36): p. 1903452.

46. de Haan, L.T., C. Sánchez‐Somolinos, C.M. Bastiaansen, A.P. Schenning, and D.J. Broer, *Engineering of complex order and the macroscopic deformation of liquid crystal polymer networks.* Angewandte Chemie, 2012. **124**(50): p. 12637-12640.

47. Schuhladen, S., F. Preller, R. Rix, S. Petsch, R. Zentel, and H. Zappe, *Iris-Like Tunable Aperture Employing Liquid-Crystal Elastomers.* Advanced Materials, 2014. **26**(42): p. 7247-7251.

48. Ware, T.H., M.E. McConney, J.J. Wie, V.P. Tondiglia, and T.J. White, *Voxelated liquid crystal elastomers.* Science, 2015. **347**(6225): p. 982-984.

49. Kotikian, A., R.L. Truby, J.W. Boley, T.J. White, and J.A. Lewis, *3D Printing of Liquid Crystal Elastomeric Actuators with Spatially Programed Nematic Order.* Advanced Materials, 2018. **30**(10): p. 1706164.

50. Dong, L. and Y. Zhao, *Photothermally driven liquid crystal polymer actuators.* Materials Chemistry Frontiers, 2018. **2**(11): p. 1932-1943.

51. Wang, C., K. Sim, J. Chen, H. Kim, Z. Rao, Y. Li, W. Chen, J. Song, R. Verduzco, and C. Yu, *Soft Ultrathin Electronics Innervated Adaptive Fully Soft Robots.* Advanced Materials, 2018. **30**(13): p. 1706695.

52. Qian, X., Q. Chen, Y. Yang, Y. Xu, Z. Li, Z. Wang, Y. Wu, Y. Wei, and Y. Ji, *Untethered Recyclable Tubular Actuators with Versatile Locomotion for Soft Continuum Robots.* Advanced Materials, 2018. **30**(29): p. 1801103.

53. Kotikian, A., C. McMahan, E.C. Davidson, J.M. Muhammad, R.D. Weeks, C. Daraio, and J.A. Lewis, *Untethered soft robotic matter with passive control of shape morphing and propulsion.* Science Robotics, 2019. **4**(33): p. eaax7044.

54. Wang, Z., K. Li, Q. He, and S. Cai, *A Light-Powered Ultralight Tensegrity Robot with High Deformability and Load Capacity.* Advanced Materials, 2019. **31**(7): p. 1806849.

55. Ahn, C., X. Liang, and S. Cai, *Bioinspired design of light-powered crawling, squeezing, and jumping untethered soft robot.* Advanced Materials Technologies, 2019. **4**(7): p. 1900185.

56. Fan, J.A., W.-H. Yeo, Y. Su, Y. Hattori, W. Lee, S.-Y. Jung, Y. Zhang, Z. Liu, H. Cheng, L. Falgout, M. Bajema, T. Coleman, D. Gregoire, R.J. Larsen, Y. Huang, and J.A. Rogers, *Fractal design concepts for stretchable electronics.* Nature communications, 2014. **5**(1): p. 3266.

57. Nishikawa, K. and T.G. Huck, *Muscle as a tunable material: implications for achieving muscle-like function in robotic prosthetic devices.* Journal of Experimental Biology, 2021. **224**(19).

58. Dickinson, M.H., C.T. Farley, R.J. Full, M. Koehl, R. Kram, and S. Lehman, *How animals move: an integrative view.* Science, 2000. **288**(5463): p. 100-106.

59. Roberts, T.J. and E. Azizi, *Flexible mechanisms: the diverse roles of biological springs in vertebrate movement.* Journal of Experimental Biology, 2011. **214**(3): p. 353-361.

60. Biewener, A.A. and M.A. Daley, *Unsteady locomotion: integrating muscle function with whole body dynamics and neuromuscular control.* Journal of Experimental Biology, 2007. **210**(17): p. 2949-2960.

61. Theriault, J.S., J.W. Bahlman, R.E. Shadwick, and D.L. Altshuler, *Work loop dynamics of the pigeon (Columba livia) humerotriceps demonstrate potentially diverse roles for active wing morphing.* Journal of Experimental Biology, 2019: p. jeb. 195578.

62. Nishikawa, K., A.A. Biewener, P. Aerts, A.N. Ahn, H.J. Chiel, M.A. Daley, T.L. Daniel, R.J. Full, M.E. Hale, T.L. Hedrick, A.K. Lappin, T.R. Nichols, R.D. Quinn, R.A. Satterlie, and B. Szymik, *Neuromechanics: an integrative approach for understanding motor control.* Integrative and Comparative Biology, 2007. **47**(1): p. 16-54.

63. Madden, J.D., N.A. Vandesteeg, P.A. Anquetil, P.G. Madden, A. Takshi, R.Z. Pytel, S.R. Lafontaine, P.A. Wieringa, and I.W. Hunter, *Artificial muscle technology: physical principles and naval prospects.* IEEE Journal of oceanic engineering, 2004. **29**(3): p. 706-728.

64. Mirvakili, S.M. and I.W. Hunter, *Artificial Muscles: Mechanisms, Applications, and Challenges.* Advanced Materials, 2018. **30**(6): p. 1704407.

65. He, Q., Z. Wang, Y. Wang, Z. Wang, C. Li, R. Annapooranan, J. Zeng, R. Chen, and S. Cai, *Electrospun liquid crystal elastomer microfiber actuator.* Science Robotics, 2021. **6**(57): p. eabi9704.

66. Wu, S., Q. Ze, J. Dai, N. Udipi, G.H. Paulino, and R. Zhao, *Stretchable origami robotic arm with omnidirectional bending and twisting.* Proceedings of the National Academy of Sciences, 2021. **118**(36): p. e2110023118.

67. Hu, W., G.Z. Lum, M. Mastrangeli, and M. Sitti, *Small-scale soft-bodied robot with multimodal locomotion.* Nature, 2018. **554**(7690): p. 81-85.

68. Lang, C., E.C. Lloyd, K.E. Matuszewski, Y. Xu, V. Ganesan, R. Huang, M. Kumar, and R.J. Hickey, *Nanostructured block copolymer muscles.* Nature nanotechnology, 2022: p. 1-7.

69. Duduta, M., E. Hajiesmaili, H. Zhao, R.J. Wood, and D.R. Clarke, *Realizing the potential of dielectric elastomer artificial muscles.* Proceedings of the National Academy of Sciences, 2019. **116**(7): p. 2476-2481.

70. Xia, Y., Y. He, F. Zhang, Y. Liu, and J. Leng, *A Review of Shape Memory Polymers and Composites: Mechanisms, Materials, and Applications.* Advanced Materials, 2021. **33**(6): p. 2000713.

71. Deschenes, M., *Short review: Rate coding motor unit recruitment patterns.* The Journal of Strength & Conditioning Research, 1989. **3**(2): p. 34-39.

72. Josephson, R., *Contraction dynamics and power output of skeletal muscle.* Annual review of physiology, 1993. **55**(1): p. 527-546.

73. Pennycuick, C. and M.A. REZENDE, *The specific power output of aerobic muscle, related to the power density of mitochondria.* Journal of Experimental Biology, 1984. **108**(1): p. 377-392.

74. Yakacki, C., M. Saed, D. Nair, T. Gong, S. Reed, and C. Bowman, *Tailorable and programmable liquid-crystalline elastomers using a two-stage thiol–acrylate reaction.* Rsc Advances, 2015. **5**(25): p. 18997-19001.

75. Lu, H.-F., M. Wang, X.-M. Chen, B.-P. Lin, and H. Yang, *Interpenetrating liquid-crystal polyurethane/polyacrylate elastomer with ultrastrong mechanical property.* Journal of the American Chemical Society, 2019. **141**(36): p. 14364-14369.

76. Boothby, J.M., J.C. Gagnon, E. McDowell, T. Van Volkenburg, L. Currano, and Z. Xia, *An untethered soft robot based on liquid crystal elastomers.* Soft Robotics, 2022. **9**(1): p. 154-162.

77. Petsch, S., A. Grewe, L. Köbele, S. Sinzinger, and H. Zappe, *Ultrathin Alvarez lens system actuated by artificial muscles.* Applied optics, 2016. **55**(10): p. 2718-2723.

78. Petsch, S., R. Rix, B. Khatri, S. Schuhladen, P. Müller, R. Zentel, and H. Zappe, *Smart artificial muscle actuators: Liquid crystal elastomers with integrated temperature feedback.* Sensors and Actuators A: Physical, 2015. **231**: p. 44-51.

79. Wang, Y., Z. Wang, Q. He, P. Iyer, and S. Cai, *Electrically Controlled Soft Actuators with Multiple and Reprogrammable Actuation Modes.* Advanced Intelligent Systems, 2020: p. 1900177.

80. Ross, S.A. and J.M. Wakeling, *Muscle shortening velocity depends on tissue inertia and level of activation during submaximal contractions.* Biology letters, 2016. **12**(6): p. 20151041.

81. Ellington, C.P., *Power and efficiency of insect flight muscle.* Journal of Experimental Biology, 1985. **115**(1): p. 293-304.

82. Bottinelli, R., M. Canepari, M. Pellegrino, and C. Reggiani, *Force-velocity properties of human skeletal muscle fibres: myosin heavy chain isoform and temperature dependence.* The Journal of physiology, 1996. **495**(2): p. 573-586.

83. Lynch, K.M. and F.C. Park, *Modern Robotics*. 2017: Cambridge University Press.

84. Enoka, R.M. and J. Duchateau, *Rate coding and the control of muscle force.* Cold Spring Harbor perspectives in medicine, 2017. **7**(10): p. a029702.

85. Zdero, R., M.M. Borkowski, and C. Coirault, *Measuring the contraction force, velocity, and length of skeletal muscle*, in *Experimental Methods in Orthopaedic Biomechanics*. 2017, Elsevier. p. 363-378.

86. Kosky, P., R. Balmer, W. Keat, and G. Wise, *Exploring engineering: an introduction to engineering and design*. 2015: Academic Press.

87. Ahn, A.N., *How muscles function–the work loop technique*. 2012, The Company of Biologists Ltd.

88. Kotikian, A., J.M. Morales, A. Lu, J. Mueller, Z.S. Davidson, J.W. Boley, and J.A. Lewis, *Innervated, Self‐Sensing Liquid Crystal Elastomer Actuators with Closed Loop Control.* Advanced Materials, 2021: p. 2101814.

89. Ketelson, H.A., D.L. Meadows, and R.P. Stone, *Dynamic wettability properties of a soft contact lens hydrogel.* Colloids and Surfaces B: Biointerfaces, 2005. **40**(1): p. 1-9.

90. Hamidi, M., A. Azadi, and P. Rafiei, *Hydrogel nanoparticles in drug delivery.* Advanced drug delivery reviews, 2008. **60**(15): p. 1638-1649.

91. Qiu, Y. and K. Park, *Environment-sensitive hydrogels for drug delivery.* Advanced drug delivery reviews, 2001. **53**(3): p. 321-339.

92. Brandt, K.A., S.A. Goldman, and T.A. Inglin, *Hydrogel-forming polymer compositions for use in absorbent structures*. 1988, Google Patents.

93. Quarfoot, A.J., P.H. Hyla, and D. Patience, *Hydrogel wound dressing*. 1990, Google Patents.

94. Lee, H.R., C.C. Kim, and J.Y. Sun, *Stretchable Ionics–A Promising Candidate for Upcoming Wearable Devices.* Advanced Materials, 2018: p. 1704403.

95. Kim, D.H., M. Abidian, and D.C. Martin, *Conducting polymers grown in hydrogel scaffolds coated on neural prosthetic devices.* Journal of Biomedical Materials Research Part A, 2004. **71**(4): p. 577-585.

96. Simon, D.T., E.O. Gabrielsson, K. Tybrandt, and M. Berggren, *Organic bioelectronics: bridging the signaling gap between biology and technology.* Chem. Rev, 2016. **116**(21): p. 13009-13041.

97. Keplinger, C., J.-Y. Sun, C.C. Foo, P. Rothemund, G.M. Whitesides, and Z. Suo, *Stretchable, transparent, ionic conductors.* Science, 2013. **341**(6149): p. 984-987.

98. Sawahata, K., J.P. Gong, and Y. Osada, *Soft and wet touch-sensing system made of hydrogel.* Macromolecular rapid communications, 1995. **16**(10): p. 713-716.

99. Yang, C.H., B. Chen, J. Zhou, Y.M. Chen, and Z. Suo, *Electroluminescence of giant stretchability.* Advanced Materials, 2016. **28**(22): p. 4480-4484.

100. Kim, C.-C., H.-H. Lee, K.H. Oh, and J.-Y. Sun, *Highly stretchable, transparent ionic touch panel.* Science, 2016. **353**(6300): p. 682-687.

101. Rogers, J.A., T. Someya, and Y. Huang, *Materials and mechanics for stretchable electronics.* Science, 2010. **327**(5973): p. 1603-1607.

102. Wagner, S. and S. Bauer, *Materials for stretchable electronics.* MRS bulletin, 2012. **37**(3): p. 207-213.

103. Wang, Y., C.-J. Huang, U. Jonas, T. Wei, J. Dostalek, and W. Knoll, *Biosensor based on hydrogel optical waveguide spectroscopy.* Biosensors and Bioelectronics, 2010. **25**(7): p. 1663-1668.

104. Mateescu, A., Y. Wang, J. Dostalek, and U. Jonas, *Thin hydrogel films for optical biosensor applications.* Membranes, 2012. **2**(1): p. 40-69.

105. Lin, S., H. Yuk, T. Zhang, G.A. Parada, H. Koo, C. Yu, and X. Zhao, *Stretchable hydrogel electronics and devices.* Advanced Materials, 2015.

106. Zhao, S., P. Tseng, J. Grasman, Y. Wang, W. Li, B. Napier, B. Yavuz, Y. Chen, L. Howell, and J. Rincon, *Programmable Hydrogel Ionic Circuits for Biologically Matched Electronic Interfaces.* Advanced Materials, 2018: p. 1800598.

107. Schroeder, T.B., A. Guha, A. Lamoureux, G. VanRenterghem, D. Sept, M. Shtein, J. Yang, and M. Mayer, *An electric-eel-inspired soft power source from stacked hydrogels.* Nature, 2017. **552**(7684): p. 214.

108. Huang, X., X.Y. Kong, L. Wen, and L. Jiang, *Bioinspired Ionic Diodes: From Unipolar to Bipolar.* Advanced Functional Materials, 2018: p. 1801079.

109. Frilette, V.J., *Preparation and characterization of bipolar ion exchange membranes.* The Journal of Physical Chemistry, 1956. **60**(4): p. 435-439.

110. Mafe, S. and P. Ramirez, *Electrochemical characterization of polymer ion-exchange bipolar membranes.* Acta polymerica, 1997. **48**(7): p. 234-250.

111. Hurwitz, H.D. and R. Dibiani, *Investigation of electrical properties of bipolar membranes at steady state and with transient methods.* Electrochimica acta, 2001. **47**(5): p. 759-773.

112. Han, J.H., K.B. Kim, J.H. Bae, B.J. Kim, C.M. Kang, H.C. Kim, and T.D. Chung, *Ion flow crossing over a polyelectrolyte diode on a microfluidic chip.* Small, 2011. **7**(18): p. 2629-2639.

113. Gabrielsson, E.O., P. Janson, K. Tybrandt, D.T. Simon, and M. Berggren, *A four-diode full-wave ionic current rectifier based on bipolar membranes: Overcoming the limit of electrode capacity.* Advanced Materials, 2014. **26**(30): p. 5143-5147.

114. Zhang, W., X. Zhang, C. Lu, Y. Wang, and Y. Deng, *Flexible and transparent paper-based ionic diode fabricated from oppositely charged microfibrillated cellulose.* The Journal of Physical Chemistry C, 2012. **116**(16): p. 9227-9234.

115. Cayre, O.J., S.T. Chang, and O.D. Velev, *Polyelectrolyte diode: Nonlinear current response of a junction between aqueous ionic gels.* Journal of the American Chemical Society, 2007. **129**(35): p. 10801-10806.

116. Yamamoto, T. and M. Doi, *Electrochemical mechanism of ion current rectification of polyelectrolyte gel diodes.* Nature communications, 2014. **5**: p. 4162.